Sascha Krüger

Laser Diagnostics in Two Phase Flows

Cuvillier Verlag Göttingen

Angewandte
Laserphysik

Laser Diagnostics in Two Phase Flows

Doctoral Dissertation

by

Sascha Krüger

Faculty of Physics
University of Bielefeld

June 2001

Die Deutsche Bibliothek - CIP-Einheitsaufnahme

Krüger, Sascha:
Laser Diagnostics in Two Phase Flows / vorgelegt von Sascha Krüger. -
1. Aufl. - Göttingen : Cuvillier, 2001
Zugl.: Bielefeld, Univ., Diss., 2001
ISBN 3-89873-210-X

Nonnenstieg 8, 37075 Göttingen
Telefon: 0551-54724-0
Telefax: 0551-54724-21
www.cuvillier.de

1. Auflage, 2001
Gedruckt auf säurefreiem Papier

ISBN 3-89873-210-X

Contents

Chapter 1

Introduction

The theory of evaporation in dense sprays, where the average spacing of the droplets is only a few droplet diameters, is still incomplete, due to the strong interactions (heat and mass transfer) of the droplets and the gas phase [21]. In addition, the interactions of dispersed and continuous phase in non-evaporating, highly particle-laden gas flows are not fully understood [23]. This makes it difficult to model the flow field of the gas phase in dense sprays. It should be noted that dense sprays are technically important. For example, high-pressure swirl injectors, generating dense hollow-cone sprays, are currently being developed for automotive direct injection spark ignition engines [5], [3]. One reason for the lack of a satisfactory theory of dense spray evaporation is the fact that little experimental data exists of the gas flow field in such two-phase flows. The lack of experimental data is mainly caused by severe difficulties which are encountered when conventional measurement techniques are applied to highly particle-laden flows. In principle, point-wise gas velocity measurements can be performed in sprays by Phase Doppler Anemometry (PDA) based on sufficiently small particles [24]. However, PDA suffers from high number densities of droplets and beam steering, for example, in the dense regions of automotive direct injection sprays [2]. Particle Image Velocimetry (PIV) based on fluorescent particles can also be employed for gas-phase velocity measurements in sprays [25]. However, PIV is not applicable when the medium is so dense that the detected signal is strongly affected by multiple light scattering [3]. PIV requires that individual particles are resolved, and this becomes impossible when strong multiple scattering results in considerable image blurring. It is well established that the flow field of the continuous phase is important for break-up and evaporation of sprays. The flow field is also an important parameter in the combustion of spray flames. It is desirable to measure the velocity fields of both phases in two-phase flows in order to study their interactions. Furthermore it is advantageous to measure both velocity fields simultaneously, so that the interactions can be studied on a "single-shot" basis, in particular in unsteady, non-reproducible two-phase flows. In this work techniques to extract instantaneous 2D and 3D flow fields of the dispersed and the continuous phase from said technical systems were developed. Validations of these new techniques were performed and combustion and spray systems were investigated.

Chapter 2

An optical flow algorithm for fluid flow velocity analysis

A basic problem in the processing of digital image sequences is the measurement of optical flow. An optical flow algorithm (OFA) is a tool for the computation of the 2D image velocity field, which is a projection of the 3D velocities of the surface points visible in the images, from spatial patterns in the images. The obtained 2D velocity information can be used for many different tasks. They range from the determination of the ego-motion of a robot to the measurement of the velocities of image parts. In this work techniques of optical flow will be applied to the determination of the velocities of gases and liquids. The chosen numerical approach for this implementation will be presented in the following.

This algorithm is related to the work of Gornowicz ([39]) and Dimotakis et al. ([17]). The input data often consists of two images to be correlated. Typically these have been acquired with a CCD camera at two times, that differ by a small delay Δt. The result of the algorithm will be the displacement field $\Delta\vec{s}(\vec{x})$, which describes how sub-volumes of image 1 have to be translated to approximately yield image 2. The velocity field is then simply given by:

$$\Delta\vec{v}(\vec{x}) = \frac{\Delta\vec{s}(\vec{x})}{\Delta t} \tag{2.1}$$

The basic concept of the algorithm can be explained in two steps as Fig. 2.1

shows. The first step will be referred to as initialization and the second step as global optimization. The main idea is to optimize the correlation of the two images by varying a certain globally defined function that describes the transformation between these two images (matrices). So this optimization means "morphing" one image of the data pair into the other.

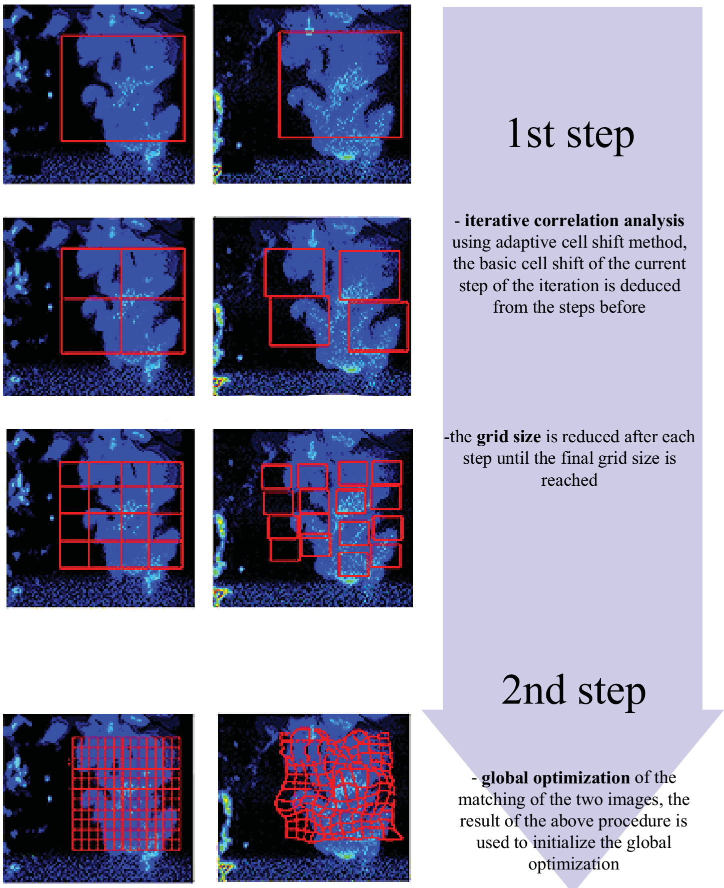

Figure 2.1: Basic principle of the algorithm. The initialization based on direct correlation analysis (See [87] for a comparison to FFT-based correlation analysis) yields the starting parameters for a continuous field optimization.

The number of the parameters, that determine the mapping function, determines the dimensionality of the problem, which in most cases is a highly multidimensional problem, that depends on the complexity of the measured system. Numerical optimizations in multidimensions require an initialization.

This means that the approximate solution of the problem has to be known. This approximate solution is provided by the initialization step. The following global optimization in multidimensions is then performed by means of a conjugate gradient method. The chosen implementation of this numerical procedure is the code from Polak/Ribiere ([90]).

2.1 Initialization

This type of initialization is an iterative local direct correlation analysis. The function, that measures the state of local correlation, is given by equation 2.2.

$$C^K_{\Delta i,\Delta j} = \frac{\sum_{i,j\in K} I_{1_{i,j}} \cdot I_{2_{i+\Delta i,j+\Delta j}}}{\sqrt{\sum_{i,j\in K} I^2_{1_{i,j}}} \cdot \sqrt{\sum_{i,j\in K} I^2_{2_{i+\Delta i,j+\Delta j}}}} \tag{2.2}$$

Equation 2.2 is similar to the well known Pearson's correlation function, which is suitable for measurements of the correlation between images that contain continuous scalar data. This type of image has to be distinguished from the type of image that contains discrete structures. In the latter case the determination of optical flow can be done with well-established local correlation analysis and is comparatively straight. The determination of velocity fields from scalar continuous data with a high resolution however is a difficult problem. Besides function 2.2 other functions can be useful, depending on the concrete relation between the average structure size in the images and the spatial scales of the velocity field.

$$C^K_{\Delta i,\Delta j} = \sum_{i,j\in K} I_{1_{i,j}} \cdot I_{2_{i+\Delta i,j+\Delta j}} \tag{2.3}$$

$$C^K_{\Delta i,\Delta j} = \frac{\sum_{i,j\in K}(I_{1_{i,j}} - \bar{I}_1) \cdot (I_{2_{i+\Delta i,j+\Delta j}} - \bar{I}_2)}{\sqrt{\sum_{i,j\in K}(I_{1_{i,j}} - \bar{I}_1)^2} \cdot \sqrt{\sum_{i,j\in K}(I_{2_{i+\Delta i,j+\Delta j}} - \bar{I}_2)^2}} \tag{2.4}$$

$$C^K_{\Delta i,\Delta j} = \sum_{i,j\in K} (I_{1_{i,j}} - I_{2_{i+\Delta i,j+\Delta j}})^2 \tag{2.5}$$

The equations 2.3 and 2.4 describe the standard correlation function and Pearson's correlation function respectively. K is a sub-volume of the whole correlation volume (Area Of Interest, AOI), e.g. 128 x 128 pixels. It is defined on I_1. $(\Delta i, \Delta j)^T$ is the translation vector of sub-volume K, which is given by the position of the maximum of the matrix C. One step of iteration is performed as follows (see Fig. 2.1): The current sub-volume K is divided into 4 equal sub-volumes. For each of these sub-volumes the translation of the mother sub-volume is taken as initial translation. The real translation of these sub-volumes is found by performing a new correlation analysis on the shifted sub-volumes. For each new translation vector only a certain deviation of the initial translation vector is allowed. This magnitude of the allowed deviation is a function of the step of division, which is adapted to the flow field under investigation. It strongly depends on the spatial scales of the flow field. This procedure is repeated until the final grid size (resolution) for this step is reached. Generally the average structure size in the images determines the lower limit for this final grid size. A detailed discussion will be given in sect. 3.3.1. Note that correlation analysis on continuous scalar image data is a very challenging task. Continuous structures always lead to correlation matrices with broad ridge-like correlation peaks in contrast to sharp correlation peaks arising from discrete structures (ref. PIV). For this reason it should be clear that scalar continuous data are very sensitive to error sources like noise. This justifies the high computational expense when using a direct correlation method in this implementation resulting in more reliable correlation matrices. Problems arising from remaining erroneous correlation peaks have to be eliminated. This leads to the following section on vector validation algorithms.

2.2 Vector Validation Algorithms

As mentioned in Sect. 2.1 the initialization is the main precondition for a successful global continuous-field optimization. Thus the dependability of the initialization process, i.e. the proposed iterative correlation analysis followed by the selection of valid starting vectors, is very important. The selection of valid vectors from a given vector field is often referred to as vector validation.

From literature ([85], [83]) several procedures concerning the elimination of correlation errors are known. In principle they can be divided into two subfamilies. One family is based on physical arguments derived from properties of the fluid flow system under investigation, the other is based on statistical or mathematical arguments, e.g. steadiness. Procedures of the latter family shall be shortly discussed in the following. As a commonly known example the local median filter based on a local analysis of the vectors according to equation 2.6 has to be mentioned:

$$\mid \vec{v}_{i,j} - < \vec{v}_{n.n.} > \mid \leq c \cdot \sigma(\vec{v}_{n.n.}) \tag{2.6}$$

In equation 2.6 (i,j) denotes the position of the vector to be validated, n.n. are the next neighbours of said vector, $\sigma(\vec{v}_{n.n.})$ is the RMS and $< \vec{v}_{n.n.} >$ the average of these neighboured vectors. c is a user-defined factor determining the degree of restriction of the procedure. This is a typical example of a *local* validation procedure.

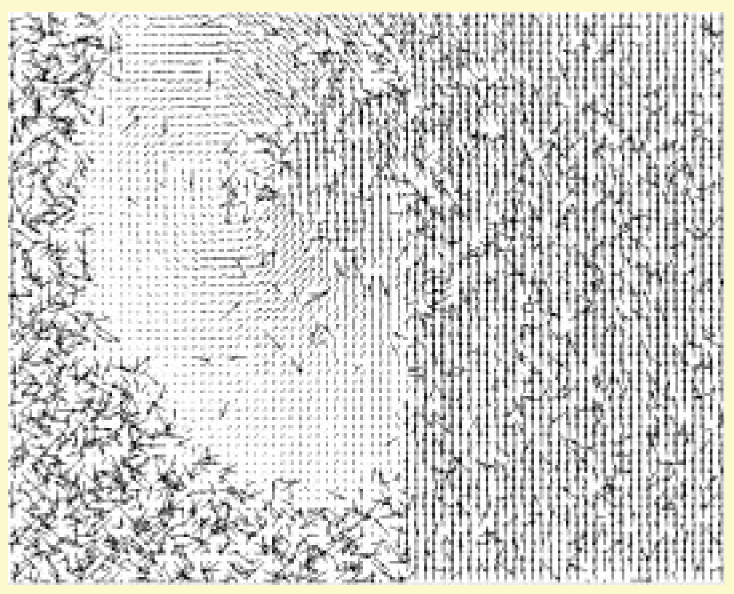

Figure 2.2: Initialization data without validation of vectors. A lot of erroneous vectors can be found in almost any region of the field. The underlying flow field was generated with the set-up in Fig. 4.1. Despite the numerous false vectors the vortical structure of the flow field can be seen.

Fig. 2.2 shows initialization data without application of a validation procedure. A lot of spurious vectors can be found even in the main strutcure of the flow field, i.e. the vortex. The underlying flow field was generated with the set-up in Fig. 4.1. It is a very challenging task to eliminate false vectors with a local median filter. Fig. 2.3 shows validated vectors obtained by applying equation 2.6 with $c = 0.7$. As can be seen, a lot of spurious vectors were successfully removed. But although the criteria for validation was chosen very restrictive, some erroneous vectors can still be found. Furthermore it can be seen, that as an effect of the high degree of restriction the data has already become quite holey, especially in regions , where high velocity gradients occur (vortex). As the global optimization process requires data on a regular grid, missing vectors have to be determined by e.g. interpolation. Special filters for this purpose can be found in the literature and shall not be discussed here ([82]). Nevertheless it is obviously desirable that the validation routine conserves as many correct vectors as possible and removes almost *all* erroneous vectors. An advanced gobal vector validation routine was therefore implemented. It is mainly based on the work of Nogueira et al. ([82]).

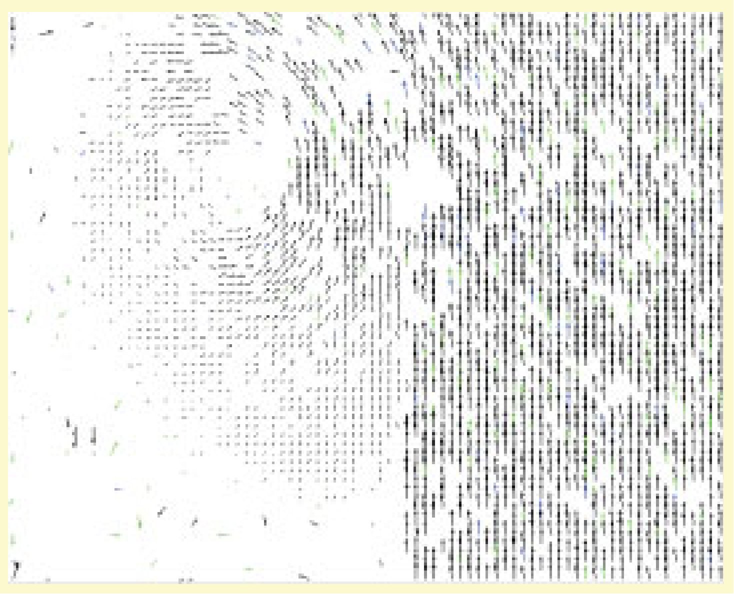

Figure 2.3: Validated vectors obtained by applying equation 2.6 with $c = 0.7$.

In a first step regions of local coherence, which are defined via equation 2.7, are sought.

$$c_0 = \frac{\sum_{i \in \Omega_{n.n.}} \mid v_i - v_0 \mid}{\sum_{i \in \Omega_{n.n.}} \mid v_i \mid} \tag{2.7}$$

$\Omega_{n.n.}$ is the set of 8 nearest neighbours of the grid node with velocity v_0. A region where equation 2.7 reaches a minimum is a zone of local coherence. In the second step of the algorithm the whole vector field is scanned and vectors, coherent with those found in the first step, are identified. A vector v_0 to be validated is then called coherent if any of the following preconditions is met:

1. $\exists T \subseteq \Omega_{n.n.}, \#(T) \geq 2, \mid v_0 - \frac{\sum_{j \in T} v_j}{\#(T)} \mid \leq c_1$

2. Its euclidean distance from the linear interpolation of any combination of three not aligned vectors among the validated neighbours around the node 0 is smaller than a given amount c_2

Now, as a third step, step 2 is repeated until no further vectors can be validated anymore. Thus the zones of local coherence found in the first two steps are allowed to grow and merge with previous ones. In the final fourth step the domains of coherence found during the steps 1-3 are validated by checking the number of validated vectors contained. Domains with only few vectors (less than a certain amount c_3) are finally rejected.

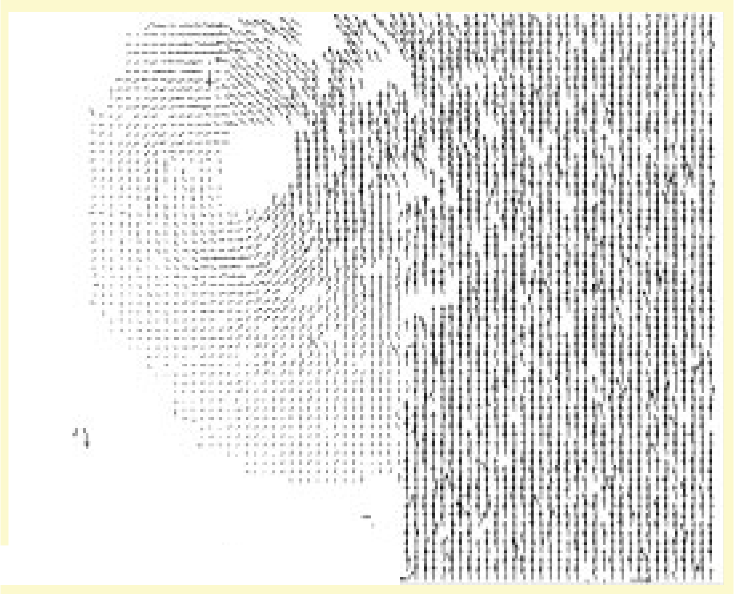

Figure 2.4: Validated vectors obtained by application of the new algorithm.

Fig. 2.4 shows validated vectors after application of the described validation algorithm to the example vector field. The difference to local validation procedures can be seen. Only in regions, where obvious errors of the correlation routine occur, vectors are rejected. Reliable vectors are mainly maintained which leads to a dense vector information across the whole flow system. The fourth step of the algorithm was not applied. Therefore some small erroneous domains can still be found in the image. Thus an impression of the power of this validation algorithm shall be given. In a real run the fourth step is applied and gaps are filled by an interpolation routine providing starting vectors for the minimization process on a regular grid in the whole AOI.

2.3 Conjugate Gradient Optimization

After the initialization step translation vectors for the whole correlation volume are found. Each translation vector describes the motion of the corresponding sub-volume of the final size of the correlation procedure (e.g. 32 x 32 pixels). Now a global mapping function based on B-Splines is created. The field is determined by the so-called control parameters $\vec{q}_{i,j}^{\,(\mathrm{p})}$, which are as said before initially taken from the result of the initialization. The B-Spline representation of the field is:

$$\vec{\xi}(\vec{x}) = \sum_{r=R_{min}}^{R_{max}} \sum_{i,j \in AOI} \vec{q}_{i,j}^{\,(\mathrm{p})} \cdot B_i^{(r)(p)}(x) \cdot B_j^{(r)(p)}(y) \tag{2.8}$$

The control parameters are defined on a grid with the highest possible resolution R. Note that the mapping function itself is defined with pixel resolution. But the physical resolution is given by the number of degrees of freedom, i.e. the number of control paramters $\vec{q}_{i,j}$.The B-Spline order p is an internal parameter and in the current implementation always set to the value 3. With this mapping function defined on the whole AOI a general minimization problem can easily be formulated:

$$\int_{AOI} f(I_1(\vec{x}), I_2(\vec{x}), \vec{\xi}(\vec{x}))d\vec{x} \overset{!}{=} min \tag{2.9}$$

Depending on the images different functions $f(I_1, I_2, \xi)$ can be used. Besides the above mentioned (equation 2.2 - 2.3) the following function is available:

$$f(I_1(\vec{x}), I_2(\vec{x}), \vec{\xi}(\vec{x})) = (I_1(\vec{x}) - I_2(\vec{x} + \vec{\xi}(\vec{x})))^2 \tag{2.10}$$

In the literature this function is generally referred to as *cost function.* Note that the functions contained in equation 2.2-2.3 must be mirrored for use in a minimization process.

Problem 2.9 can be solved numerically by means of an iterative gradient based method which is called conjugate gradient method. The gradient of the left hand side of 2.9 with respect to the control parameters is calculated. The attribute conjugate means that gradients of several steps are taken into account when calculating the direction of optimization in the current step. This strongly enhances the minimization process. The iteration is stopped when the desired accuracy is reached.

The algorithm was trained on data obtained from measurements in gaseous flows, where Schmidts Number $S_c = \frac{\nu}{D} \approx 1$. This implies, that the influence of the molecular diffusion D is comparable to that of the kinematic viscosity ν, which often leads to the situation, that the average structure size of the seeded flow marker, which itself is a gas (examples will be given later), is comparable to the spatial scales of the velocity field, which shall be investigated. Detailed studies on the achieved accuracy of this implementation

in such situations will be given in the chapters 3 and 4. Note that the use of optical flow algorithms in systems with $S_c = \frac{\nu}{D} \approx 1$ differs from typical applications of optical flow given in [39], where structures are always much smaller than the scales of the velocity field.
The OFA will serve as a basic instrument for the measurements presented in the following.

Chapter 3

Gas-Phase Velocity Field Measurements in Sprays Without Particle Seeding

A laser-based technique is presented that can be used to measure the instantaneous velocity field of the continuous phase in sprays and aerosols. In contrast to most well established laser-based velocity measurement techniques, this method is independent of particle seeding and Mie scattering. Instead of that it is based on gaseous flow tracers and laser-induced fluorescence (LIF). Inhomogeneous tracer gas distributions, which are created by an incomplete, turbulent mixing process, are exploited for flow tracing. The velocity field can be measured close to the droplets, because frequency-shifted LIF is separated from Mie scattering by optical filters. Validation tests and results from a water spray in air are given. Accuracy and spatial resolution are discussed in detail.

3.1 Introduction

It is well established that the flow field of the continuous phase is important for break-up and evaporation of sprays. The flow field is also an important parameter in the combustion of spray flames. Very few non-intrusive techniques are capable of measuring gas-phase velocity fields close to droplets, because most of the established two-dimensional techniques, such as particle image velocimetry (PIV), are based on Mie scattering from tracer particles. The present technique works similar to PIV, but the seed particles are replaced by a gaseous tracer (NO). Double-pulse imaging of laser-induced fluorescence (LIF) from the gaseous tracer is used in the present experiment. The velocity field is computed from the LIF images, essentially, by using the OFA presented in chapter 2 which is based on the Image Correlation Velocimetry (ICV) method presented by Tokumaru and Dimotakis (1995). PIV and ICV can be employed to measure the velocity field of any gaseous, liquid or solid phase (continuous or dispersed) in different applications, whereas the present technique aims to measure the velocity of the gas phase only. It should be noted that very different experimental problems are encountered when velocity measurements are performed with gases, particles, or liquids, respectively. This chapter focuses on the problems encountered with gaseous tracers in the gas phase. Specifically, enhanced molecular diffusion of the tracer is a major problem in this case, so that a special experimental technique is required. For example, it is generally necessary to acquire two consecutive images with a much smaller delay than in the experiments of Su & Dahm (1996), Maas (1993) and others, who did velocity measurements using molecular tracers in liquids (see next section). Diffusion of gaseous tracers also causes more difficulties in sustaining inhomogeneous tracer distributions, which are required for tracing the velocity field. Further consequences will be discussed below. A suitable set-up for probing the gas-phase velocity field using gaseous tracers, which can be applied to a wide variety of sprays, will be described. It is generally difficult to separate any laser-induced signals from the tracer particles and the droplets in sprays or aerosols ([1], [48]). PIV based on fluorescent seed particles can be used in some cases ([25], [56]), but there are no suitable fluorescent particles for high-temperature (combustion) applications. In contrast, the present technique can also be applied in this case, when a suitable tracer such as NO is employed ([40] and references therein). There has been no technique for instantaneous velocity field measurements of the continuous phase in sprays and aerosols without particle seeding, which can also be applied to spray flames. The use of gaseous tracers could make it possible to study the flow field on smaller spatial scales.

The ultimate spatial resolution of particle-based techniques is limited, among other factors, by the average spacing between the particles, because there is no information provided about the fluid between the particles. Very high spatial resolution was achieved by the "super-resolution" PIV method, which is capable of tracing individual particles ([42]). The authors reported a spatial resolution of about 0.1 mm, roughly corresponding to the spacing of the particles. In principle, the spatial resolution can be improved by using higher particle densities, but an optical penetration difficulty arises at a certain density, as pointed out by Su and Dahm (1996). These difficulties can be circumvented using gaseous tracers. Thus, the flow field very close to single droplets, in droplet clusters, or in shear layers near surfaces could be measured. A resolution of ≈ 10 μm has been achieved in liquids, for example by Meinhardt et al. (1998), but these techniques are not available for gas phase measurements. The spatial resolution and accuracy of the present technique will be discussed in detail. Other potential advantages of the present technique will be discussed in chapter 4. Other related velocimetry techniques, which do not require seed particles, will also be described there.

3.2 Experimental

The present technique was applied to a steady water spray in room air. An automobile Bosch-type port fuel injector ([62]) was used, which was operated with a backing pressure of 3 bar. This injector generates a conical spray. The Sauter mean diameter of the droplets can be estimated to be $d_{32} = 100$ - 140 μm (arithmetical mean diameter $d_{10} = 30$ - 50 μm) a few centimetres downstream from the nozzle, where the measurements were performed ([63], [14]). There the droplet density can be estimated to be 10 - 100/cm^3, whereas it is of the order of 10^5/cm^3 in the center of the spray. The experimental set-up is outlined in Figure 1. A measured raw image is included at y = 2-4 cm. The injector was moved with regard to the detection system in order to scan the velocity field up to 10 cm downstream from the nozzle. The present technique is based on planar LIF from a gaseous tracer. NO was used as the tracer in the present experiment. The tracer was probed twice with a short time delay using two laser pulses, similar to double-pulsed

PIV. The probe area was imaged onto a CCD camera using optics with a demagnification of 2:1 ($f_{\#} = \mathrm{f/D} = 8.8$). The field of view in this experiment contains 6.2 cm^2. The spatial resolution of the camera system, including optics, is limited by the pixel size, which corresponds to 70 μm in the probe volume. The resolution in the z direction is determined by the width of the laser sheets, which was about 150μm. A progressive scan CCD camera (LaVision), that is capable of recording two images with a delay down to $\approx 1\mu$s, was employed. Rapid double-pulse illumination with such a short delay can be performed using two independent, pulsed lasers (see below). It should be emphasized that the delay of the two images generally must be much smaller when experiments are performed in gases using gaseous tracers compared to liquids, due to enhanced molecular diffusion, as mentioned in the Introduction. The typical delay in these measurements was 150μs. In contrast, Su & Dahm (1996) and Maas (1993), who did related experiments in liquids, used high-speed cameras with delays of the order of 5 ms between consecutive images. The choice of the delay also depends on the interesting time scales of the flow field similar to PIV. The CCD camera is equipped with an image intensifier (DEP), which is capable of detecting fluorescence in the ultraviolet wavelength range. The intensifier also amplifies the LIF signals from NO, so that low NO tracer concentrations (see below) can be detected accurately. The LIF photons impinging on the photocathode of the intensifier generate photoelectons with a certain probability (quantum efficiency). These photoelectrons are multiplied in the intensifier, so that they can be detected by the CCD camera without much additional noise generated by the camera. Thus, the number of photoelectrons N (per pixel) created by a single laser shot essentially determines the noise in these "shot-noise-limited" measurements ([61]). The shot noise will be quantified in Sect. 3.3.1. An optical filter (1 cm layer of butylacetate) is used in front of the camera system in order to suppress Mie scattering from the dispersed phase. The filter exhibits a sharp cut-off wavelength at about 250 nm and suppresses the Mie scattering at ≈ 226 nm by at least four orders of magnitude, so that it is negligible in those regions of the dilute spray, where the measurements were performed. This filter is not sufficient to suppress Mie scattering completely on the spray axis. For example, the measured image in Fig. 3.1 exhibits some Mie scattering on the spray axis. This does not interfere with the LIF signal, which is located on the right hand side of the image. However, the filter should be improved for future applications to dense sprays.

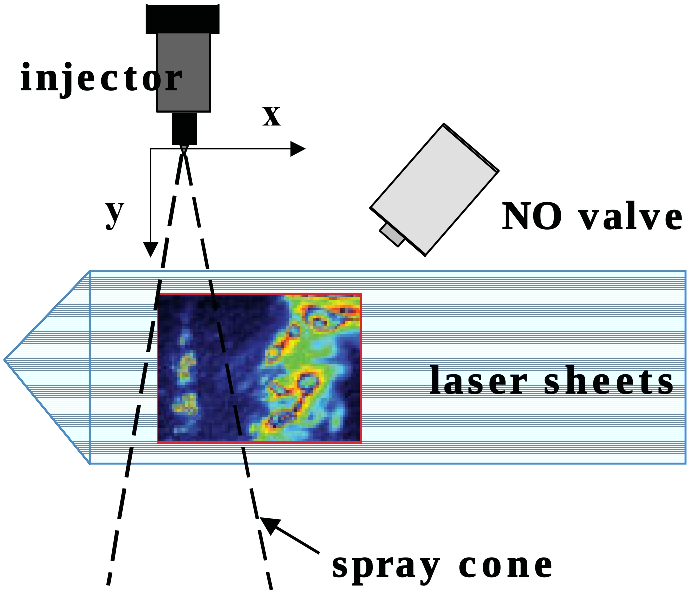

Figure 3.1: Experimental set-up. The Bosch-type injector is moved in x- and y-directions with regard to the measurement system to scan the velocity field. A typical raw LIF image is also shown in the range y = 2-4 cm.

The tracer seeding technique plays an important role in this type of experiments. It is crucial to generate spatially inhomogeneous tracer distributions across the field of view, because the inhomogeneous distributions are exploited for tracing the flow. Seeding is often more convenient with gaseous tracers than with particles. On the other hand, diffusion of gaseous tracers must be taken into account as an additional factor, because any inhomogeneities in the tracer distributions diminish due to diffusion, in particular if the delay between seeding and detection is long. It is generally also desirable that the flow field is not considerably altered by the seeding process. One example how to achieve this in a diffusion flame is described elsewhere ([40]). As a general rule, seeding of small amounts of tracer gas well upstream with regard to the probe volume and with a long delay before detection is a suitable way to perform non-intrusive seeding. On the other hand, the delay must be limited, so that the tracer gas distributions are not washed out by diffusion as mentioned above. NO seeding was performed by discharging a "cloud" of pure NO in the ambient air of the spray using a pulsed valve (General Valve) in this experiment, as outlined in Fig. 3.1. The backing pressure of this valve was slightly higher than the ambient pressure (ca. 0.4 bar), so that the ambient air is not strongly accelerated by the NO jet. The pulsed NO valve was triggered 25 ms before LIF detection was performed, and this delay was much longer than the pulse length of the NO valve (0.5 ms). It turned out that the gas motion in the probe volume induced by this seeding method was much weaker than the gas motion caused by the spray. The NO was predominantly drawn into the probe volume in a passive way by air entrainment. These NO "clouds" were several cm^3 large. The NO concentration in the probe volume was typically of the order of 0.1 % when it was probed. Further information on the structure of the NO distributions is given in the next section (see also Fig. 3.4). NO was excited at about 226 nm via the $R_21(17.5)$ line in the $\gamma(0,0)$ band ([38]). For this purpose, two pulsed, tunable, narrowband KrF excimer lasers were used. The laser radiation was shifted to $\approx$ 226 nm using stimulated Raman scattering in two hydrogen cells. The resulting $\gamma(0,3)$, $\gamma(0,4)$, and $\gamma(0,5)$ LIF emission lines between 250 nm and 300 nm were recorded by the camera system. This was performed with a gate length of about 100 ns, so that the resulting images show instantaneous NO distributions. The recorded images have been corrected for non-linearity effects of the detector, so that the image intensity is finally proportional to the NO concentration. The images are also corrected for variations in the pixel-dependent detection efficiency, so that a given NO concentration results in the same image intensity at any position in the images (at least over the length scale of the displacement). Otherwise the overall detection efficiency would be pixel-dependent due to inhomogeneities in the laser beam profiles and other factors. These calibration procedures are important for the accuracy of the data evaluation as described elsewhere ([18]). A number of quantification problems of LIF from small molecules at high pressure (>= 1bar) are discussed in the literature, e.g., due to quenching ([66] and references therein). These quantification problems can be neglected here, because quantification of the NO density is not necessary for measuring the velocity field. However, any factor that may change the LIF signal between the two laser pulses other than the flow field must be considered. For example temperature changes could change the LIF signal in spray flames, which is discussed elsewhere ([40]). Also mixing with certain majority species, e.g., water vapor in spray flames, that lead to higher quenching rates than others, may change the LIF quantum yield between the two laser pulses. Generally these factors can be suppressed by decreasing the delay between the laser pulses. Essentially the same set-up was also used for Mie scattering imaging in order to determine the position of the spray cone. NO seeding was disabled and the Mie filter was removed in this case.

3.3 Results and discussion

Fig. 3.2 a)/b) shows a pair of typical LIF images recorded at the edge of the spray (y=4-6 cm) with a delay of $\Delta t = 150 \mu s$. The inner frame in the images corresponds to the "correlation volume", where the velocity field is to be determined.

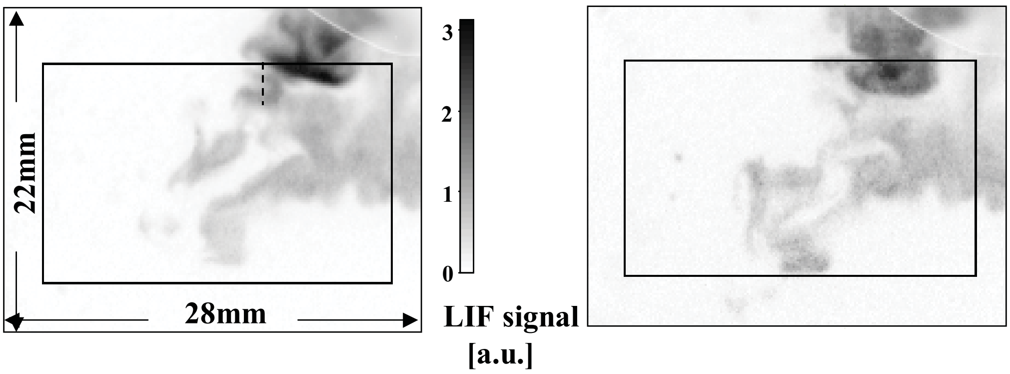

Figure 3.2: Pair of LIF (NO) images recorded with a delay of 150μs. The inner rectangles indicate the correlation volume. The dotted line in Fig. 3.2a) shows the position of the profile given in Fig. 3.4.

Fig. 3.3 shows the instantaneous velocity field determined from these images. It can be seen that the velocity vectors have been suppressed in regions where the LIF signal is smaller than a certain level (the threshold is chosen as 15% of the average LIF signal in the present data set). The remaining velocity vectors cover about 50 % of the correlation volume. The suppression of velocity vectors is necessary because the accuracy of the LIF images is shot-noise limited, so that small signal intensities are particularly noisy (see Sect. 3.3.1). Thus, the suppression of the corresponding velocity vectors will improve the accuracy of the temporally averaged velocity fields. It can be assumed that this procedure does not change the eddy statistics. In other words, the procedure does not suppress specific velocity vector classes of the ensemble, because it can be assumed that there is no specific correlation between the instantaneous velocity field and the scalar field. The scalar field is not directly linked to the instantaneous velocity field, but it depends on the whole history of the seeding process (25 ms of turbulent mixing). The most important potential sources of error of the present technique are discussed in the following. First, the accuracy may be affected by attenuation (shadowing) of the laser beams or the LIF emission, when it is applied to very dense or strongly absorbing sprays. The ICV data reduction scheme assumes that the overall detection efficiency is constant throughout the images (or at least constant over the length scale of the displacement of the tracer molecules). This requires that the local laser intensity is not changed due to absorption or strong scattering, and that the LIF is not affected by "secondary scattering" in such optically dense media. These difficulties are circumvented, basically, by performing measurements in the dilute spray region near the edge of the spray cone, where the droplet density is roughly 10-100 /cm^3 (see Sect. 3.2). In addition, water was used as the liquid fluid, which does neither absorb the laser radiation nor the LIF. The laser beam intensity was measured after passing the probe volume in order to check if attenuation due to strong scattering occurred. It turned out that the attenuation was $<$5 %, so that it can be assumed that the local laser intensity is constant and the LIF is not affected by "secondary scattering" ([64]). In addition, no significant shadowing of the LIF within the spray cone, in particular behind larger droplets, was observed in the images.

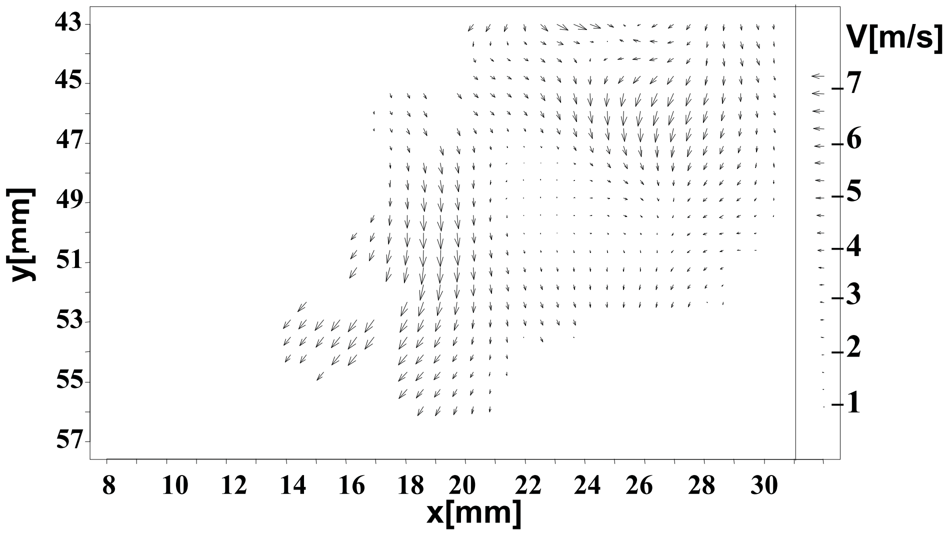

Figure 3.3: Instantaneous velocity field calculated from two consecutive LIF images, which are given in Fig. 3.2a)/b). The data is only provided in regions with sufficient LIF signal.

Generally the detection efficiency may also be affected by attenuation of the laser light due to strong absorption by the tracer molecules or trapping of the LIF due to re-absorption, in particular under high-pressure conditions. This was avoided by low NO concentrations (sub-percent range) in the probe volume and atmospheric pressure. Indeed, no significant absorption of the laser beams was observed after passing the NO distributions. The ICV data reduction method assumes that molecular diffusion of the tracer between the two LIF measurements is negligible. This assumption is discussed in the following. The smallest length scales in the typical images in Fig. 3.2 are around $\approx$ 1mm (apart from image noise). This can be observed in the LIF intensity profile in Fig. 3.4, that has been extracted from Fig. 3.2a) at x = 23 mm (the image in Fig. 3.2a has been smoothed over 2x2 pixels before the profile was extracted, in order to suppress image noise and visualize the true NO distribution). The diffusion of such NO distributions can be estimated, as a first approach, by solving Fick´s law for Gaussian tracer distributions analytically. The initial width (FWHM) of the Gaussian distribution is assumed to be 1.00 mm (in three dimensions) in this test. It turns out that the FWHM increases to about 1.01 mm due to diffusion within $\Delta t = 150\mu s$

(diffusion coefficient $D_{NO}^{air} \approx 0.1$ cm^2/s). This would be interpreted as a displacement $\mid \Delta\vec{s} \mid$ of the order of $\approx$ 10 μm by the data reduction method. The corresponding velocity $\mid \vec{v} \mid = \mid \frac{\Delta\vec{s}}{\Delta t} \mid \approx$ 0,07 m/s is much smaller than the instantaneous velocities measured in this experiment, which are typically $\approx$ 5 m/s in the average (see Fig. 3.3). The resulting error is $<$ 2 % in the average. However, a displacement of $\approx$ 10 μm due to diffusion is not detected in the current experiment anyway, because the spatial resolution of the detector is 70 μm. Thus, the smallest measured velocity is about 70 μm / 150μs $\approx$ 0.5 m/s. The error determined in this way will be corroborated by the first validation test presented in the following section.

3.3.1 Validation tests

Molecular diffusion of the tracer is simulated by applying Ficks´s law numerically (in two dimensions) to measured LIF images in the following.

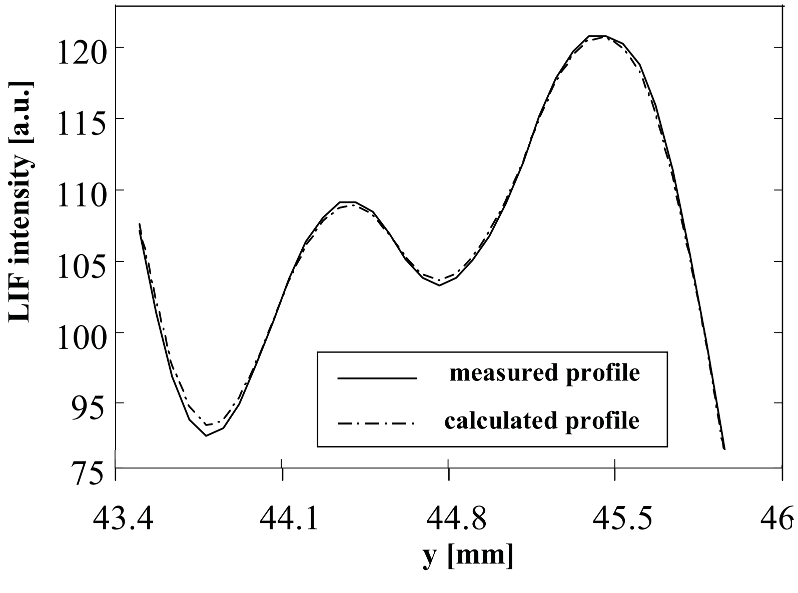

Figure 3.4: LIF intensity profile extracted from Fig. 3.2a) and calculated profile that shows a simulated diffusion process (the image in Fig. 3.2a was smoothed over 2x2 pixels before the first profile was extracted in order to suppress shot noise and to make the difference between the two profiles clearly visible).

The time step of the simulated diffusion process is chosen as the delay of the double-pulse measurements (150μs). A profile from a resulting simulated second image (based on Fig. 3.2a) is given as a second curve in Fig. 3.4. It can be seen that there is a weak influence of diffusion, in particular at minima and maxima of the signal intensity. The question remains if these slight differences lead to any considerable, apparent fluid motion, when the ICV data reduction method is applied to such image pairs. This test simulates an experiment where the velocity field is vanishing. The resulting velocity field determined from Fig. 3.2a) and the simulated second image (not shown) is depicted in Fig. 3.5.

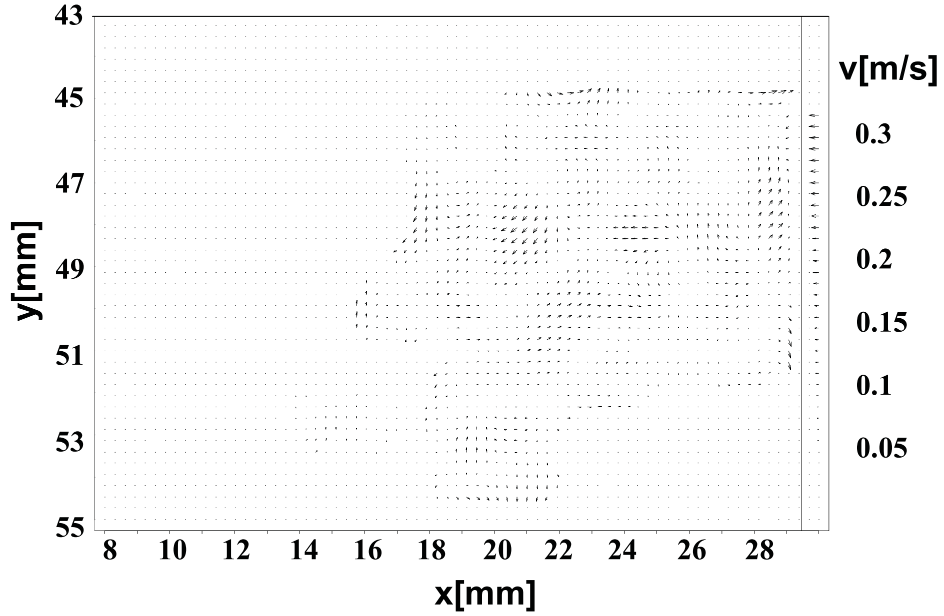

Figure 3.5: Apparent fluid motion due to molecular diffusion over a time interval of 150μs. This velocity field has been obtained by applying the ICV method to the LIF image in Fig. 3.2a) and a simulated second image (see text).

The same test has been performed with several other LIF images and the results are similar. It turned out that the averaged magnitude of the velocity vectors is 0.08 m/s (the standard deviation of the ensemble is 0.05 m/s). The "apparent" velocity magnitude determined in this way is comparable to the analytical result obtained in the last section. This corroborates that the apparent fluid motion caused by diffusion is much smaller than the detected, instantaneous gas velocities, which are typically ≈ 5 m/s. This corroborates that the error introduced by Fickian diffusion is smaller than 2 % in the average, and it is significantly smaller than other errors that will be determined in the following.

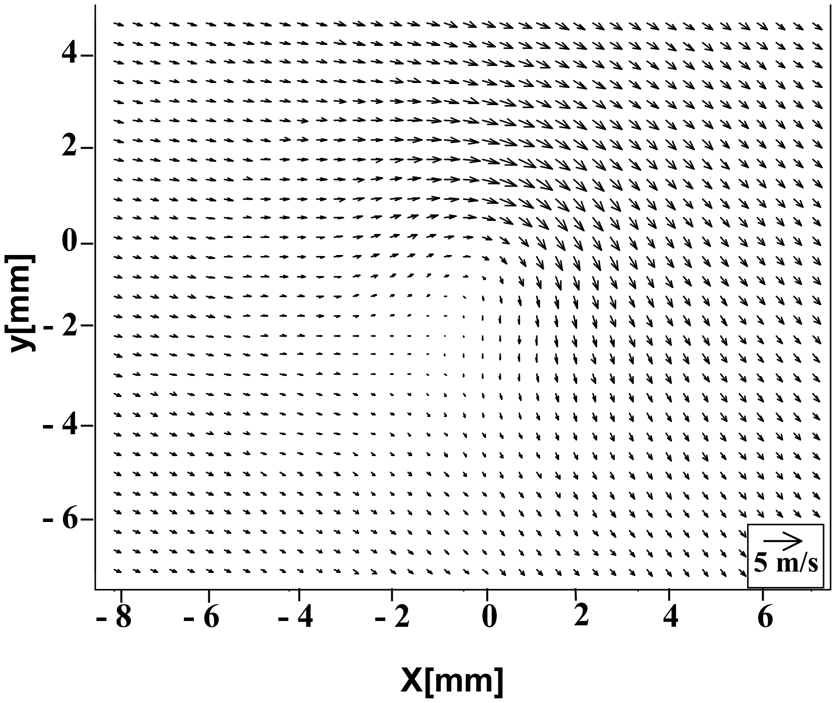

Figure 3.6: Simulated flow that has been generated by adding freestream components $v_y = 1.5$ m/s and $v_x = 2.3$ m/s to a Lamb-Oseen vortex with the parameters t = 120 ms, $\Gamma = 4$ mm^2/s.

The following validation test has been performed to check if the data reduction scheme is capable of resolving simulated flow fields based on the set of images acquired in this experiment. The second image of each image pair has been replaced by a simulated image, which has been computed by numerically-convecting the first image using a simulated flow field. In addition, a realistic amount of noise has been added to the second image in order to make the test more realistic (see below). This test assumes that molecular diffusion and out-of-plane motion are negligible. Molecular diffusion is a minor source of error as demonstrated above. Out-of-plane motion will be discussed separately below. A Lamb-Oseen vortex, the simplest viscous vortex, has been used as the basic simulated flow in this test ([67], and references therein). The velocity profile in polar coordinate system is given by the following analytic function, when the vortex core is located at r = 0 (ν = kinematic viscosity of air, t = time, Γ = circulation, r = radial distance):

$$v_\phi = \frac{\Gamma}{2\pi r}(1 - e^{-\frac{r^2}{4\nu t}}), v_r = 0 \tag{3.1}$$

The actual simulated flow used in this test has been generated by adding freestream components v_y = 1.5 m/s and v_x = 2.3 m/s (arbitrarily chosen) to a Lamb-Oseen vortex with the parameters t = 120 ms, Γ = 4 mm^2/s. The result is shown in Fig. 3.6. Similar vortical structures and freestream components have indeed been resolved in the present flow field (not shown). 40 LIF images measured in the range y = 4-6 cm (see Fig. 3.3) have been numerically-convected over a time step of Δt = 150μs using the flow field in Fig. 3.6. The origin of the coordinate system in Fig. 3.6, i.e. the center of the vortex, has been moved to random positions in the correlation volume of the 40 images. The simulated second image has also been degraded with noise, as mentioned above. Shot noise is the dominating source of noise in the present LIF images. It can be described by Poisson statistics ([61]). Thus, the root mean square deviation of a number of photoelectrons N (per pixel), which are amplified in the image intensifier, is given by $N^{1/2}$. Hence, the relative noise ("shot noise") is

$$\sigma_I = N^{1/2}/N = 1/N^{1/2} = (g/I)^{1/2} \tag{3.2}$$

where g is a gain factor, which describes the signal intensity I in terms of N, i.e., $I = g \cdot N$ (the gain factor g is known from a calibration of the camera system). The shot noise level in the present LIF images is σ_I = 3 % in the average (corresponding to N $\approx$ 1000 per pixel). Such an amount of shot noise has been added to the simulated second image. Thus, it is prevented that the algorithm tracks the high-wavenumber structure in the images, which is primarily due to shot noise. A resulting second image, which has been calculated based on Fig. 3.2a), is shown in Fig. 3.7.

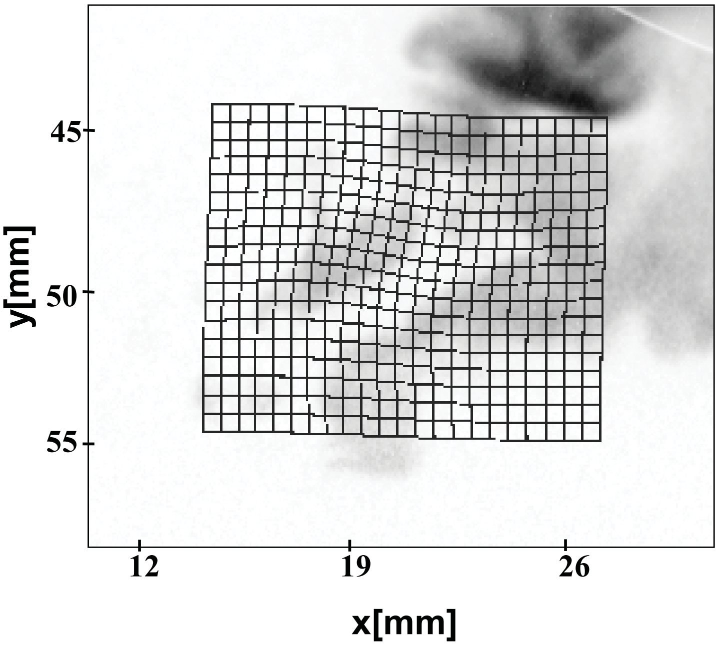

Figure 3.7: Simulated second image that has been calculated by numerically-convecting the tracer distribution given in Fig. 3.2a) according to the flow field in Fig. 3.6. The grid indicates the motion and distortion of the "fluid elements". The image has also been degraded with noise. The corresponding grey scale is shown in Fig. 3.2.

A grid has been introduced to visualize the motion and distortion of the "fluid elements" according to Fig. 3.6. The additional shot noise is hardly visible in the image. The data reduction scheme has been applied to the pair of images Fig. 3.2a) / Fig. 3.7. The resulting velocity field within the correlation volume is shown in Fig. 3.8. Again the velocity vectors have been suppressed in regions with low signal intensity. It can be seen that the resulting velocity vectors in Fig. 3.8 are very similar to the corresponding vectors shown in Fig. 3.6. The results obtained with a set of 40 LIF images are very similar: The mean deviation of the velocity vectors compared to the simulated flow field in Fig. 3.6 is 3.1 %.

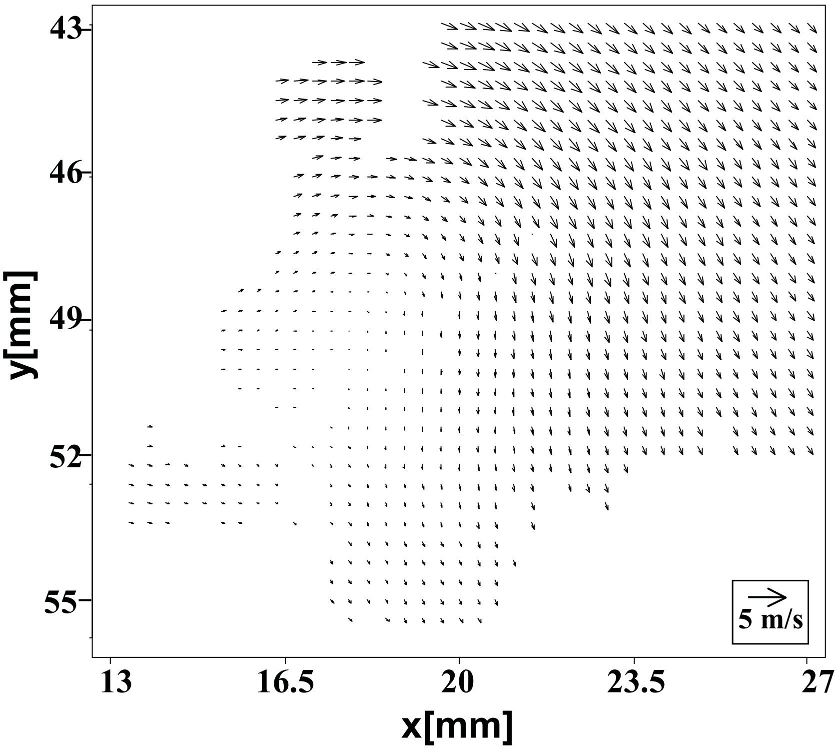

Figure 3.8: Velocity field resulting from the measured image depicted in Fig. 3.2a) and the simulated second image shown in Fig. 3.7. The deviation of the velocity magnitudes with regard to the corresponding vectors in Fig. 3.7 is about 3 %.

The spatial resolution of the current data reduction method corresponds to its "interrogation spot" size, similar to most PIV data reduction methods (see chapter 4). The validation test described so far has been performed with an interrogation spot size of 4x4 pixels. The corresponding spatial resolution is 280 μm in both directions. It is demonstrated in the following that the accuracy of the instantaneous velocity fields depends on the interrogation spot size. The test described before has been repeated several times with varying interrogation spot size. The resulting mean deviation of the instantaneous velocity vectors from 40 image pairs (with regard to the simulated flow field) are plotted in Fig. 3.9 as a function of spot size (see lower curve: "without smoothing"). It can be seen that the best accuracy (around 3 % error) is achieved with 4x4 or 8x8 pixel spot sizes. The error increases with larger spot sizes (16x16 or 32x32), because the spatial resolution is reduced in this case, so that larger errors due to insufficient resolution of the simulated flow field occur. On the other hand, Fig. 3.9 shows that the accuracy decreases if the spot size is further reduced beyond 4x4 pixels.

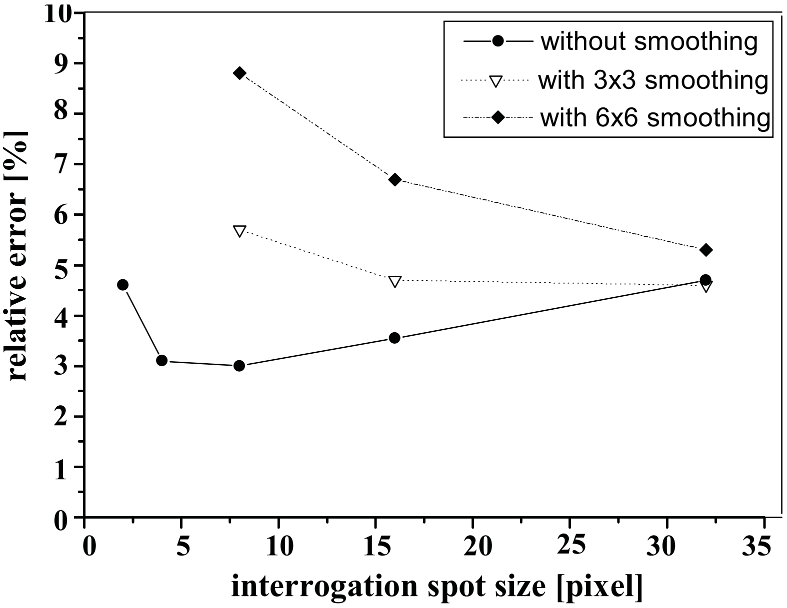

Figure 3.9: Relative error averaged over 40 instantaneous velocity fields as a function of interrogation spot size (in one dimension). Two of the curves have been obtained after smoothing the scalar images over 3x3 or 6x6 pixels, respectively, in order to suppress shot noise. The interrogation spot size corresponds to the spatial resolution (1 pixel =70 μm).

This behaviour is plausible, because such small interrogation spots do not contain sufficient information about the scalar field. However, it is remarkable that an accuracy of 4.7 % can be obtained with 2x2 pixel spot sizes, i.e. with a spatial resolution of 140 μm. This length scale is smaller than the length scale of the scalar field, which is about 1 mm. The reasons for this are explained in chapter 4. It should be noted that 2x2 or 4x4 pixel spot sizes can hardly be used for PIV analysis with conventional cross-correlation codes ([41]). This implies that such gas-phase velocity measurements require CCD cameras with fewer pixels than typical PIV cameras. The following tests have been done to investigate the influence of shot noise on the accuracy of the velocity data. In principle, shot noise can be reduced by averaging over neighbouring pixels, i.e., by smoothing the images, because the effective number of photoelectrons N per "detector element" is increased in this way. For example, N is increased by a factor of 9 by 3x3-smoothing, and the shot noise is reduced by a factor of 3 according to equation 3.2. Thus, the average shot noise is $\sigma = 1$ % in the 3x3-smoothed images, because it is 3 % in the original images. The same test as described before has been performed with 40 LIF images after 3x3 and 6x6 smoothing. The resulting accuracy of the velocity data is shown in Fig. 3.9 (upper curves). It can be seen that the errors are considerably larger compared to the case without smoothing (lower curve). This can be explained by the loss of spatial resolution (information) due to smoothing. It is clear that this is particularly severe for small interrogation spot sizes. Indeed the error increases for smaller spot sizes in the case of the smoothed images, as Fig. 3.9 shows. These results demonstrate that smoothing does not improve the accuracy of the present data set. Obviously, the loss of information about the tracer distribution within individual interrogation spots is more important than the reduced shot noise. In other words, shot noise is less important than the structure in the scalar field. Thus, the accuracy and spatial resolution of such measurements could not be improved considerably by larger signals.

3.3.2 Determination of velocity data from the spray

The validation tests indicate that satisfactory accuracy of the instantaneous velocity fields can be achieved with 280 μm resolution, provided that there is no out-of-plane motion. However, the flow field is generally turbulent in the present experiment, although the fluid motion can be expected to be predominantly in the measurement plane, due to the symmetry of the set-up. It is clear that the measurement accuracy is affected if a certain fraction of the tracer molecules probed by the first laser pulse leaves the light sheet before the second laser pulse. A similar problem arises when two-dimensional PIV measurements are performed in turbulent flows, i.e., when some of the illuminated seed particles do not reside in the light sheet for both light pulses ([41]). It is generally required that the displacement of the tracer molecules (or particles) in the z direction $s_z = v_z \cdot \Delta t$ is much smaller than the width w of the light sheet, in order to obtain a high measurement accuracy. In principle, this can be achieved by a short delay Δt and a large w. However, Δt is limited by the condition $\Delta t > \Delta s_{min} / v_{min}$, where Δs_{min} is the smallest displacement resolved by the detector (≈ 70 μm), and v_{min} is the smallest velocity to be measured (in x or y directions).

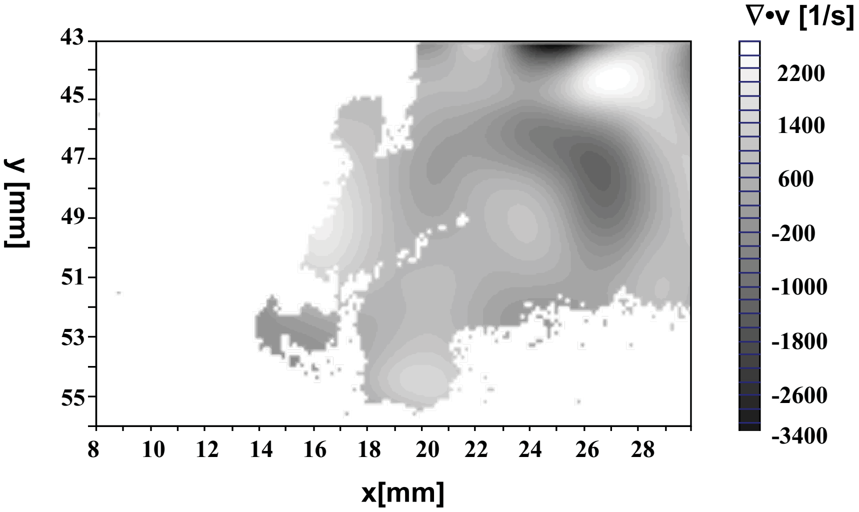

Figure 3.10: Divergence field $\nabla \cdot \vec{v} = \partial_x v_x + \partial_y v_y$ of the instantaneous velocity field given in Fig. 3.3.

In addition, a thick light sheet is often not acceptable because this affects the spatial resolution in the z direction, and the measured tracer distributions may become smooth due to averaging in the z direction. Thus, the condition $v_z \cdot \Delta t << w$ is generally not fulfilled in the present experiment, so that out-of-plane motion can not be neglected. An alternative, preliminary approach is used to identify those regions in the velocity fields where the data are in error because considerable v_z occurred. It is assumed that out-of-plane motion can be identified by the divergence field $\nabla \cdot \vec{v} = \partial_x v_x + \partial_y v_y$. The gas phase can be regarded as a non-reacting, incompressible fluid in this experiment. Thus, non-vanishing divergence is an "artifact" caused by normal velocity components v_z. It is true that there may be cases of out-of-plane motion with vanishing divergence. However, the present approach is based on the assumption that it is simply unlikely that the divergence vanishes when there is significant out-of-plane motion, because two different, random tracer distributions are probed by the two light pulses. Hence, it is assumed that most regions with considerable v_z can be identified in this way.

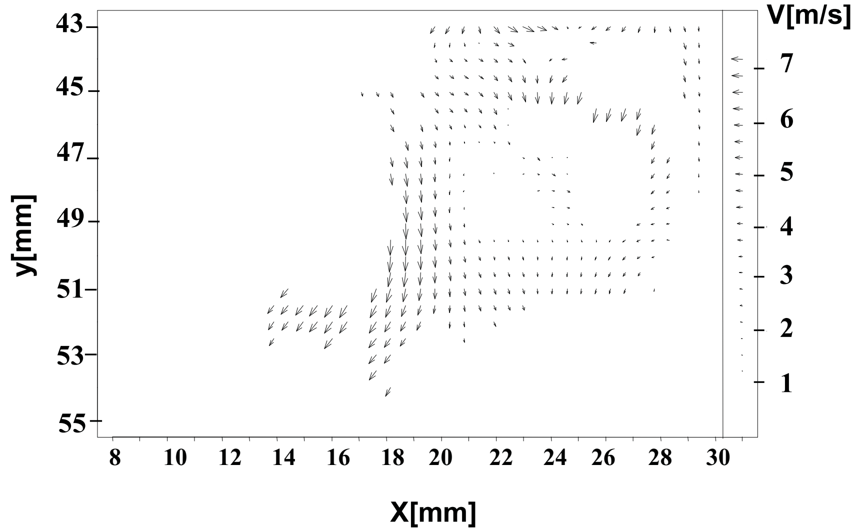

Figure 3.11: Remaining velocity data of Fig. 3.3 after suppression of the vectors in regions with high divergence according to Fig. 3.10 (threshold: ±1000/s).

All the velocity vectors have been suppressed in the instantaneous velocity fields, where the divergence is beyond a certain threshold. We have not quantified the error introduced by this procedure. More sophisticated strategies to suppress the velocity vectors, which are erroneous due to out-of-plane motion, should be developed in the future. The divergence field of the velocity field in Fig. 3.3 is shown in Fig. 3.10. The threshold for suppression of the velocity vectors is chosen as ± 1000/s. This threshold is comparable to the divergence that occurred in the simulated (purely two-dimensional) flow fields of the validation tests described in the previous section. Thus, it can be assumed that a large fraction of the velocity vectors with considerable v_z components have been erased by this procedure. The remaining velocity vectors of Fig. 3.3 are depicted in Fig. 3.11. The validated velocity data from 2 x 20 instantaneous velocity fields measured between y = 4-6cm, and y = 8-10cm, respectively, have been averaged to generate the mean velocity fields, which are given in Fig. 3.12. The mean velocity field determined in this way is erroneous when the turbulence is not isotropic, because the eddies, which exhibit considerable normal components v_z, have been suppressed. The resulting error depends on the structure of the particular flow field and can not be exactly quantified here. However, some expected features of the mean velocity field, in particular close to the edge of the spray, can be observed in Fig. 3.12. The spray cone, as determined from Mie scattering, is outlined by the broken lines. The velocity magnitudes in Fig. 3.12 are smaller than 1 m/s, in contrast to the instantaneous velocity fields, due to averaging. It can be seen in Fig. 3.12 a)&b) that much higher air velocities occur within the spray and near the spray cone than in the ambient air. This is caused by the influence of the droplet motion. The "chaotic" structure of the mean flow field within the spray in Fig. 3.12 a) is caused by insufficient averaging, because the data were averaged over 20 velocity fields only. The flow field within the spray in Fig. 3.12 b) indicates that the mean fluid motion is downstream here. Obviously, the gas "follows" the droplets in this region. The velocity field within the spray is much more consistent in Fig. 3.12 b) than in Fig. 3.12 a), because the turbulence level is lower and consequently smaller errors occur due to insufficient averaging. In principle, the spatially-resolved "turbulence" level of flow fields can be determined from instantaneous velocity fields by calculating the standard deviation of the velocity from shot to shot at any given point. The turbulence field resulting from the present data set is not presented, because the available set of instantaneous velocity fields is too small. However, the "large scale" structure in the turbulence intensity can be determined roughly, based on the present data. It turned out that the turbulence intensity close to the edge of the spray is about a factor of two larger within the spray compared to the ambient air. The turbulence enhancement in sprays is well known.

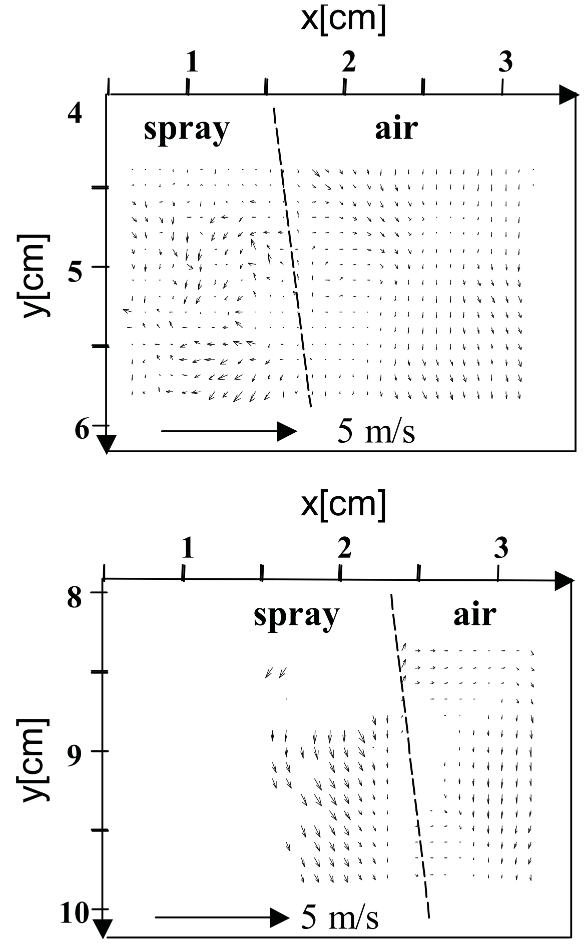

Figure 3.12: Mean velocity fields measured in the spray and in the ambient air at y = 4-6 cm (a) and y = 8-10 cm (b) downstream from the nozzle. The dotted line shows the approximate position of the spray cone. The largest velocity vectors are around 0.5 m/s.

3.4 Summary and Conclusions

It is demonstrated that instantaneous velocity fields of the continuous phase can be measured in (dilute) sprays by the present technique. In contrast to PIV, it is based on a gaseous flow tracer, such as NO, and laser-induced fluorescence (LIF). This is one of the very few techniques that can, in principle, also be applied to spray flames, because NO is sufficiently stable at high temperature. The frequency shift of the LIF with regard to the excitation wavelength is exploited to discriminate it against Mie scattering from the dispersed phase. Inhomogeneous tracer distributions, which are required for tracing the flow field, are generated by an incomplete, turbulent mixing process. Validation tests indicate that the mean error of the instantaneous velocity fields is of the order of 5 %, provided that the flow field is essentially two-dimensional. This accuracy is comparable to the results of an experimental validation of the same measurement technique, which is described in chapter 4. The validation tests demonstrate that the accuracy depends on the spatial resolution as expected. It turns out that the accuracy is close to the optimum with 280 μm resolution. The accuracy decreases if the spatial resolution is further improved. It is also demonstrated that this is not caused by image noise, but it is due to lacking structure in the tracer distributions. The influence of molecular diffusion is also investigated, and it turns out that this is a minor source of error, as long as the measured fluid motion is much larger than 0.1 m/s (at $T = 300$ K). Other potential sources of error are discussed in the sections 3.3.1 - 3.3.2. Although the mean velocity fields determined are affected by errors due to out-of-plane motion and insufficient averaging, they reflect some expected features of the gas flow close to the edge of the spray. Further work is needed to quantify and reduce the errors due to out-of-plane motion. Furthermore, the dynamic range of the gas-phase velocimetry should also be discussed in the future, because it is an important issue.

Chapter 4

Probing the Velocity Fields of Gas and Liquid Phase Simultaneously in a Two-Phase Flow

The feasibility of simultaneous measurements of the instantaneous velocity fields of gaseous and liquid phase is demonstrated in a laminar, unsteady two-phase flow. Thus, the instantaneous relative velocity field can be measured in such media. This is achieved by combining Gaseous Image Velocimetry (GIV) and Particle Image Velocimetry (PIV) techniques. The GIV technique is based on laser-induced fluorescence (LIF) from gaseous tracers. The wavelength shift of LIF is exploited to separate it from Mie scattering from the liquid phase. The GIV and PIV measurement systems work independently in this approach. Thus, the measurement accuracy and precision of the GIV technique can be validated by comparing it to the PIV results in regions of the flow field where the relative velocity vanishes.

4.1 Introduction

It is desirable to measure the velocity fields of both phases in two-phase flows in order to study their interactions. For example, the relative gas-liquid velocity is important for the secondary break-up and evaporation of droplets in sprays. Furthermore, it is advantageous to measure both velocity fields simultaneously, so that the interactions can be studied on a "single-shot" basis, in particular in unsteady, non-reproducible two-phase flows. It has been demonstrated in chapter 3, that the Gaseous Image Velocimetry (GIV) technique can be used for measuring instantaneous velocity fields of the gas phase in sprays. It is demonstrated, that the velocity fields of gas and liquid phase can be measured simultaneously in an aerosol by combining GIV with Particle Image Velocimetry (PIV). This yields the instantaneous relative velocity field. The acronym GIV was introduced to distinguish it from the related PIV method: PIV is based on discrete flow-tracing particles, whereas GIV is based on a gaseous tracer. In addition, PIV has the potential to be employed to measure the velocity field of any gaseous, liquid or solid phase (continuous or dispersed) in different applications, whereas GIV aims to measure the velocity of the gas phase only. Apart from that GIV works similar to PIV. Double-pulse imaging of laser-induced fluorescence (LIF) from the gaseous tracer is used in the present experiment. The velocity field is computed from the LIF images, essentially, by using the OFA presented in chapter 2 which is mainly based on the Image Correlation Velocimetry (ICV) method presented by Tokumaru and Dimotakis (1995). Thus, GIV may be regarded as a special application of data processing *à* la "optical flow". However, the ICV method, and similarly the Scalar Image Velocimetry (SIV) method proposed by Dahm et al. (1992) and the method used by Maas (1993), are methods to extract the velocity field from any measured, dynamically passive, conserved scalar field, i.e., these methods can in principle be applied to gaseous tracers or particles in gases or liquids. These methods are data reduction procedures, whereas GIV is rather an experimental technique. It should be noted that very different experimental problems are encountered when such measurements are performed with gases, particles, or liquids, respectively. The GIV technique focuses on the problems encountered with gaseous tracers in the gas phase. Specifically, enhanced molecular diffusion of the tracer is a major problem in this case, so that a special experimental technique is required. For example, it is generally necessary to acquire consecutive images with a much smaller delay than in the experiments of Dahm et al. (1992), Maas (1993) and others, who did velocity measurements using molecular tracers in liquids. Diffusion of a gaseous tracer also causes more difficulties in sustaining inhomogeneous tracer distributions, which are required for tracing the velocity field. Further consequences of diffusion are discussed in chapter 3. Related experimental techniques for measuring the gas-phase velocity using gaseous tracers are also discussed in this chapter. GIV can be combined with PIV, based on Mie scattering from the dispersed phase, in sprays or aerosols, because the wavelength shift of LIF with regard to Mie scattering is exploited to separate GIV and PIV signals by optical filters. Very few non-intrusive measurement techniques are capable of providing instantaneous velocity fields of gaseous and liquid phase simultaneously. A review on the application of PIV to multiphase flows is given elsewhere ([54]). Digital image processing can be applied to distinguish both phases in two-phase flows if the particles seeded to the continuous phase are much smaller than the particles of the dispersed phase ([50], [52]). However, the droplet size spectrum in many sprays and aerosols includes small particles, so that it is often difficult to find much smaller seed particles. In this case two-colour PIV based on fluorescent seed particles can be used in some applications ([25], [56], [57]). However, it is generally difficult to discriminate LIF against Mie scattering from the dispersed phase if it contains large particles ([1], [48], [55]). Mie scattering from large particles may be many orders of magnitude stronger than any LIF, so that it is difficult to suppress it by today´s optical filters. These problems could be overcome by gaseous tracers, because they yield continuous signals: Continuous signals could be separated from discrete Mie scattering from large particles by image processing, as long as the large particles are identified. However, this is not demonstrated here. It should be emphasized that GIV based on nitrous oxide (NO) as the tracer is one of the very few 2D techniques that can in principle also be applied to flames and burning sprays. This was demonstrated previously in a hydrogen diffusion flame ([40]). NO is sufficiently stable in combustion, even at $T>2500K$, where most light seed particles lose their capability of providing sufficient Mie scattering. It is also well known that gaseous tracers have a better ability to follow the flow with large velocity gradients or very low velocities. A commercial PIV measurement system (LaVision) is used, and care is taken that the PIV measurements are not disturbed by the simultaneous GIV measurements. Thus, the PIV system yields reliable results, which can be used to validate the accuracy and precision of the GIV data in certain regions of the flow where the relative velocity is vanishing. The single-shot precision of these particular GIV measurements turns out to be 6-7%. The error of the temporally averaged GIV data is less than 2%, and the deviations from the averaged PIV data are dominated by particle lag.

4.2 Experimental

The measurements presented are performed in a water aerosol embedded in a laminar, unsteady, two-dimensional flow field, which is highly reproducible. No problems with out-of-plane motion occur in this two-dimensional flow field using planar GIV and PIV methods. The whole set-up is shown in Fig. 4.1.

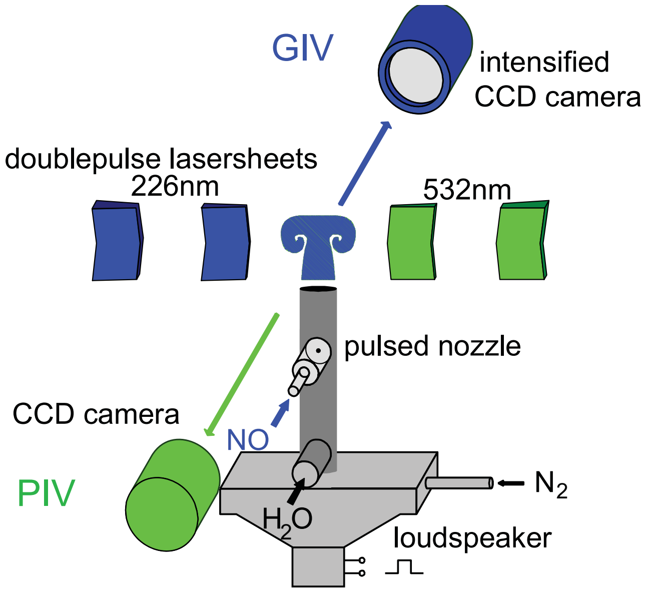

Figure 4.1: Experimental set-up of combined GIV and PIV measurements applied to a laminar unsteady flow field produced by a vortex ring generator.

A two-dimensional (axisymmetric) flow field is generated by a vortex ring generator, i.e., by briefly discharging nitrogen gas into room air from a round orifice ([53], [49]). The vortex ring generator basically consists of a tube with an open end (orifice diameter 25mm) and a speaker connected to the other end. The speaker can be triggered independently relative to the measurements. The planar laser measurements are done in the central plane of the resulting flow field. The tracer gas (NO) is seeded into the tube (sub-percent volume fraction) a short time before the speaker is triggered using a pulsed valve as shown in Fig. 4.1. This seeding method yields inhomogeneous NO distributions in the vortex bubble, which are exploited for determination of the velocity field. Water aerosol from an ultrasonic aerosol generator is also seeded into the tube via another inlet. This inlet is upstream from the NO inlet, so that the aerosol distribution in the vortex bubble is rather homogeneous. The aerosol generator operates at 1.7 MHz. This yields a narrow log-N droplet diameter distribution (standard deviation $\sigma_g \approx 1.5$) in the range 2-5 μm (count-median diameter: $d_{50,0} \approx 3$ μm, see [58]; [51]). The major components of the GIV measurement system are two tunable KrF excimer lasers (Lambda Physik) and an intensified progressive scan CCD camera. The excimer lasers generate two consecutive laser pulses at 248 nm, which can be fired independently. The typical delay in these measurements is 100 μs. Stimulated Raman scattering in two high pressure cells filled with hydrogen is used to shift the wavelength of the laser beams from 248 nm to 226 nm, where NO can be excited via the $\gamma(0,0)$ band system ([38]). The resulting 226 nm beams are formed to sheets. The probe area is imaged onto the CCD camera with a demagnification of 2:1. The progressive scan CCD camera (LaVision) is capable of recording two images with a delay down to 1μs. The camera is equipped with an image intensifier, so that ultraviolet LIF can be detected efficiently. The intensified camera is also equipped with an optical filter in order to suppress Mie scattering at 226 nm from the water aerosol. A 10 mm layer of liquid butylacetate is used as the filter. This attenuates the Mie scattering by at least four orders of magnitude. The remaining Mie scattering is negligible compared to the LIF signals from NO. A complete commercial PIV measurement system including software (LaVision) has been added to this set-up, so that independent PIV and GIV measurements can be performed simultaneously. The PIV system consists of a double-pulse frequency-doubled Nd:YAG laser system and a progressive scan CCD camera, which is not equipped with an image intensifier in contrast to the GIV camera. The first GIV laser is fired a short time (1 μs) after the first PIV laser pulse, and the second GIV laser is fired after the second PIV pulse, so that the laser-induced emissions of the PIV system do not disturb the GIV system and vice versa. However, the delay is so short that the measurements can be regarded as simultaneous. Similar PIV measurements could have been done by the GIV measurement system, by removing the Mie filter. Furthermore, simultaneous GIV and PIV measurements with only two lasers and one camera should be possible by splitting the camera and using one half for GIV and the other for PIV. However, the present set-up was chosen in order to avoid any interferences between the measurements. Thus, the PIV measurements are reliable and can be used for verifying the accuracy of the GIV system. The velocity field of the gas phase is determined from the NO images, essentially, by using the OFA from chapter 2 based on the ICV method proposed by Tokumaru and Dimotakis (1995) as mentioned before. Only a brief description of the method is given in the following, and the reader is referred to their paper and to the chapters 2 and 3 for more details. The method assumes that the image intensities $I_1(x)$ and $I_2(x)$ in the two images represent the true NO density. It is also assumed that the motion of the tracer molecules is solely due to convection, i.e., diffusive effects are negligible. It is demonstrated in a previous paper that diffusion is indeed negligible in such experiments under similar conditions, i.e. with NO in room air and delays of about Δt = 0.1 ms between the two images ([27]). In memory of chapter 2 the velocity field is determined as follows: Essentially a mapping function $\Delta\vec{s}(\vec{x})$ is found that maximizes a correlation between the two scalar fields. The mapping function represents the displacement of the fluid elements, and corresponds to the velocity field through $\vec{v}(\vec{x}) = \Delta\vec{s}(\vec{x})/\Delta t$. Specifically, the mapping function $\Delta\vec{s}(\vec{x})$ is optimized so that the signal intensity distribution $I_1(x)$ in the neighbourhood (interrogation spot) of any position x in the first image is best mapped into the intensity distribution $I_2(\vec{x}+\Delta\vec{s})$ in the neighbourhood of $\vec{x}+\Delta\vec{s}$ in the second image. Essentially, this is achieved by minimization of the cost function:

$$C(\Delta\vec{s}) = \int (I_2(\vec{x}+\Delta\vec{s}) - I_1(\vec{x}))^2 d\vec{x} \tag{4.1}$$

The integration is performed, in principle, in the whole correlation volume, i.e. in a fraction of the images where the velocity field is to be determined. In addition, smoothness of the velocity field is enforced, corresponding to the Navier-Stokes equations. Each interrogation spot ("fluid element") is subject to translation and deformation in this representation of the velocity field.

4.3 Results and Discussion

Fig. 4.2 depicts a sequence of typical GIV double-pulse raw images, that have been measured at t = 3ms (a), 4.5ms (b), 6ms (c), and 7ms (d) after triggering the speaker. The LIF from NO shown in these images marks the fluid discharged from the vortex ring generator. The orifice is located at the lower edge of these images. These double-pulse images have been recorded with a delay of $\Delta t = 0.1$ ms.

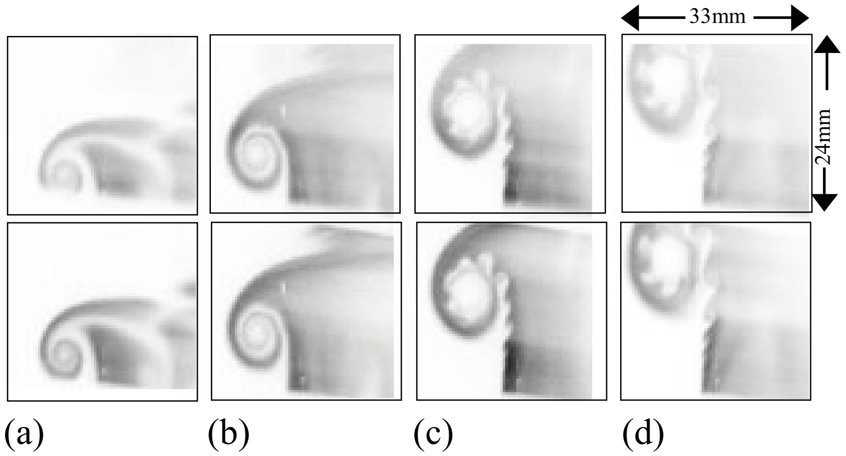

Figure 4.2: Typical GIV double-pulse raw images (LIF from NO) measured at t = 3ms (a), 4.5ms (b), 6ms (c), and 7ms (d) after triggering the speaker. The upper frame of each pair corresponds to the first laser pulse and the lower frame to the second pulse, that has been recorded with a delay of $\Delta t = 0.1$ ms.

The images are highly reproducible as demonstrated below. Only one half of the generated vortex bubble can be seen with this field of view (33 mm x 26 mm). The sequence of images shows how the vortex bubble is formed.

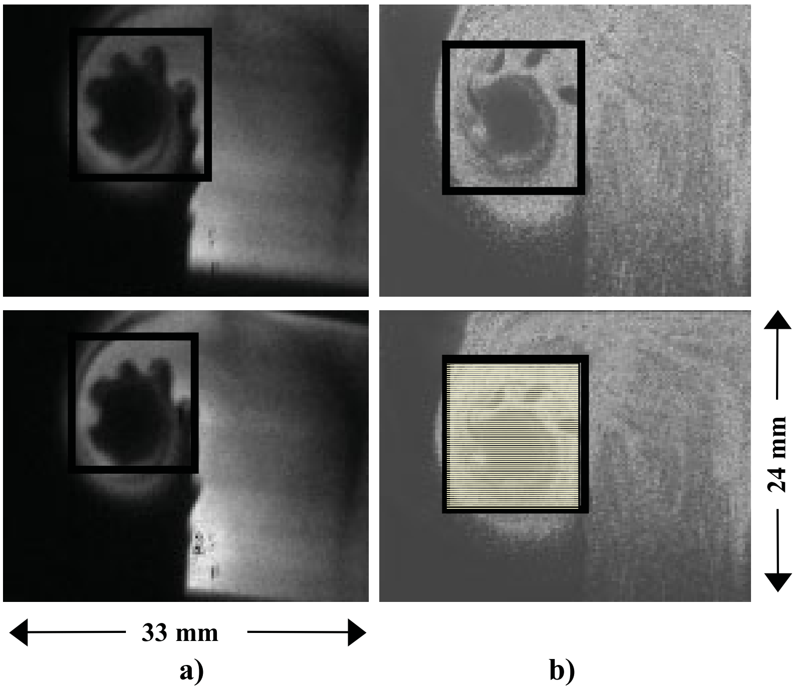

Figure 4.3: A complete set of instantaneous GIV/PIV raw images. The images in the upper row, and the lower row respectively, have been recorded quasi simultaneously. The inner rectangles correspond to 12.4mm x 12.4mm.

Obviously the delay of $\Delta t = 100$ μs is small compared to the time scale of the fluid motion. It can also be seen in Fig. 4.2 c) & d) that there are many small vortices formed along the shear layer of the discharged fluid and the ambient air due to the Kelvin-Helmholtz instability. The velocity fields shown in the following have been measured at t = 6 ms after triggering the speaker. A complete set of instantaneous GIV/PIV raw images is depicted in Figure 4.3. The images in the upper row, and the lower row respectively, have been recorded (quasi) simultaneously. The data evaluation described in the following is performed in a fraction of these images, the so called correlation volume, as indicated by the inner rectangles (12.4 mm x 12.4 mm). The GIV data reduction can not be performed throughout the whole images because of lacking inhomogeneities in the LIF signal or lacking signal intensity. Figure 4.4 a)&b) shows two GIV and PIV single shot images with the smaller field of view.

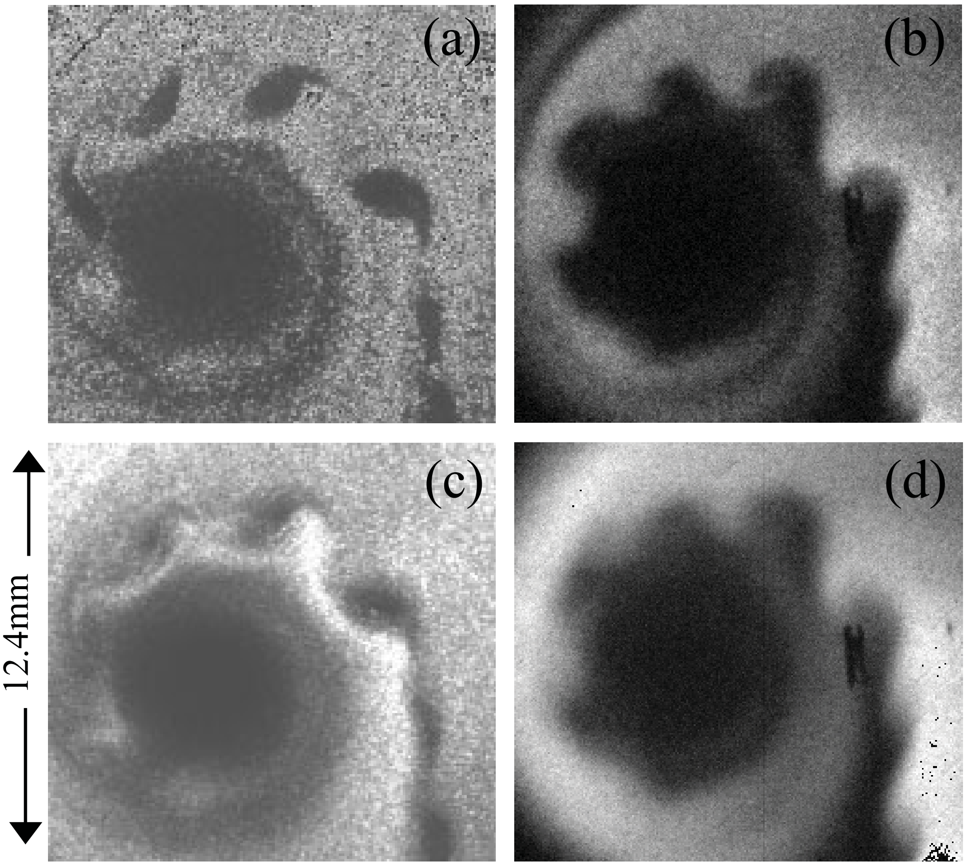

Figure 4.4: Two single-shot (a&b) and averaged (c&d) GIV and PIV images. The field of view corresponds to 12.4mm x 12.4mm.

For comparison two GIV and PIV images averaged over 10 single shot measurements are displayed in Figure 4.4 c)&d). It can be seen that the single shot images and the averaged images are very similar. This indicates that the fluid motion is highly reproducible as expected. It should be noted that the NO and droplet distributions shown in Fig. 4.3 cover different areas, although both stem from the fluid discharged by the vortex ring generator: The vortex bubble, which is indicated by the NO distribution, is significantly smaller than the corresponding droplet distribution. Obviously the droplets do not follow the vortical motion of the gas perfectly and tend to leave the vortex core. This can be seen more clearly in the velocity fields discussed in the following. Velocity-tangent (streamline) fields averaged over 10 instantaneous measurements at t = 6ms are depicted in Figure 4.5.

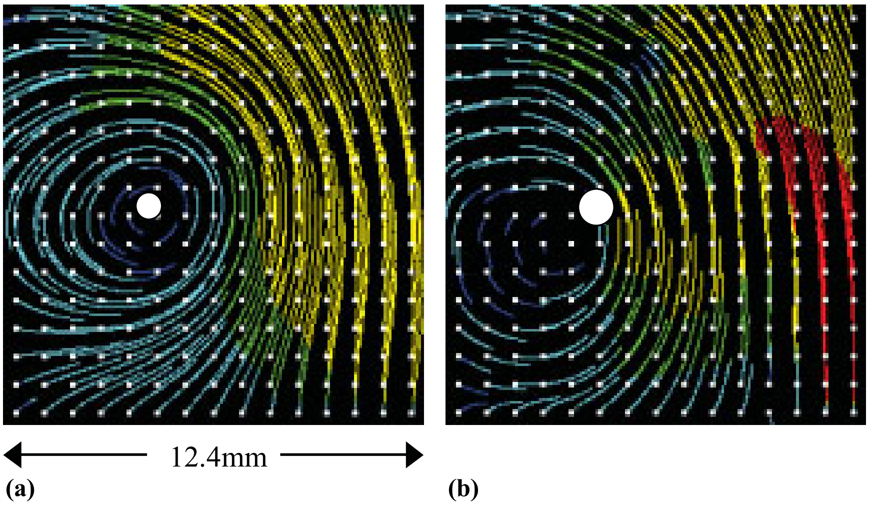

Figure 4.5: Temporally averaged streamline patterns of simultaneously measured GIV (a) and PIV (b) data; the large white dot indicate the center of the vortical motion of the gas-phase.

GIV data are given in the left panel, and simultaneously measured PIV data in the right panel respectively. The spacing of the small white dots, which are the starting points of streamlines, corresponds to 0.8mm in real space. This is equal to the spatial resolution of the PIV data using interrogation spots of 32 x 32 pixels. The spatial resolution of the GIV technique, as determined by the resolution of the data evaluation, is 1 mm in this particular data set. This resolution is sufficient to resolve the prevalent fluid motion. The fluid velocity is directed upwards on the right hand side of each panel in Fig. 4.5, i.e., in the stem of the vortex bubble. The strong vortical motion is anti-clockwise. The center of the vortical motion in the GIV data is marked by a large white dot in both panels. Obviously the droplets to do not rotate about this point due to their inertia. Also the droplets lag behind the steep change in the velocity direction near the upper right corner of the streamline patterns. Obviously, the PIV data do not describe the gas motion accurately in most regions of this flow field. Thus, the quantitative comparison of GIV and PIV data is made only in the stem of the vortex bubble, where particle lag is expected to be smallest. The averaged velocity data in this region are shown in Figure 4.6.

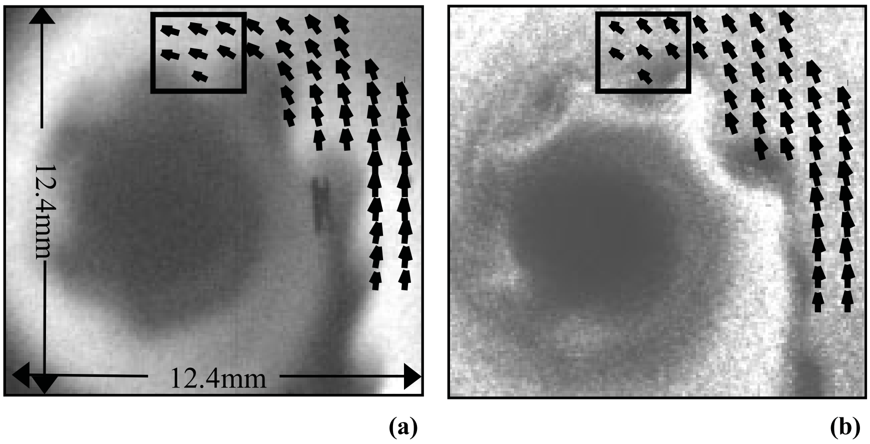

Figure 4.6: Temporally averaged GIV (a) and PIV (b) data in regions of the flow where particle lag is relatively small.

GIV data are given on the left hand side and PIV data on the right hand side, respectively. The data show that there is excellent agreement of GIV and PIV data in the lower part of the stem, but there are significant angles between the velocity vectors near the upper right corner, in particular in the rectangles shown in this area. The data in these rectangles are discussed in the following. The particle lag in a forced circular air flow is discussed in the literature ([47]). If the tangential velocity of the particles is equal to the fluid velocity and Stokes´ friction equals the centrifugal force the ratio of radial and tangential velocities is

$$\frac{v_r}{v_t} = (\omega_r d_p^2 \rho_p)/(18\mu) \tag{4.2}$$

where ω_r = angular frequency (of the vortex core), d_p = particle diameter, ρ_p = particle density, and μ = viscosity. In this simple model v_t corresponds to the GIV data and the combination of v_r and v_t to the PIV data, respectively.

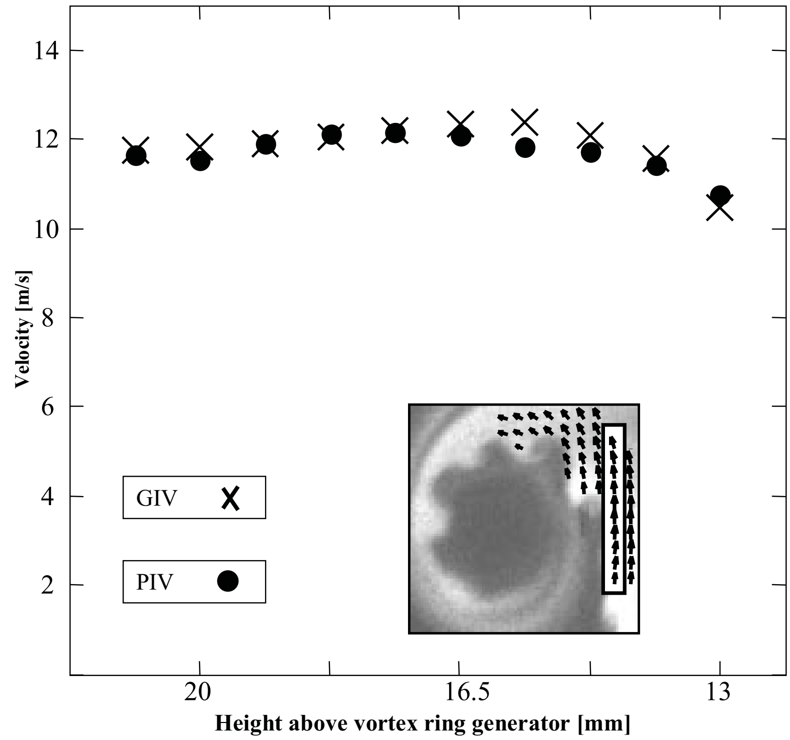

Figure 4.7: Vertical profile of temporally averaged GIV and PIV data taken from the velocity fields given in Fig. 4.6. The exact position of the profile is indicated in the small image.

Thus, the angle between v_r and v_t is expected to be the angle between PIV and GIV velocity vectors. The angle between the PIV and GIV velocities averaged over the data in the rectangles shown in Figure 4.6 equals 17°. The angular velocity of the vortical motion equals $\omega_r \approx 2000/\mathrm{s}$ in the present experiment. Under this condition equation 4.2 yields an angle of 17° between both velocity components v_r and v_t, when the droplet diameter is assumed to be $d_p \approx 3\ \mu\mathrm{m}$. This d_p corresponds nicely to the count-median droplet diameter of the aerosol $d_{50,0} \approx 3\ \mu\mathrm{m}$ (see "Experimental"). It can be concluded that the measured angle between PIV and GIV data in this region of the flow agrees well with the theoretical result. Thus, the large difference in the averaged GIV and PIV data can be explained by this simple model, although it does not take unsteady effects into account. The accuracy of the velocity magnitudes are discussed in the following.

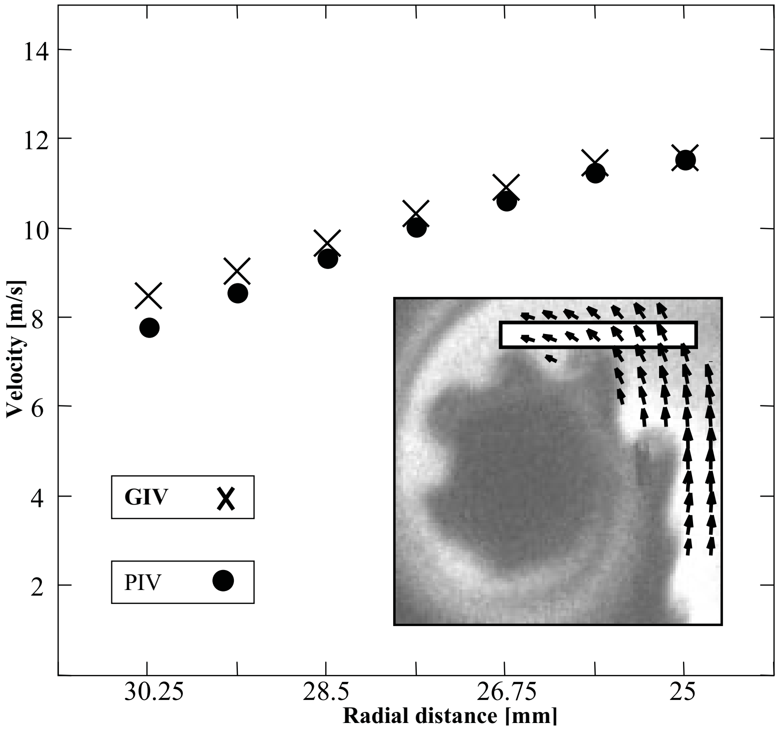

Figure 4.8: Horizontal profile of temporally averaged GIV and PIV data taken from the velocity fields given in Fig. 4.6. The exact position of the profile is indicated in the small image.

The averaged deviation of the GIV and PIV velocity magnitudes shown in Fig. 4.6 equals 3.3%. The profiles shown in Figures 4.7 & 4.8 are taken from specific columns and rows, respectively, from Fig. 4.6. These profiles show that the deviation is at least partly due to particle lag: The deviation in the vertical profile in the stem (Fig. 4.7) equals 1.8%, which is much smaller than the deviation in the horizontal profile (Fig. 4.8) that is 3.6%. This corroborates that the particle lag is smallest in the stem as expected. Indeed the velocity magnitudes measured by PIV are significantly lower than the GIV data towards the left hand side of the profile in Fig. 4.8. It can be concluded that the systematic error in these temporally averaged GIV measurements is smaller than 2% at least in the stem. This error can not be determined more precisely here because the PIV data are affected by particle lag. The precision of the instantaneous velocity measurements is discussed in the following.

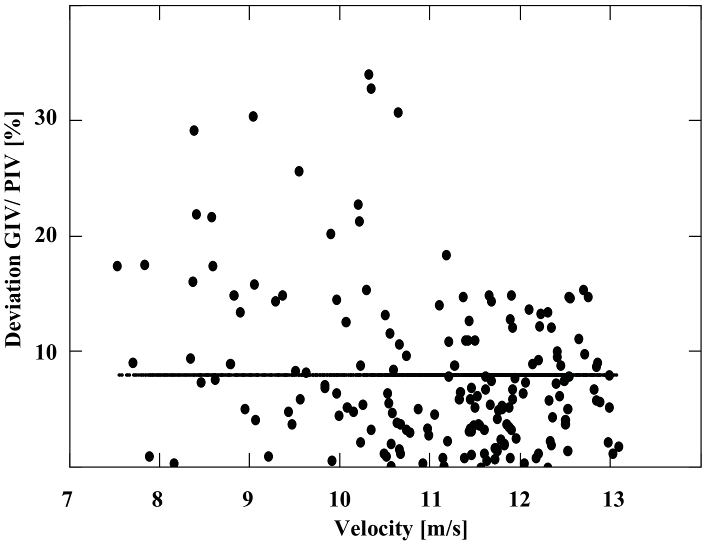

Figure 4.9: Instantaneous GIV/PIV deviations taken from 10 measurements; the horizontal line indicates the mean value = 8.0%.

The relative deviations of the data from 10 instantaneous GIV and PIV measurements (normalized by the arithmetical mean of GIV and PIV data) are given in the scatter plot in Figure 4.9. The data are taken from the same region of the flow field where the averaged measurements have been compared as depicted in Figure 4.6. It can be seen in Fig. 4.9 that smaller velocity magnitudes appear to be affected by larger deviations. This correlation can be observed more clearly in Figure 4.10, where the same data are given by averaging over velocity intervals, i.e., 7-8m/s, 8-9m/s, ... , 12-13m/s. However, this does not imply that instantaneous GIV or PIV measurements are generally less precise with smaller velocities, but it is again caused by particle lag in this particular set-up: Smaller velocities occur in the upper region of the observed flow field, where large angles between the liquid and gas-phase velocities occur. Thus, it is not surprising that the instantaneous velocity magnitudes are also different there. A similar correlation of velocity magnitude and the GIV/PIV deviation can also be seen in the averaged data shown in Figure 4.8. Hence, larger deviations in smaller velocity magnitudes seen in Fig. 4.9 do not indicate that instantaneous measurements are generally less precise. The average of the instantaneous GIV/PIV deviations in Fig. 4.9 equals 8.0%, as indicated by the horizontal line. This is considerably larger than the deviation of the time averaged measurements, which are dominated by particle lag. Thus, the instantaneous deviations are predominantly caused by other factors, e.g., noise in the single-shot images. Hence, the single-shot GIV error can be determined from the PIV/GIV deviation by subtracting the single-shot PIV error. The latter can be approximately quantified by determination of the shot-to-shot variations in the instantaneous PIV results, assuming that the flow field is perfectly reproducible. The instantaneous PIV error determined in this way equals 3.6% in the present data set.

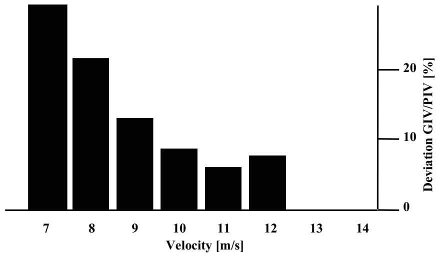

Figure 4.10: Instantaneous GIV / PIV deviations averaged over velocity intervals 7-8m/s, 8-9m/s, ... , 12-13m/s.

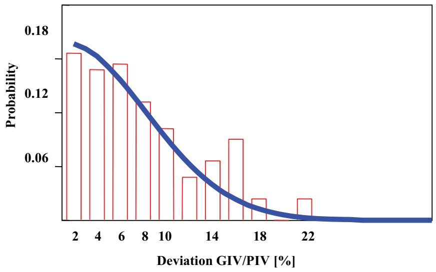

Figure 4.11: Probability density function of the instantaneous GIV / PIV deviations including a Gaussian fit (FWHM/2 = 8.5%).

This implies that the instantaneous GIV error is 7.1%, so that the total deviation adds up to 8%. The instantaneous GIV error can also be estimated from the shot-to-shot variations in the instantaneous GIV results, which are 6.1% in the present data set. These results agree quite nicely and it can be concluded that the error in these instantaneous GIV measurements equals 6-7%. The same data as in Figure 4.9 are plotted as a probability density function in Figure 4.11. It can be seen that the p.d.f. is roughly Gaussian as indicated by the thick curve, and the width at half maximum equals 8.5%, which is comparable to the 8.0% mean deviation of the data. It can be assumed that the GIV error in the remaining parts of the measured flow field, which were not taken into account in the preceding analysis, is similar to the error determined before, provided that the LIF signal intensities and their spatial inhomogeneities are sufficient. The dependence of the GIV accuracy on these features of the LIF signals is discussed in detail in chapter 3. It is clear that larger GIV errors will occur in regions where the LIF signal is below a certain limit, because the LIF is dominated by shot noise. For this reason the velocity data given in the following are suppressed in regions where the LIF signal was less than 25% (corresponding to about 5% shot noise) of the maximum level in the present images. Figure 4.12 shows the temporally averaged relative velocity field of the droplets with regard to the gas phase, which was determined by subtracting the GIV data in Fig. 4.5 a) from the PIV data in Fig. 4.5 b). The suppression of velocity vectors results in a large gap around the vortex core. The error of the remaining relative velocity vectors can be estimated to be $< 5\%$ based on the preceding discussion. Indeed the relative velocity field in Fig. 4.12 shows the expected motion of the droplets. It can be seen that they are flung away from the vortex core in most regions. Only in the stem of the vortex bubble (right hand side) the relative velocity vectors point roughly towards the vortex core. Figure 4.5 a)/b) reveal that this is caused by the curved gas flow in the stem, whereas the droplets move straight upwards due to their inertia.

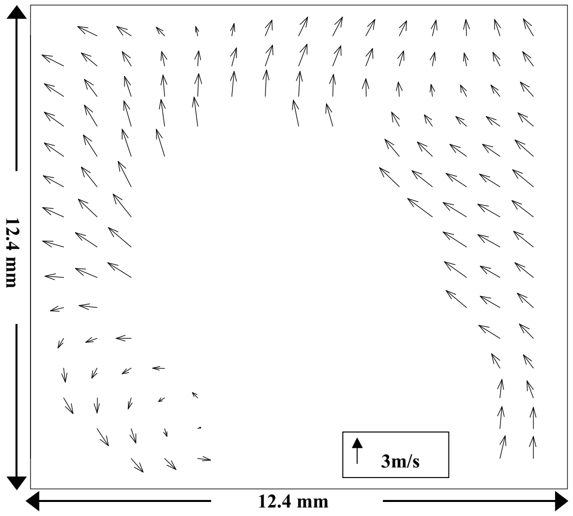

Figure 4.12: Velocity field of the droplets relative to the gas phase (temporally averaged). The data around the vortex core has been suppressed due to lacking LIF signal.

4.4 Summary and Conclusions

It is demonstrated that gaseous and liquid phase velocity fields can be measured simultaneously in unsteady, laminar flows containing water aerosol by the use of combined GIV/PIV techniques. The wavelength shift of LIF from gaseous tracers is exploited to avoid interferences between the GIV and PIV measurements. This can be applied to measure the relative velocity field and to study the interactions of both phases in two-phase flows. The measurements show that droplets and gas phase exhibit different dynamics in this experiment, as expected from theoretical considerations. Satisfactory agreement is found between the experimental and theoretical results. The measurement accuracy and precision of GIV is determined by comparing it to the PIV results in regions of the flow where particle lag is rather small. The relative error in the temporally averaged GIV measurements is found to be less than 2% there. The error in these instantaneous GIV measurements is determined to be 6-7%. The error of the relative velocity field can be estimated to be in the same range.

4.5 Further validation tests in a free jet

The group of Prof M. Long at YALE performed further measurements in a two phase flow. They used a free jet to obtain measurements of the particle velocity and the gas velocity simultaneously. Micron-size sugar particles and aceton served as the tracers for PIV and GIV respectively. Calculations on the data were performed in our group. The results from the calculation with the OFA will be given. This shall serve as an additional support of the capabilities of the algorithm. 50 measurements of simultaneously recorded double-frame images of the particle Mie scattering and acetone-LIF were processed. In Fig. 4.13 two typical single images of the two phases are shown. As can be seen the tracer distributions in both images are strongly correlated. This allows to carry out the validation on the whole seeded regions for each set of related data. Thus sufficient averaging can be obtained with 50 measurements only.

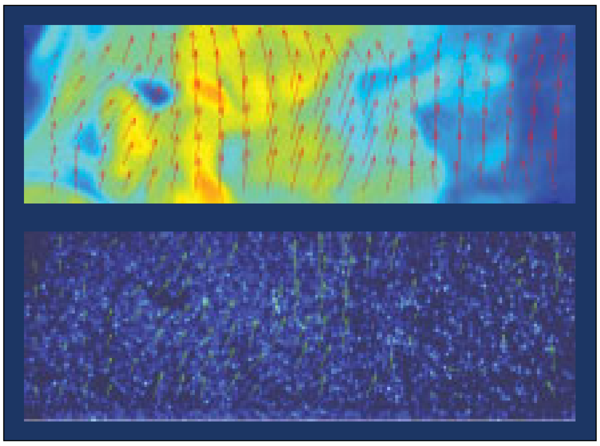

Figure 4.13: Single shot raw images from the gaseous and dispersed phase in the free jet. Typical results obtained with the OFA and a typical PIV algorithm are also shown in the foreground. Spurious vectors after PIV data processing have already been removed.

The resulting mean velocity fields obtained from 50 measurements via the OFA or a PIV algorithm respectively are shown in Fig. 4.14 and 4.15. The uniform upwards motion of the gas phase in the free jet can be clearly seen. Towards the edge of the images a slight decrease of the velocities can be found which indicates the geometrical horizontal extension of the jet. The highest velocities correspond to about 20 Pixels/Frame as indicated in the figures.

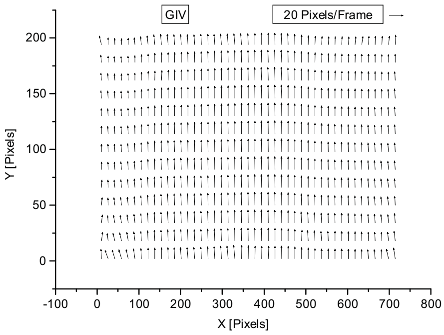

Figure 4.14: Mean velocities obtained via the OFA from 50 measurements of acetone LIF.

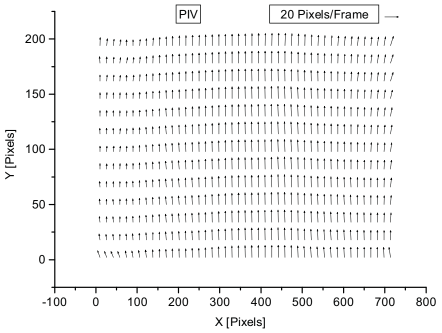

Figure 4.15: Corresponding averaged PIV data.

Some deviations of the velocity fields can already be seen in these figures. Especially in the edges higher deviations occur. A comparison based on the euclidean measure according to equation 4.3 was performed. The results are expressed relatively to the corresponding local velocity magnitude and are depicted in Fig. 4.16

$$d_{eucl} = \sqrt{(v_x^{PIV} - v_x^{GIV})^2 + (v_y^{PIV} - v_y^{GIV})^2} \tag{4.3}$$

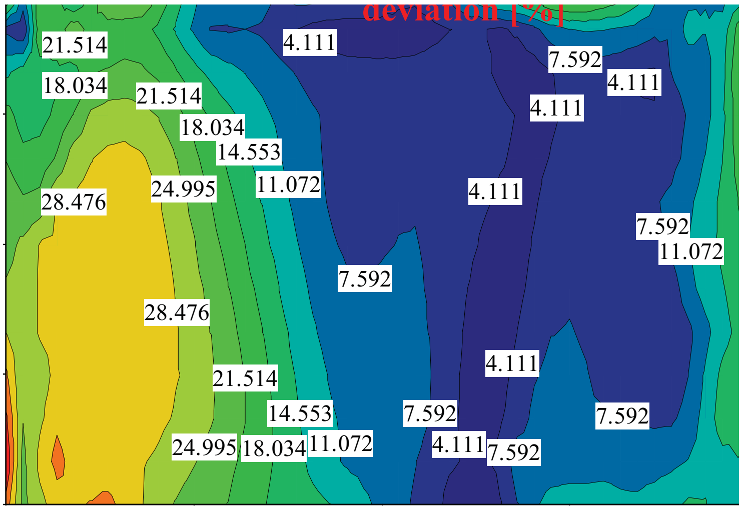

Figure 4.16: Deviation of the mean velocities depicted in Figs. 4.14 and 4.15. The euclidean distance as a percentage of the vector length is given. The distance measure is given in equation 4.3

Very small deviations of only some percent can be seen in the center of the jet which is slightly shifted to the right whereas the errors become big towards the edge of the AOI, especially on the left hand side. Errors up to 30% can found in this region of the image. The erroneous region on the right hand side is narrower but nevertheless significant. Errors up to ≈15% occur. The reason for this turned out to be the existence of larger spatial structures of the gaseous tracer in these domains of the images. This observation is based on a FFT analysis of the scalar images. In the case of PIV this does not affect the measurements because the seeding density is still high enough. In the case of the scalar images this naturally leads to a loss in spatial resolution and therefore to a higher error in the velocity determination as discussed above. Focussing on the center region of the jet a good agreement of the data sets is found. The average deviation in this region turns out to be $\approx$ 8% which is comparable to the results given above.

Chapter 5

GIV in Laminar, Unsteady Flames

5.1 Introduction

The recently developed gaseous image velocimetry (GIV) technique is applied to laminar, unsteady flames for the first time. It was briefly demonstrated in [40] that GIV can in principle be applied to turbulent flames. GIV has been validated for the first time by comparing it to PIV in a laminar, unsteady, *non-reacting* two-phase flow (see chapter 4). It is now necessary to investigate the capabilities and the accuracy of this method in more detail in flames under well controlled conditions. This is done by applying GIV to laminar, unsteady hydrogen diffusion flames. In [40] it is shown that GIV can be combined with simultaneous Raman scattering, Rayleigh scattering, and additional LIF measurements. This can be employed for simultaneous spatially-resolved measurements of majority species densities, temperature, and minority species. In particular density-velocity correlations could be measured by combining GIV and Rayleigh scattering. Such correlations were measured previously by combination of LDV with Mie scattering or LDV with Rayleigh scattering, respectively, as reviewed by Ferrao and Heitor [68]. The limitations of these techniques based on particles are well known. For example, high concentrations of seed particles may disturb the flow field and/or chemistry. The particles may also lag behind the fluid flow, and in addition sharp temperature gradients may cause large errors (up to 25% in [69]) due to thermophoresis. In contrast, GIV works without seed particles, so that Rayleigh scattering is not obscured by Mie scattering, and consequently GIV and Rayleigh measurements can be performed without any delay. It should also be noted that GIV yields instantaneous velocity fields in contrast to pointwise LDV. The first planar density-velocity correlation measurements presented recently were based on double pulse Rayleigh scattering [43]. However, the velocity fields measured in this way may generally be affected by changes in the 2D Rayleigh scattering due to chemical reactions or other factors that change the signal intensities between the two laser pulses. In contrast, GIV is based on specific molecular tracers which are sufficiently stable in combustion, such as NO (or even OH), so that changes in the 2D distribution of these tracers can be clearly attributed to fluid motion. Changes in the LIF signal due to temperature gradients can be suppressed by the proper choice of the LIF excitation line and by short delay between the two pulses [40], [70]. The data reduction scheme is discussed in detail in the chapters 2 ,3 and 4. It should be emphasized that this is a modern optical flow algorithm, which is not only based on cross-correlation analysis as most previous studies [43]. This yields much higher spatial resolution than cross-correlation analysis as demonstrated below. A number of related velocimetry techniques based on molecular tracers are discussed in the chapters 3 and 4.

5.2 Experimental

The set-up is shown in Figure 5.1. A laminar, unsteady, axisymmetric diffusion flame is generated by modulating the fuel (hydrogen) stream discharged from a round orifice (inner diameter 6mm) by using a loudspeaker. This approach is similar to the work presented by Lewis et al. [71]. As a first approach the tracer gas (NO) is seeded into the tube of the vortex ring generator using a pulsed valve as shown in Fig. 5.1. GIV depends on spatial gradients in the tracer gas distribution. Gaseous tracers are susceptible to molecular diffusion so that it is necessary to generate inhomogeneous tracer distributions a short time before they are probed.

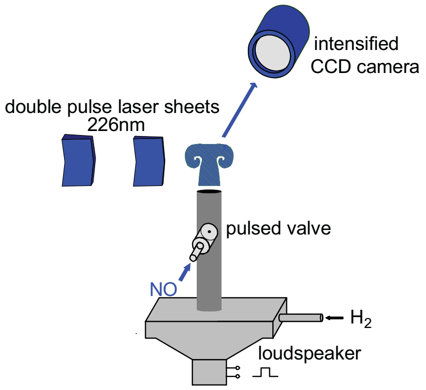

Figure 5.1: Experimental set-up for the generation of a laminar, unsteady vortical flow field by the modulation of a laminar fuel stream.

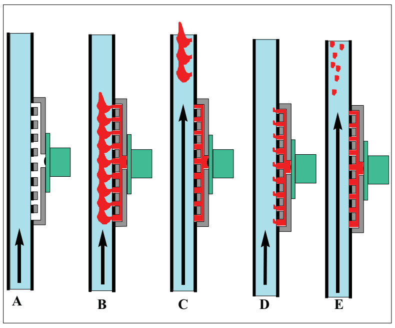

Figure 5.2: Seeding method for the generation of small gaseous structures used as flow markers.

It is also desirable not to disturb the flow by the seeding process. This is achieved in the present set-up by a special seeding method outlined in the time sequence in Figure 5.2: There is a small prechamber attached to the vortex ring generator through a number of holes (the loudspeaker is located underneath the tube shown in Fig. 5.2). First a small amount of pure NO is discharged into the prechamber (labelled "B"). Then the speaker is triggered once to clear the tube ("C"). After that small portions of the remaining NO in the prechamber diffuse into the tube generating an NO pattern in the hydrogen stream ("D"). Then the speaker is triggered a second time ("E") and the measurements are performed in this second vortex bubble. This seeding method yields inhomogeneous NO distributions in the resulting flow field, which are exploited for GIV data evaluation. The GIV measurement system contains two tunable KrF excimer lasers and an intensified progressive scan CCD camera. The excimer lasers generate two consecutive laser pulses at 248nm. The radiation is shifted to 226nm by stimulated Raman scattering in order to excite NO via the $\gamma(0,0)$ band system. The measurement system is capable of recording two images with a delay down to $\approx 1\mu s$.

5.3 Results and Discussion

Figure 5.3 depicts a velocity field (8 x 10 mm^2) that was measured 1.3 ms after triggering the speaker. A constant velocity of 44 m/s (upwards) has been subtracted from all vectors in order to visualize the rotational motion: The toroidal vortex core can be clearly identified. The magnitude of the velocity vectors in the center of the image equals $\approx$ 16 m/s. The reaction zone, as determined from OH imaging (not shown), is located close to the outer edge of the velocity vectors shown in Fig. 5.3. A pair of corresponding LIF raw data images are shown underneath the vector plot.

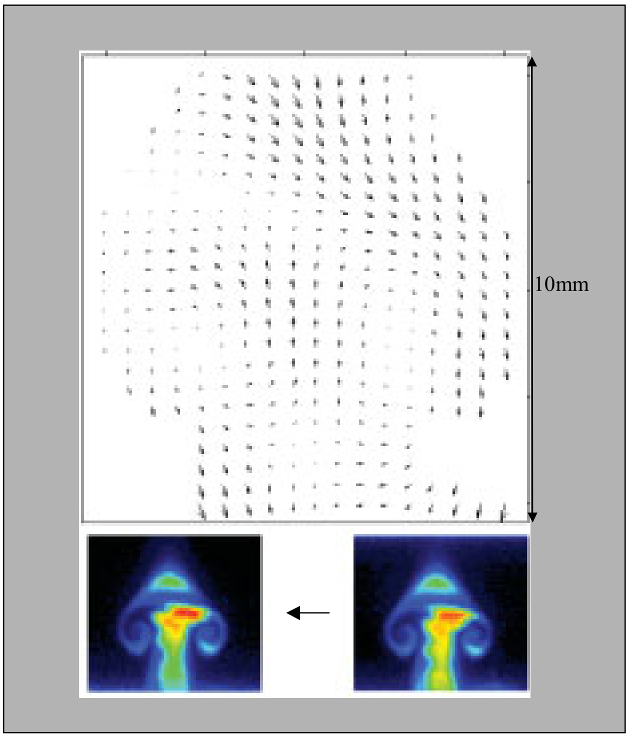

Figure 5.3: Velocity field and raw LIF (NO) images. The velocity field is determined via the OFA.

It can be seen that the NO distribution does not simply reflect the fluid discharged from the orifice, but there are modulations in the NO signal. They are caused by the seeding method described above. The GIV data evaluation depends on these gradients. It is clear that the sharpness of the gradients strongly affects the spatial resolution of the method. Stronger gradients than in the raw images in Figure 5.3 can be achieved by "tuning" the seeding process (unfortunately "holes" in the NO distribution tend to occur under this condition). A resulting single shot LIF image (9 x 10 mm^2) is shown as an example on the right hand side in Figure 5.4.

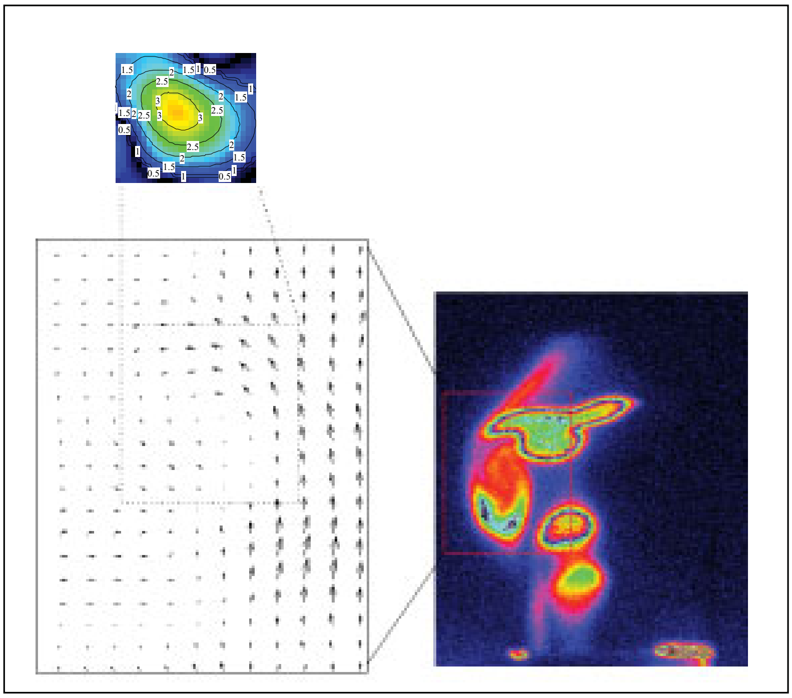

Figure 5.4: High resolution velocity and vorticity field

It can be seen that there is a sequence of NO "blobs" within the left "branch" of the vortex bubble, which is wrapped up and down into the vortex core. The resulting instantaneous velocity field shown in Fig. 5.4 has a spatial resolution of 0.3 mm corresponding to the spacing of the vectors. It should be emphasized that this spatial resolution could not have been achieved by simple cross-correlation analysis, because the spatial resolution is much smaller than the typical length scale of the NO structures. The left side of the vortex core can be clearly seen in Fig. 5.4. The vorticity (z component), defined as $(rot\vec{v})_z = \frac{\partial v_z}{\partial y} - \frac{\partial v_y}{\partial z}$, of the vortex core is shown in the upper frame in Fig. 5.4. This demonstrates that GIV yields instantaneous continuous field velocity data in such flames with a spatial resolution of 0.3 mm in the present state. The precision of the single shot GIV data can be estimated, as a first approach, from the variability of a set of instantaneous velocity fields obtained under repeatable conditions. The standard deviation of the present instantaneous data equals $\approx 10\%$. This variability includes shot-to-shot fluctuations in the flow field, which can be estimated from the fluctuations in the LIF raw data to be $\approx 7\%$. Thus, the precision of the instantaneous GIV data is roughly $\approx 7\%$.

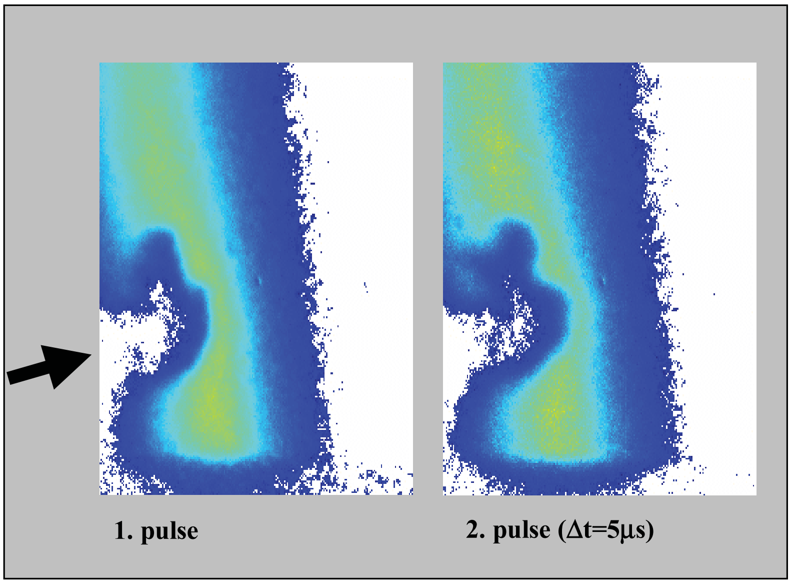

Figure 5.5: OH double pulse raw images

The OH radical can also be used as the flow tracer under certain conditions as proposed previously [72]. OH is very attractive because velocity profiles could be measured close to the reaction zone without any seed materials. It is generally desirable to acquire two OH images with a delay that is short compared to the chemical reactions, so that changes in the OH distribution are solely caused by fluid motion. OH is formed via fast two-body reactions within $\approx 15\mu s$ and recombines via slow three-body reaction within $\approx$

3 ms, respectively, in hydrogen-air diffusion flames [70]. This implies that the change in the measured OH distribution due to chemical reactions will be very small if the delay of the two measurements is much smaller than 15 μs. It is demonstrated in the following that the application of the GIV algorithm to double pulse OH images yields velocity profiles with high spatial resolution for the first time. A second set-up is used for this purpose: A laminar hydrogen-air diffusion flame is used similar to the set-up discussed above, but the flame is disturbed by a pulsed air jet that is directed towards the reaction zone from the air side. Figure 5.5 shows a pair of double pulse OH images measured with a delay of 5 μs. The air jet is indicated by the large arrow. It can be seen that the jet penetrates the reaction zone under right angle. The velocity field depicted in Figure 5.6 was calculated from the OH images in Fig. 5.5 within the rectangle shown in the left frame. The magnitude of the largest vectors correspond to ≈ 10 m/s. It should be noted that the spatial resolution of this instantaneous velocity field equals 0.4mm as indicated by the spacing of the velocity vectors in Fig. 5.6.

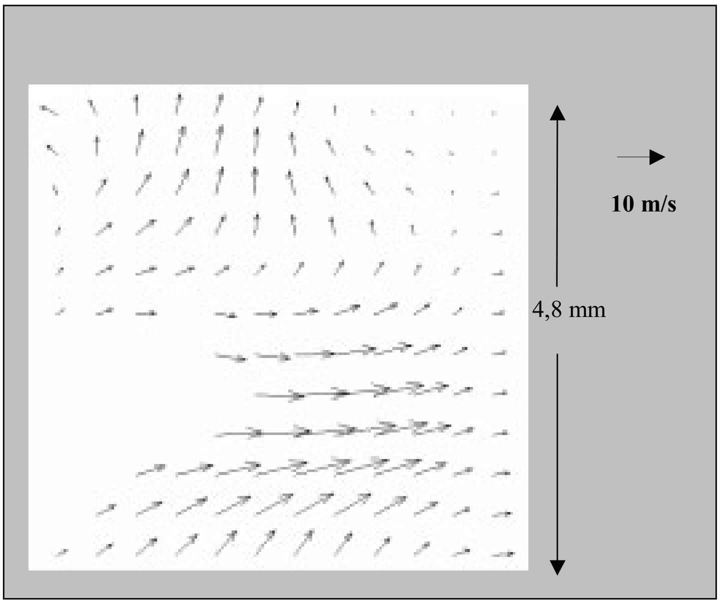

Figure 5.6: Velocity field from the OH images in Fig. 5.5

5.4 Conclusions

It is demonstrated that precise instantaneous velocity field measurements can be performed in laminar, unsteady hydrogen-air diffusion flames based on NO or OH radicals. The spatial resolution of the instantaneous velocity fields is determined to be 0.3 mm (NO) or 0.4mm (OH), respectively, in the present state. The precision of the instantaneous velocity fields based on NO is determined to be $\approx 7\%$ (relative error). This will be used for density-velocity correlation measurements in combustion because it is possible to combine GIV with Raman and Rayleigh scattering.

Chapter 6

3D flow fields: Random vs. Regular

The measurements presented so far were always based on random structures, generated by adding tracer molecules to the system under investigation. The mixing process of the added tracer itself was used to generate an inhomogeneous distribution of the tracer in the probe volume, which can be analysed by means of the OFA. A lot of advantages exist, especially in systems that are difficult to access by the measurement system, e.g. pressure chambers, technical sprays, engines. The feasibility of this measurement technique under such conditions has already been demonstrated (previous chapters). Methods to track down errors caused by *small* velocity components perpendicular to the imaging plane have been proposed.

Regular artificially created ("written") structures (e.g. grids) have several advantages in 3D flow systems with *strong* out-of-plane components especially if a stereoscopically measured 3D velocity information in the image plane is desired. Note that for this purpose the determination of two *complete* velocity projections is required. This often fails when the data contains randomly created structures and their complete 3D distribution is not known. Ambiguities can occur. E.g. optical flow, from which an apparent velocity follows, can be present although there is actually no fluid motion in the directions spanning the image plane. In a similar way no optical flow can occur despite the existence of velocity components inside the image plane. Practically in 3D systems both cases often sum up to a non-interpretable mixture. Vector validation routines will reject a considerable fraction of the apparent vectors in regions where a too strong out-of-plane motion of the tracer leads to a partial destruction of the correlation. The two projections will therefore have only a small overlap of information, which strongly reduces the data rate.

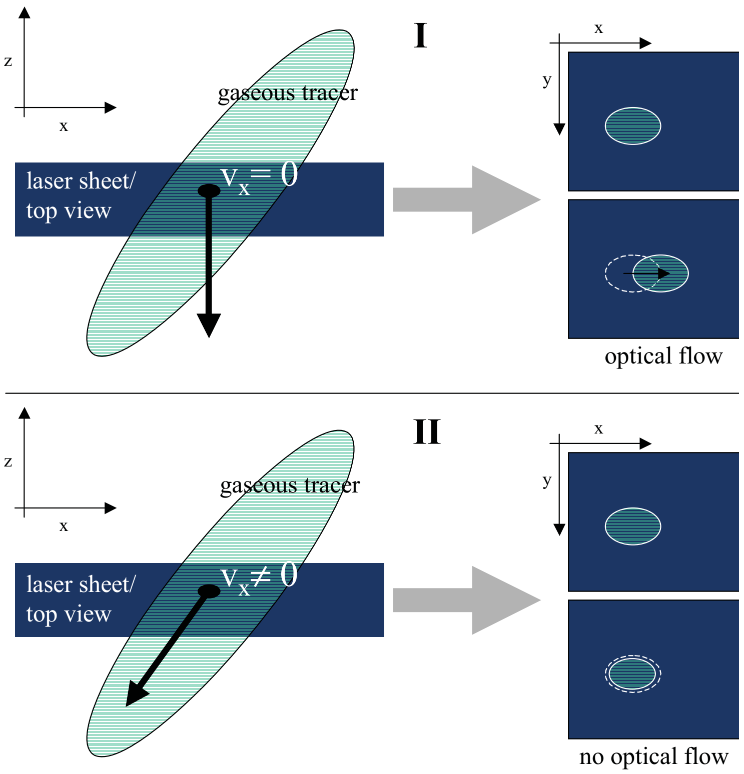

Figure 6.1: Possible worst cases that can occur locally. Fluid motion in the image plane is feigned (I) or hidden (II).

To quantify the limits of a measurement technique based on random structures, a simulation based on a 3D data set was performed. The upper part of the left hand side of Fig. 6.2 shows typical tested 3D double frames containing random distributions. A cloud-like object, the iso-surface of a 3D tracer distribution, can be seen there. The image plane is in the x-y direction. The illuminating laser sheet is indicated in terms of two planes above and below the cloud. A homogeneous illumination , i.e. no absorption of the incident light, and the absence of trapping, i.e. no absorption of the emitted light by the medium, is assumed. Stereoscopic projections onto 2 virtual detector planes were calculated. Various stereoscopical set-ups are known. The so-called "translational method" used for this simulation is described in [89]. Typical resulting projections are shown on the right hand side of Fig. 6.2. For the case of random structures shown in the upper part of the figure, 100 random test "clouds" were created and stereoscopic measurements including the data reduction were simulated. The regular structures (grid) in the lower part of the figure were treated identically.

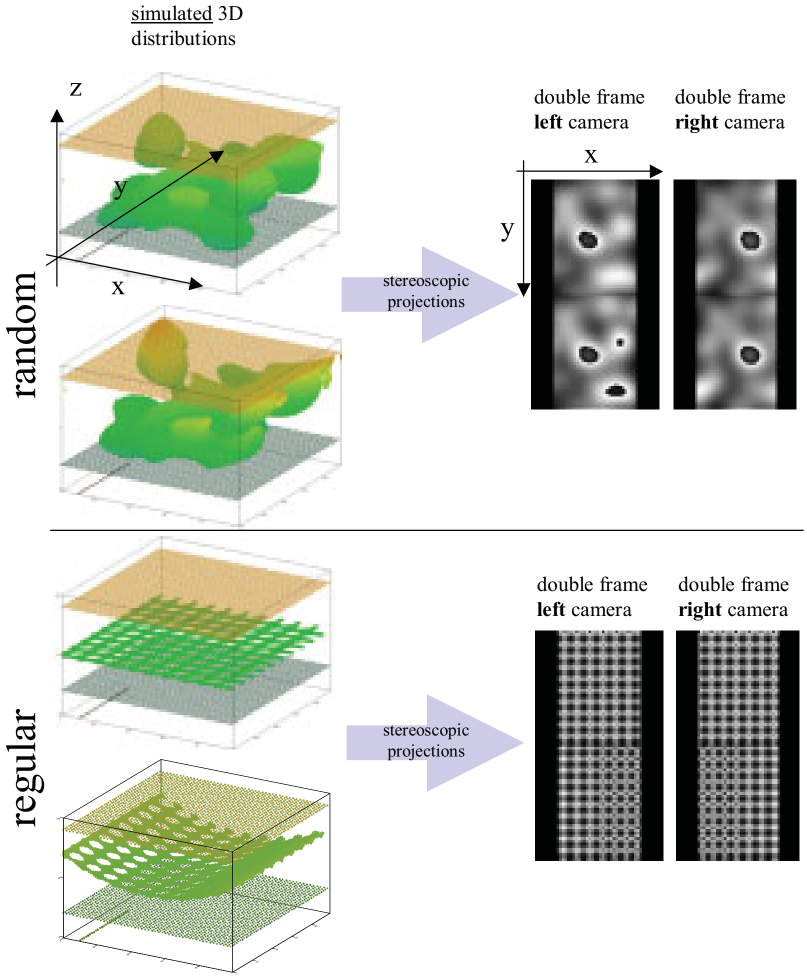

Figure 6.2: Simulated 3D structures: Random structures are compared to regular written structures

Only cases without loss of structures because of movements of parts of the clouds out of the illumination volume were considered. The quantity K was introduced as basic error criteria.

$$K = \left| \frac{v_j(x)|_{x_i} - v_j(x)|_{x_i + d \cdot \tan\alpha}}{v_j(x)} \right| \tag{6.1}$$

x_i represents any of the 2 spatial coordinates of the image plane, $v_j(x)$ is a velocity component of the 3 dimensional vector at point x, α is half the stereoscopic angle, which is the angle between the 2 imaging directions, and d is the thickness of the laser sheet. K $=$ 0.2 means that v_i varies by 20% from point x to point $x + d \cdot \tan(\alpha)$ in the image plane.

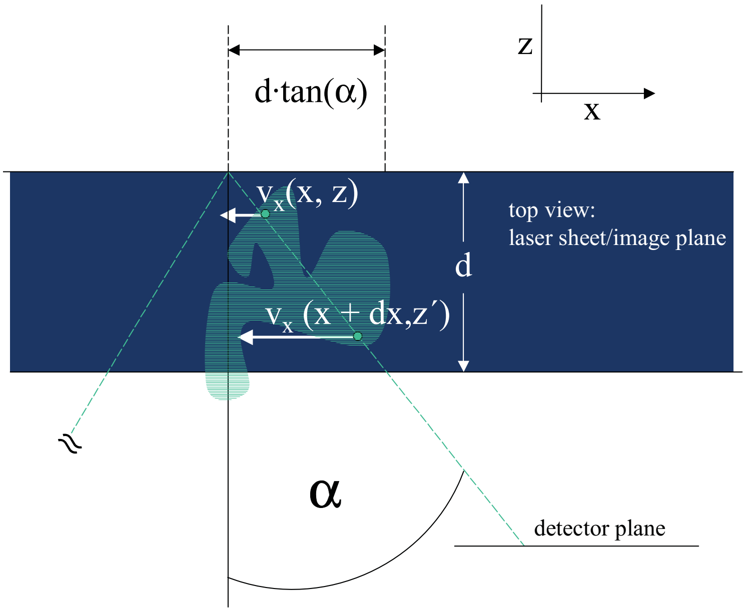

Figure 6.3: Sketch for the explanation of the introduced quantity K which measures the variation of v over a critical distance $d \cdot \tan(\alpha)$

Fig. 6.3 illustrates that K could be understood as a measure of the degree of rearrangement of partial clouds in each stereoscopic projection. Thus K also measures the loss of correlation in the projection planes, which is the fundamental inevitable source of error. By the investigation of this error criteria a quantitative estimate for the best possible accuracy can be determined.

Upon closer consideration of Fig. 6.2 the effect of local loss of correlation can already be seen although the gradient of the applied velocity field seems to be quite moderate. The structure of the velocity field is clearly visible from the distortion of the grid in the lower part of Fig. 6.2. A parabolic structure can be seen. Quantitatively it turns out that already K = 0.1 results in an average maximum error of 50% for the velocity determination of each stereoscopic channel. Note that K grows with d. In a realistic 3D application it is very important to consider the additional error occurring due to the fact that a certain percentage of the tracer volume is not probed twice as primarily excluded above. To minimize the influence of this additional source of error, d must be chosen big enough. Unfortunately this enlarges the minimum spatial scales of the velocity field allowed as $K \leq limit$ has to be met at the same time. This strongly reduces the feasibility of the technique if it is based on random structures. In the case of regular written structures however, $d \cdot \tan(\alpha)$ can be strongly reduced as will be demonstrated below. Thus even 3D flow systems with small turbulence scales and high velocity magnitudes at the same time become accessible. Because of the regularity of the tagged structures ambiguities completely vanish. 3D velocity information in a plane can be determined with high precision as will be demonstrated in chapter 7. Reliable 2D projections can be determined if only a 2 dimensional information is desired. Experiments based on regular laser written structures will be presented in the following chapters.

Chapter 7

Stereoscopic Flow Tagging Velocimetry

A laser-based method for measuring the three components of the velocity in a plane simultaneously and instantaneously without seed particles is presented. This is achieved by combining a laser flow tagging technique with stereoscopic detection, in which the tagged flow is viewed from two different directions. A single CCD camera is employed for this purpose by using a new optical detection system. The flow tagging is performed by two consecutive laser pulses, i.e., "write" and "read" laser pulses. The write laser creates a grid of tracer molecules (NO) by inducing a photodissociation process. The three-dimensional motion of the tracer molecules is measured by a thick read laser sheet.

7.1 Introduction

It is desirable to measure the three components of the velocity with spatial resolution in three- dimensional (3D) laminar and turbulent flows. This can be performed, for example, by stereoscopic particle image velocimetry (PIV), which is a well established technique [31]. However, it is well known that the tracer particles, which are generally required for PIV, may cause several problems, such as particle lag, disturbance of the flow field etc. This is a major reason for the development of particle-free flow tagging techniques, in which molecular tracers are used. Several flow tagging methods based on 1D tag lines or 2D grids are described in the literature [32],[6],[7],[33], [8],[34]. It is demonstrated in this chapter that 2D flow tagging can be combined with stereoscopic detection in order to measure the three velocity components of the instantaneous velocity field in a plane. Very few other three-dimensional velocimetry techniques that do not require tracer particles are known [35], [36].

7.2 Experimental

Fig. 7.1 shows how the present technique works. A well defined tracer molecule distribution is generated by a write laser grid via a photodissociation step, i.e., the tracer molecules are photofragments. Other photochemical processes may be used as well. It is required that there are parent molecules present throughout the entire probe volume, but their distribution is not necessarily homogeneous.

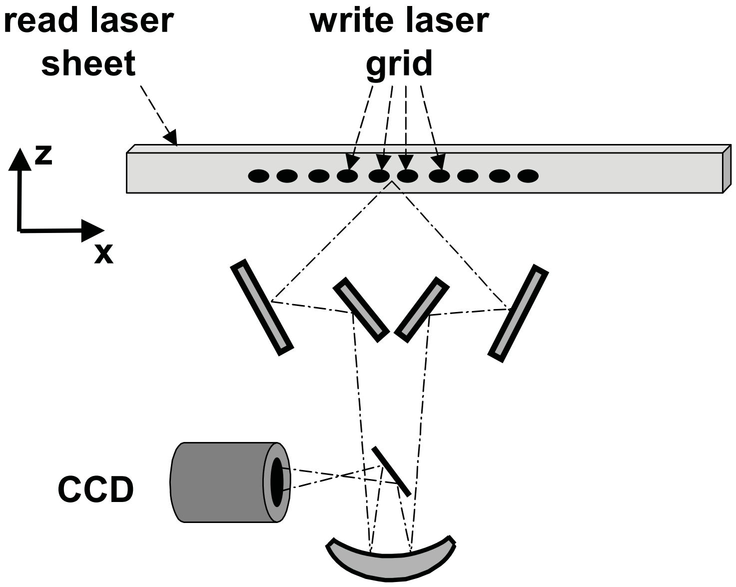

Figure 7.1: Top view of the experimental set-up. Stereoscopic detection is performed by a mirror system and a single CCD camera. However, two independent cameras could be used as well for stereoscopic flow tagging velocimetry.

Each write laser beam, i.e. each line of the grid, is tightly focussed, so that a high spatial resolution is finally achieved (see below). The tracer molecules are convected with the three-dimensional flow. The read laser is fired after a certain delay Δt in order to probe the tracer molecules using laser-induced fluorescence (LIF). The read laser beam is formed to a thick sheet, similar to stereoscopic PIV, so that all the tracer molecules reside within the probe volume after being convected by the flow. The 3D distribution of the fluorescing molecules is recorded instantaneously by the stereoscopic detection system. The latter is realised by the mirror system and the CCD camera shown in Fig. 7.1. This system contains two optical detection channels, which are used for stereoscopic detection (see below). It is noteworthy that two independent cameras could be used as well. Each detection channel yields a 2D velocity field, provided that suitable data reduction software is applied to the measured images (see chapter 2). The three velocity components in the plane of the write laser grid are calculated from these two velocity fields [31]. It should be noted that the spatial resolution Δz in the z - ("out-of-plane") - direction of the technique proposed in this paper is in principle higher compared to stereoscopic PIV. Δz is essentially limited by the extension of the write laser grid in the z direction (provided that the resolution of the recording system is smaller than that), because the initial tracer molecule distribution basically depends on the extension of the write laser. Thus, small Δz values can be achieved by focussing the write laser beams. In contrast, Δz is essentially limited by the depth D of the laser sheets in stereoscopic PIV experiments, because all the particles within the thick laser sheets contribute to the measurement [31]. D can not be reduced beyond a certain level, because it is generally required that most of the illuminated seed particles reside in the light sheets for both light pulses. Otherwise large errors will occur in the PIV data, because it is no longer possible to determine the displacement of the particles accurately by typical data reduction schemes, e.g., cross-correlation analysis (ref. simulation in chapter 6). The present experiment is performed in the gas-phase under standard (room air) conditions. Tert-butyl nitrite, $(CH_3)_3CONO$, is used as the parent molecule in the present experiment. It can be dissociated with a cross-section of $\approx 2 \cdot 10^{-18}\text{cm}^2$ at 193 nm (extrapolated from the data available beyond 200 nm), forming $(CH_3)_3CO$ and NO

[30], [37]. A broadband ArF excimer laser is used for this purpose. Two sets of write laser lines, each ≈ 0.5 mm in diameter, are created by splitting and focussing the beam of the dissociation laser, basically by using two arrays of 15 cylindrical lenses (f = 30 cm). The pulse energy of each write laser beam in the probe volume is about 1 mJ. The photodissociation threshold of tert-butyl nitrite is 14308 cm^{-1} [37] (and references therein).

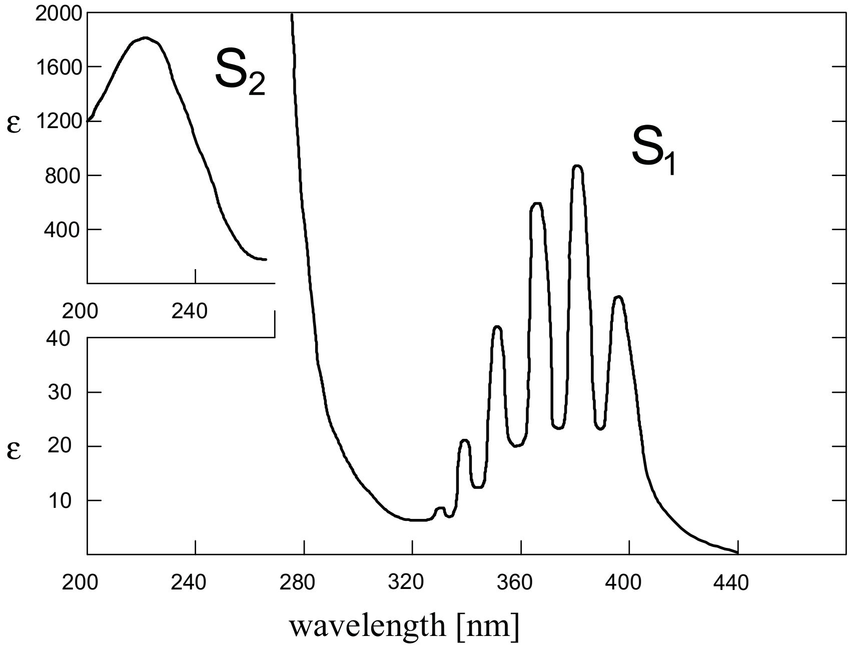

Figure 7.2: Dissociation cross-section of tert-butyl nitrite (from [30]).

Accordingly, the excess energy of the dissociation at 193 nm is ≈ 4.9 eV, which leads to significant internal and translational energy of the photofragments. However, the photofragments loose their nascent, non-thermal energy very rapidly due to molecular collisions at atmospheric pressure and room temperature [34]. Thus, it can be assumed that the excess energy does not affect the flow measurement. The photofragment probed in this experiment is NO, which is excited at about 226 nm via the R_{21} (17.5) line in the $\gamma(0,0)$ band system [38]. A tunable, narrowband KrF excimer laser is used for excitation, the laser radiation of which is shifted to ≈ 226 nm (≈ 7 mJ/pulse) using stimulated Raman scattering in hydrogen. The resulting $\gamma(0,3)$, $\gamma(0,4)$, and

γ(0,5) LIF emission lines between 250 nm and 300 nm are recorded by the camera system, which is equipped with a butylacetate filter to suppress stray light. The profile of the thick read laser sheet is 24 mm x 6 mm. Recently the photodissociation of NO_2 at 308 nm, generated by a XeCl laser, has been proposed as a source of NO molecules for flow tagging [34]. However, the cross-section of NO_2 at 308 nm is $1.7 \cdot 10^{-19}$cm^2, whereas the cross-section of tert-butyl nitrite is a factor of $\approx$ 10 larger at 193 nm (see above). Thus, much less laser energy is needed for generating suitable tag lines that contain sufficiently high tracer molecule densities. Consequently, a large number of tag lines can be created with a single commercial ArF excimer laser using tert-butyl nitrite, whereas a single tag line was used in previous work based on NO_2 [34]. Thus, the larger dissociation cross-section of tert-butyl nitrite allows one to measure instantaneous 2-D velocity fields without extensive effort as will demonstrated. The pulse energy of commercial ArF lasers is generally somewhat lower than that of XeCl lasers. It is noteworthy that tert-butyl nitrite can also be efficiently dissociated by 248 nm light [30] generated by KrF lasers, which yield pulse energies comparable to XeCl lasers. It is desirable to avoid the use of two independent camera systems for stereoscopic detection from the practical point of view. Thus, a mirror system was developed that allows one to perform stereoscopic recordings with a single camera as mentioned above. Such optical systems were proposed previously [31], but a new apparatus was designed, which is free of lenses in order to improve the imaging quality, in particular with regard to the depth of focus. This was necessary because the recorded LIF wavelengths in our experiment are in the ultraviolet range, where the dispersion of lenses is particularly detrimental. It can be seen in Fig. 7.1 that five flat mirrors and one spherical focussing mirror (f=35cm, d=25cm, aluminium) are used. The angle of the optical axes of the two detection channels is 90°, and they make an angle of 45° with the measurement plane. The field of view in this experiment contains about 3.2 x 4.8 cm^2. The spatial resolution of the detection system corresponds to about 100 μm in the probe volume. It turned out that an out-of-plane displacement of $\approx$ 100 μm can indeed be resolved by this set-up. An image-intensifying progressive scan CCD camera, that is capable of recording two images with a delay down to $\approx 1\mu$s, is employed. The double-frame option is used to record laser-induced emissions from both the write and the read laser pulses in each individual "single-shot" measurement. The write laser grid is visualized by chemiluminescence that arises from the photodissociation process [37]. This can be used to record the initial, instantaneous tracer gas distribution precisely, even when the parent molecule distribution or the write laser beams fluctuate from shot to shot. For example, spatial variations of the write laser beams may be caused by beam steering in dense optical media, such as dense sprays. Initial measurements are done in a laminar free jet of nitrogen, that is doped with about 1% tert-butyl nitrite. The gas stream is discharged from a nozzle (d = 3 cm), which is installed ≈ 3 centimetres underneath the probe volume. The nozzle is tilted with regard to the measurement plane ($\approx 45°$), so that the gas motion is predominantly in the y and z directions. The gas flow in the jet is so broad that the gas motion is approximately uniform throughout the probe volume (2 x 2 cm^2). This will be used for quantification of the measurement precision.

7.3 Results

Fig. 7.3 shows two typical unprocessed images of an instantaneous velocity measurement in the homogeneous free jet. The upper frame results from the write laser pulse and exhibits the chemiluminescence mentioned above. The left hand side corresponds to the left optical channel and the right hand side to the right optical channel, respectively. The lower frame has been recorded when the read laser has been fired after a delay of $\Delta t = 3$ ms. It shows the single-shot LIF from NO (the imaged area is slightly smaller than in the upper frame because of the limited height of the probe laser sheet). The 2D displacement fields of the LIF grids in the lower frame with regard to the chemiluminescence grids in the upper frame yield the gas motion perpendicular to the left and right, respectively, optical axes after proper calibration [31].

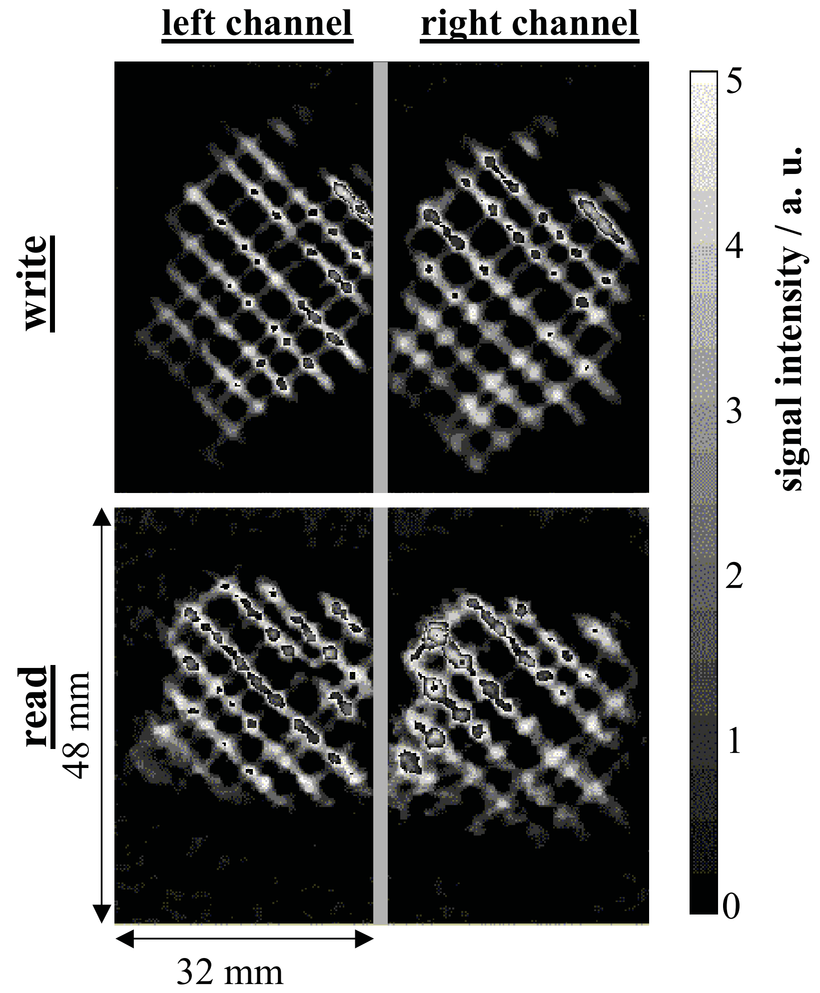

Figure 7.3: Pair of measured images that corresponds to a 3D instantaneous velocity measurement.

The displacement of both the left and right image pairs is found by employing the OFA separately to the left and right, respectively, image pairs. The resulting 2D velocity field from the left image pair is given in Fig. 7.4a) and the velocity field from the right image pair in Fig. 7.4b). The method yields continuous velocity fields, but the spatial resolution of this measurement technique is, essentially, roughly limited by the spacing of the grid line intersections. It can be seen in Fig. 7.4 that the gas velocity is approximately constant throughout the measured flow field, as expected from the set-up. All the velocity vectors are slightly tilted towards the left hand side in Fig.

7.4a), whereas they are slightly tilted towards the right hand side in Fig. 7.4b). This is expected from the orientation of the free jet and the geometry of the stereoscopic set-up.

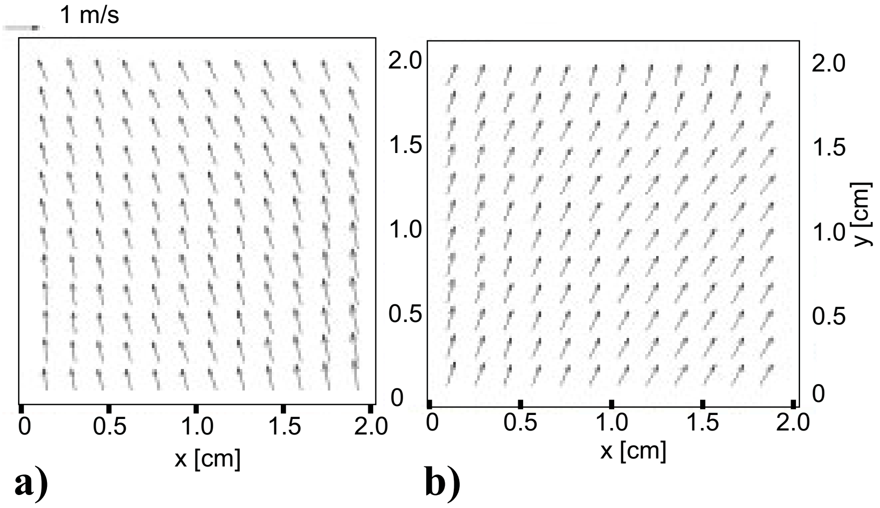

Figure 7.4: 2D velocity fields calculated from the measured images in Fig. 7.3; a) left optical channel, b) right optical channel.

Finally, the 3D velocity field, which is shown in Fig. 7.5, is calculated from the pair of 2D velocity fields in Fig. 7.4 by using well known procedures [31]. The velocity vectors represent the x and y components, and the z component is given by the grey level of the background, as indicated by the grey scale. It can be seen that the x component is approximately zero as expected (see last Section). The accuracy of these instantaneous 3D velocity fields can be estimated, in a first approach, by considering the spatial variations of the velocity vectors, since the gas flow can be assumed to be uniform. It turns out that the spatially averaged mean values and standard deviations of the instantaneous velocity components are: $v_x = (0.03 \pm 0.01) m/s, v_y = (0.6 \pm 0.05) m/s$, and $v_z = (0.5 \pm 0.1) m/s$. The y and z components are approximately equal because of the 45° angle of the free jet with regard to the imaging plane. The standard deviations of v_y and v_z correspond to 8% and 20%, respectively, relative error.

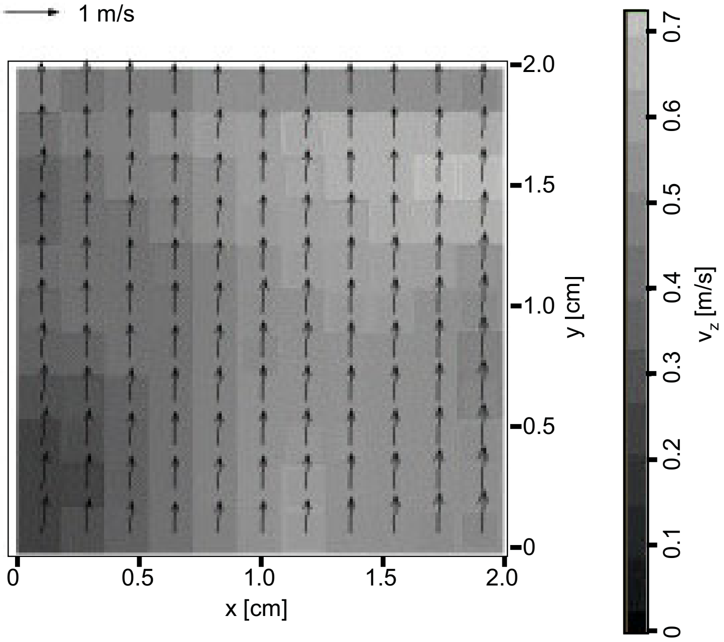

Figure 7.5: Instantaneous 3D velocity field calculated from the 2D velocity fields in Fig. 7.4.

7.4 Conclusions

It is demonstrated that the three velocity components of gaseous flows can be measured instantaneously in a plane without particle seeding by stereoscopic flow tagging velocimetry. This is particularly promising in certain three-dimensional flows in which particle-based techniques struggle to provide accurate data. For example, the wavelength shift of the LIF used for detection can be exploited to perform measurements in media with large straylight background, for example, between the droplets in sprays.

Chapter 8

Gas-Phase Velocity Field Measurements in Dense Sprays by Laser-Based Flow Tagging

It is demonstrated that gas-phase velocity measurements can be performed in dense sprays by using a new 2D laser-based flow tagging technique. Velocity measurements in dense sprays, such as automotive direct injection (DI) Otto and Diesel sprays, are difficult with conventional techniques because of the high number densities of droplets, the optical thickness of the medium, and multiple light scattering effects. The present flow tagging technique is performed by two consecutive laser pulses, i.e., "write" and "read" lasers. The write laser creates a grid of tracer molecules (NO) by inducing a photodissociation process. The tracer molecules are convected with the flow and probed by the read laser after a certain delay. The instantaneous velocity field is determined by time-of-flight analysis.

8.1 Introduction

It is well established that the velocity field of the gas phase is important for secondary break-up and evaporation of sprays [19],[20]. The theory of evaporation in dense sprays, where the average spacing of the droplets is only a few droplet diameters, is still incomplete, due to the strong interactions (heat and mass transfer) of the droplets and the gas phase [21]. In addition, the interactions of dispersed and continuous phase in non-evaporating, highly particle-laden gas flows are not fully understood [23]. This makes it difficult to model the flow field of the gas phase in dense sprays. It should be noted that dense sprays are technically important. For example, high-pressure swirl injectors, generating dense hollow-cone sprays, are currently being developed for automotive direct injection spark ignition engines [5], [3]. One reason for the lack of a satisfactory theory of dense spray evaporation is the fact that little experimental data exists of the gas flow field in such two-phase flows. The lack of experimental data is mainly caused by severe difficulties which are encountered when conventional measurement techniques are applied to highly particle-laden flows. In principle, point-wise gas velocity measurements can be performed in sprays by Phase Doppler Anemometry (PDA) based on sufficiently small particles [24]. However, PDA suffers from high number densities of droplets and beam steering, for example, in the dense regions of automotive direct injection sprays [2]. Particle Image Velocimetry (PIV) based on fluorescent particles can also be employed for gas-phase velocity measurements in sprays [25]. However, PIV is not applicable when the medium is so dense that the detected signal is strongly affected by multiple light scattering [3]. PIV requires that individual particles are resolved, and this becomes impossible when strong multiple scattering results in considerable image blurring. For these reasons a new flow tagging technique was developed, which is based on a molecular tracer. Previous flow tagging experiments are discussed elsewhere [6][26][7][8][12][27][28]. Briefly, a 2-D tracer distribution (grid) is "written" in the gas flow by a laser-induced photodissociation process. The tracer molecules are convected with the flow. The read laser is fired after a certain delay Δt, in order to probe the tracer molecules using laser-induced fluorescence (LIF). The present technique works, in principle, very similar to a 2D velocimetry technique (Gaseous Image Velocimetry, GIV), which is based on random distributions of a gaseous tracer (see chapter 3). The random distributions are generally created by an incomplete, turbulent mixing process. GIV can be applied to dilute sprays only, because it depends on the absolute LIF signal intensities, which are not reliable in dense sprays. In contrast, the technique proposed here can also be applied to dense sprays, because it does not depend on the absolute values of the LIF intensities. The present technique is also hardly affected by multiple light scattering, because the tag lines are wide enough, e.g. 0.5-1mm, so that they can still be resolved. Beam attenuation does not affect the feasibility of the technique, as long as the grid is recognized. Laser beam steering is not an important factor because the initial tracer grid is recorded as described in the following section.

8.2 Experimental

Initial measurements have been performed in a hollow-cone gasoline direct injection spray. The prototype swirl injector and electronics were supplied by S. Arndt (Robert Bosch GmbH, Stuttgart). It has been operated with 50bar rail pressure in room air. Ethanol has been used as the fuel. Unfortunately, commercial standard fuels like gasoline or Diesel can not be used in this experiment, because the ultraviolet (UV) laser light and LIF are strongly absorbed, in particular in the dense spray regions. However, it can be expected that other UV-transparent model fuels like iso-octane could be used as well. The measurements have been performed at 1ms after triggering the injector, i.e., in the fully developed spray pulse (pulse length: 1.5ms) The maximum droplet density is about $5 \cdot 10^6$ cm^{-3} in the probe volume. The Sauter mean diameter of the droplets is $d_{32} \approx 15\mu$m [29] (thus, the average droplet spacing at maximum density is $\approx 4 \cdot d_{32}$). This spray is comparable to previously investigated sprays, in which PIV measurements turned out to be difficult [3]. Flow tagging is performed here by using two consecutive laser pulses, as mentioned before. The present set-up is outlined in Fig. 8.1, but the detector is not shown. An image-intensified CCD camera is employed as the detector. A Mie scattering image from the central plane of the spray is included in Fig. 8.1 to demonstrate the field of view and the orientation of the spray. The field of view (32mm x 24mm) has been imaged onto the CCD camera by using a spherical focussing mirror (f=35cm, d=25cm, aluminium). A well defined tracer molecule distribution is generated by a "write" laser grid via photodissociation of parent molecules, which are present throughout the probe volume.

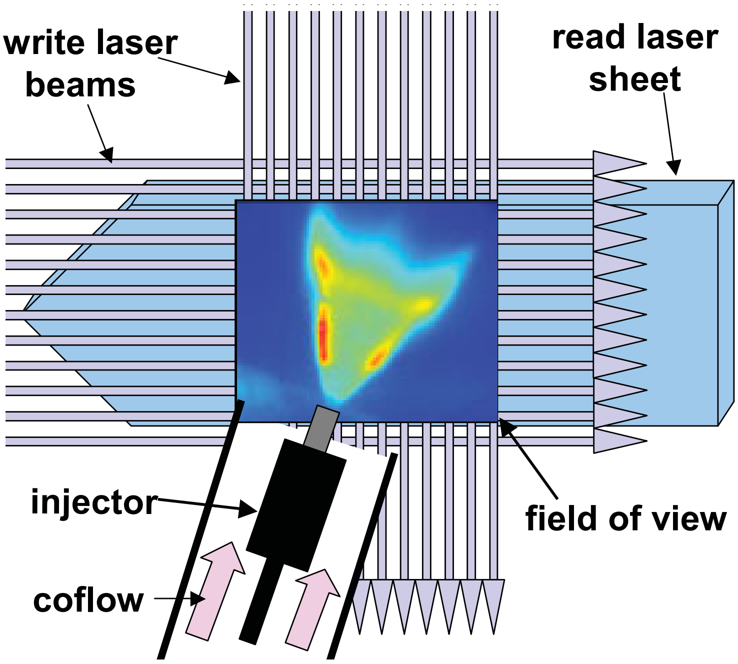

Figure 8.1: Experimental set-up. The intensified CCD camera is not shown. Instead, a Mie scattering image is included showing the spray at 1ms after triggering the injector.

The tracer molecules are convected with the flow. The "read" laser is fired after a certain delay Δt in order to probe the tracer molecules using laser-induced fluorescence (LIF). The read laser beam is formed to a thick sheet (10mm x 25mm) so that all the tracer molecules reside within the probe volume after being convected by the flow. Tert-butyl nitrite, $(CH_3)_3CONO$, is used as the parent molecule in the present experiment (see chapter 7). Seeding of gaseous tert-butyl nitrite ($\approx$1% mole fraction) is performed by a low velocity coflow of nitrogen as shown in Fig. 8.1. The tracer gas is predominantly drawn into the spray by the entrainment gas flow (see next section). The velocity of the coflow is orders of magnitude smaller than the gas velocities in the spray, so that it does not significantly disturb the gas flow within the spray. A 248-nm KrF excimer laser is used as the write laser, in contrast to previous work where a 193-nm ArF laser was employed. The photodissociation cross-section of tert-butyl nitrite is a factor of $\approx$2 smaller at 248nm compared to 193nm [30], but the pulse energy of commercial KrF lasers (Lambda Physik) is generally somewhat higher compared to ArF lasers, and in addition the absorption losses in room air are much smaller at 248nm. Two sets of write laser lines, each $\approx$ 0.5mm in diameter ($\approx$ 10mJ/pulse), are created by splitting and focussing the beam of the dissociation laser, basically by using two arrays of 15 cylindrical lenses (f = 30 cm) as shown in Fig. 8.1. The photofragment probed by the read laser is NO, which is excited at about 226nm via the $R_{21}(17.5)$ line in the $\gamma(0,0)$ band system. A second tunable, narrowband KrF excimer laser is used for this purpose. The detection of NO and discrimination against Mie scattering is described in more detail in chapter 7. It should be noted that the tagging scheme based on tert-butyl nitrite yields the possibility to record instantaneous 2-D velocity fields containing a large number of vectors, in contrast to most other tagging schemes [6][26][7][8], because a considerable number of tag lines can be created by a single commercial write laser, and NO can be probed effectively. It is also noteworthy, that the three components of the instantaneous velocity in a plane can be measured based on tert-butyl nitrite, as described in chapter 7. It was mentioned in the introduction that the initial tracer distribution must be recorded in order to correct for laser beam steering. This can be done either by probing NO using the read laser at $t \approx 0$, or by recording laser-induced emissions from the write laser grid. The latter can be performed in each individual measurement, so that spatial shot-to-shot fluctuations of the write laser grid could be detected. However, this requires that a second camera image is available to record the write laser beams on a "single-shot" basis. Actually, the "progressive scan" CCD camera used here is capable of recording two images with a delay down to $\approx 1\mu$s. We used this "double-frame" option to record laser-induced emissions from both the write and the read laser pulses in a number of individual measurements. In this case, the elastic scattering (Mie and Rayleigh) from the write laser beams was exploited to visualize the initial grid. However, such images show strong variations in the spatial distribution of the detected signal along the tag lines, basically due to spatial variations in the droplet density. This makes data evaluation more difficult. Thus, we used the second method mentioned above for visualization of the initial grid, i.e., NO detection by the read laser at t>0. This requires that there are no pulse-to-pulse fluctuations in the position of the initial grid, because the initial grid and the displaced grid can not be recorded in a single spray pulse, since the read laser can only be fired once. Indeed, we have seen beam steering of the write laser beams, but the beam steering turned out to be reproducible from pulse to pulse. The latter was investigated by evaluating LIF (NO) single-shot images at $t \approx 0$. The shot-to-shot variations in the positions of the tag lines within the spray were found to be insignificant, i.e. smaller than 10% of the tag line width. In addition, the width of temporally averaged tag lines (averaged over 10 double pulse measurements) at $t \approx 0$ with and without the spray turned out to be the same (error: <5%). Both corroborates that shot-to-shot variations in the beam steering were indeed insignificant. Thus, it is sufficient to use a temporally averaged initial grid for the flow tagging in this particular application.

8.3 Results and Discussion

Fig. 8.2 shows a pair of typical CCD images measured in the spray with a delay of Δt=40μs. Both images show LIF from NO and some residual Mie scattering. Fig. 8.2a) has been averaged over 10 measurements, and Fig. 8.2b) results from a single measurement as described before.

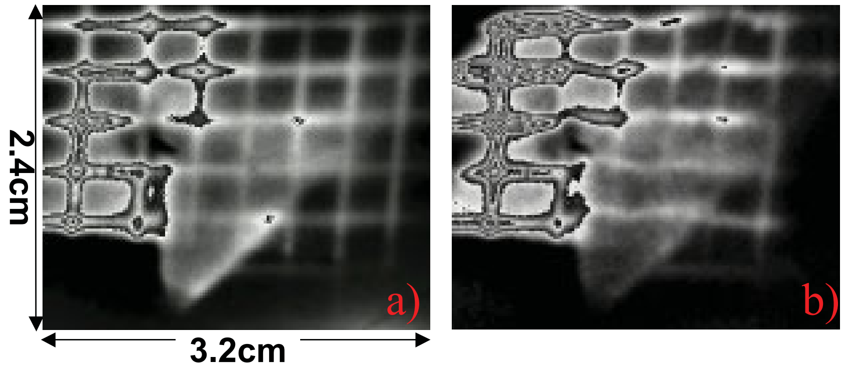

Figure 8.2: Pair of LIF (NO) images measured in the spray with a delay of Δt=40μs. (a) Measurement at t=0 averaged over 10 double pulses. (b) Instantaneous measurement at t=40μs.

It can be seen that there are considerable spatial variations of the NO signal on the grid, basically because of beam attenuation in the dense spray, but the grid is still recognized in Fig. 8.2b). The displacement field of the distorted grid in Fig. 8.2b) with regard to the initial grid in Fig. 8.2a) yields the instantaneous gas velocity field. The displacement is found by employing the OFA. The resulting instantaneous velocity field is given in Fig. 8.4a). The method yields continuous velocity fields.

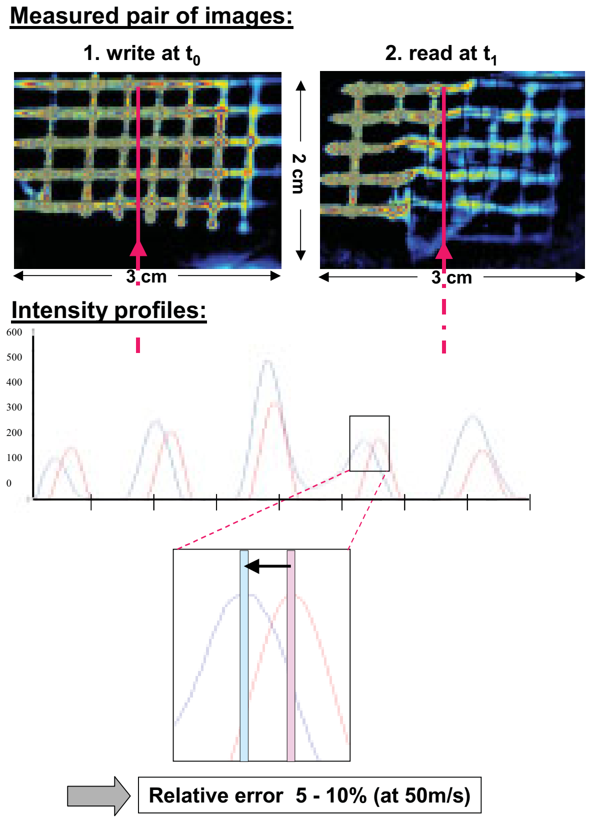

Figure 8.3: The ultimate accuracy of the velocity information physically contained in the double frames is given by the accuracy with which the position of one tag line can be determined.

However, the spatial resolution of this measurement technique is, essentially, roughly limited by the spacing of the grid line intersections. The accuracy of the instantaneous measurements is basically limited by the displacement of the tag lines, $\Delta x = v \cdot \Delta t$, the width of the tag lines (full width at half maximum), w, and the uncertainty to determine the center of the displaced tag lines, $\sigma(\Delta x)$. The latter can be estimated to be 10% of w [26]. In these initial measurements w equals 1mm. Thus, the accuracy of a typical velocity measurement with v=50m/s and $\Delta t = 40\mu$s can be estimated, in a first approximation, as $\sigma(v)/v > \sigma(\Delta x/)\Delta x > 0.1w/\Delta x = 100\mu$m/2mm = 5%. Accordingly, smaller velocities exhibit larger errors. Molecular diffusion does not significantly affect the accuracy in this application because of the short delay Δt=40μs. A Mie scattering image, similar to the one given in Fig. 8.1, is shown in the background of Fig. 8.4a) to indicate the spray contour. It can be seen that there are large eddies (up to ≈ 60m/s) formed at the edge of the spray cone, and strong air entrainment is observed closer to the nozzle. Obviously, these eddies deform the shape of the spray cone, although the droplets travel at high velocity (of the order of 50m/s [29]). This can be explained by the small size of the droplets, since d_{32} ≈15μm as mentioned above. A mean velocity field, that has been averaged over 10 instantaneous measurements, is given in Fig. 8.4b). It can be seen that it is qualitatively very similar to the instantaneous measurement in Fig. 8.4a) (thus, a number of 10 instantaneous measurements is sufficient to determine the mean velocity field at least within the spray). One might think that the high-pressure spray generates a highly turbulent flow field of the gas phase. However, this is not necessarily true, since small particles tend to reduce the turbulent intensity [23]: Small particles follow the gas flow, and thereby turbulent energy is transformed into kinetic energy of the particles.

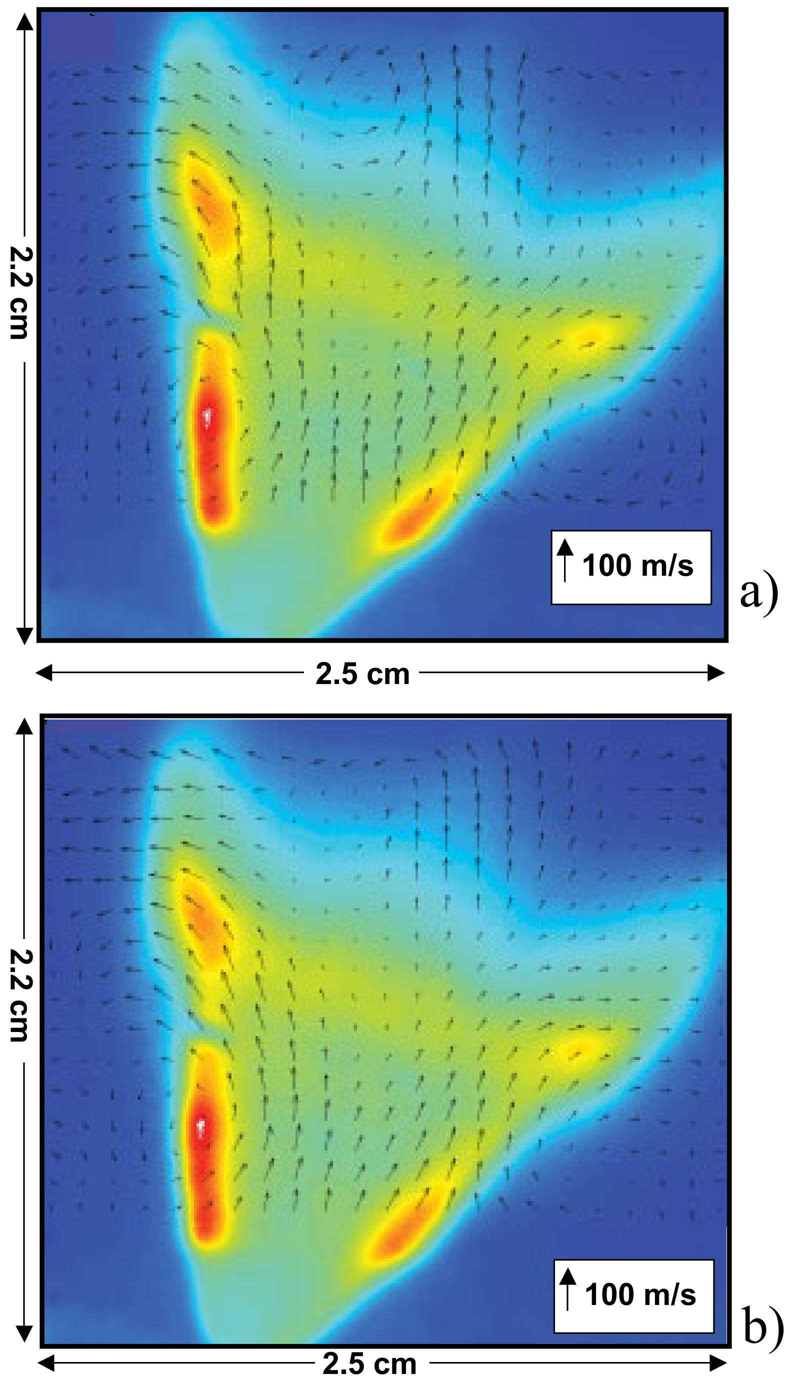

Figure 8.4: Velocity fields measured in the spray. A Mie scattering image is given in the background to show the distribution of the liquid phase. (a) Instantaneous velocity field. (b) Mean velocity field averaged over 10 instantaneous measurements.

This is indeed seen in the data: The relative standard deviation of the velocity magnitudes of the 10 instantaneous measurements is given in Fig. 8.5. The spray cone is outlined by dotted lines. Obviously, the pulse-to-pulse fluctuations of the gas flow are small (20-30%) in most regions of the spray cone, where the droplet density is high. The fluctuations are much larger inside the hollow-cone and in the ambient air. In conclusion, the spray tends to generate high turbulence only in regions where the droplet density is relatively low.

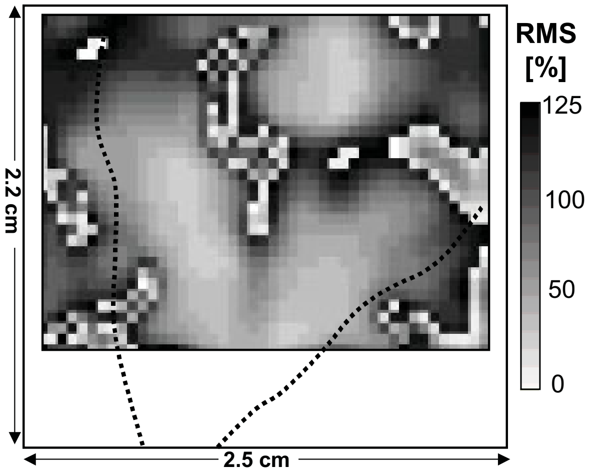

Figure 8.5: Relative standard deviation of 10 instantaneous measurements corresponding to the data given in Fig. 8.4. The edge of the spray cone is indicated by a dotted line.

8.4 Conclusions and Outlook

It is demonstrated that instantaneous velocity fields of the gas phase can be measured in dense sprays by the present flow tagging method. In comparison to well established techniques, such as PDA and PIV, the present technique is much less affected by multiple light scattering, beam steering and beam attenuation in optically thick two-phase flows. This is also the first application of a laser-based flow tagging technique to a spray. The present technique yields the possibility to study the interactions of dispersed and continuous phase in highly particle-laden, evaporating and non-evaporating gas flows, in particular when it is combined with a suitable method to measure the corresponding particle velocity field.

Chapter 9

Droplet Velocity and Acceleration Measurements in Dense Sprays by Laser Flow Tagging

The feasibility of liquid-phase velocity measurements in dense sprays by 2D laser-based flow tagging is demonstrated. Velocity measurements in dense sprays are difficult with conventional techniques because of the high number densities of droplets, the optical thickness of the medium, and multiple light scattering effects. The present flow tagging technique is based on phosphorescent tracer molecules, which are excited by a grid of pulsed "write" laser beams. The motion of the tagged droplet groups can be observed by a CCD camera in this way. In addition, multiple consecutive velocity measurements are performed by "droplet group tracking". This yields the acceleration along the trajectory of individual groups of droplets in unsteady sprays.

9.1 Introduction

Well established laser techniques such as Phase Doppler Anemometry (PDA) and Particle Image Velocimetry (PIV) are frequently used to measure spatially and temporally resolved droplet velocities in sprays [1]. However, severe difficulties are encountered when these techniques are applied to dense sprays. PDA suffers from high number densities of droplets and beam steering in high-temperature environments [2]. PIV is not applicable when the spray is so dense that the detected signal is strongly affected by multiple light scattering [3]. PIV requires that individual particles are resolved, and this becomes impossible when strong multiple scattering results in considerable image blurring. In addition, PIV suffers from strong out-of-plane motion, for example, in swirling sprays. It should be noted that dense sprays are technically important. For example, high-pressure swirl injectors, generating dense hollow-cone sprays, are currently being developed for automotive direct injection spark ignition engines [4], [5]. It is demonstrated in the present study that droplet velocity field measurements can be performed in such dense sprays by laser-based flow tagging. Previous flow tagging techniques are discussed elsewhere [6]-[13]. Most of these techniques require two laser pulses, i.e., "write" and "read" laser pulses, because they are based either on formation of tracer molecules by photodissociation, destruction of fluorescent parent molecules by photodissociation ("bleaching"), or molecular pump and probe mechanisms [6]-[13]. In contrast, flow tagging can also be performed by a single laser pulse when phosphorescent substances are used as the tracer [12], [13]. These techniques are therefore particularly attractive. The spatial position of the laser-excited phosphorescent substances is recorded by a gated camera after being convected by the flow. The use of phosphorescent substances also allows performing multiple consecutive velocity measurements within the phosphorescence lifetime. Thus, the trajectory and acceleration of fluid elements can be determined. This yields additional information, in particular in unreproducible, turbulent flows. It is demonstrated that "droplet group tracking" can be done in this way. It was mentioned above that PDA and PIV encounter severe problems in dense sprays. In contrast, a laser flow tagging technique is hardly affected by multiple light scattering when the distance and width of the tag lines are wide enough, so that they can still be resolved. Beam attenuation does not affect the feasibility of the technique, as long as the tag lines are recognized. Laser beam steering is not an important factor because the spatial positions of the "write" laser beams can be recorded. Therefore, laser flow tagging can be performed in dense sprays. This was demonstrated previously, when the velocity field of the gas phase was measured in a dense spray (see chapter 8). It should also be noted that strong out-of-plane motion is not problematic in most flow tagging experiments. Thus, it is possible to do the measurements, for example, in dense swirling sprays. It is also noteworthy that the three velocity components in a plane can be measured by stereoscopic flow tagging as shown in chapter 7.

9.2 Experimental

Initial measurements have been performed in a hollow-cone gasoline direct injection spray. The prototype swirl injector and electronics were supplied by S. Arndt (Robert Bosch GmbH, Stuttgart). It has been operated with 50bar rail pressure in room air. Ethanol has been used as the fuel. The measurements have been performed at 1ms after triggering the injector, i.e., in the fully developed spray pulse (pulse length: 1.5ms) The maximum droplet density is about $5 \cdot 10^6 cm^{-3}$ in the probe volume. The Sauter mean diameter of the droplets is $d_{32} \approx 15\mu$m [14] (thus, the average droplet spacing at maximum density is $\approx 4 \cdot d_{32}$). This spray is comparable to previously investigated sprays, in which PIV measurements proved to be difficult [3]. The flow tagging set-up is outlined in Fig. 9.1, but the detector is not shown. An image-intensified double-frame "progressive scan" CCD camera (PCO Sensicam) is employed as the detector. It is capable of recording two images with a delay down to $\approx 1\mu$s. The gated image intensifier also acts as a shutter in front of the recording system with a minimum gate length of ≈100ns. It is clear that the gate length determines the extent to which a phosphorescence image is blurred during the exposure time. A Mie scattering image that has been recorded with a thin laser sheet in the central plane of the spray is included in Fig. 9.1 to demonstrate the field of view and the orientation of the spray. The field of view (33mm x 44mm) has been imaged onto the CCD camera under right angles by using a spherical focussing mirror (f=35cm, d=25cm, aluminium). The central region of the spray is illuminated by a "write" laser grid as shown in Fig. 9.1. A frequency-quadrupled (266nm) Nd:YAG laser (Spectra Physics) is used as the laser source. Two sets of "write" laser lines, each ≈1mm x 2mm in diameter ($\approx 70\mu$J/pulse), are created by splitting and focussing the beam of the Nd:YAG laser (Spectra Physics), basically by using two arrays of 15 cylindrical lenses (f = 30 cm).

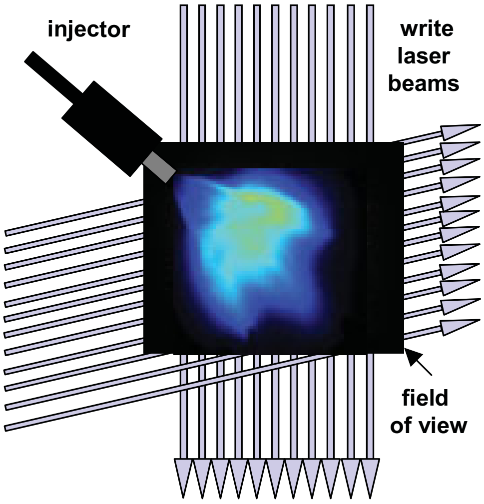

Figure 9.1: Experimental set-up. The intensified CCD camera is not shown. Instead, a Mie scattering image is included showing the spray at 1ms after triggering the injector. Only the first vertical write laser beam on the left hand side is used for the acceleration measurements.

Flow tagging is performed here by using phosphorescent molecules. A lanthanide chelate (Tb^{3+}-dipicolinic acid, Molecular Probes) dissolved in ethanol (10^{-3} M) is employed in the present experiment. Lanthanide chelates are frequently used for time-resolved luminescence measurements, for example, in biology [15], [16]. The lifetime of the terbium chelate is roughly 1ms. It exhibits a broad absorption peak around 280nm. The phosphorescence occurs at two sharp peaks at 491nm and 545nm [16], which are both collected by the camera system. Biacetyl is another interesting phosphorescent molecule that may be used for flow tagging measurements in sprays [13]. However, there are at least two drawbacks compared to lanthanide chelates. First, phosphorescence from biacetyl is easily quenched by oxygen. Thus, the medium must be free of oxygen. Secondly, some of the biacetyl may leave the droplets in the spray due to its high vapor pressure. Thus, some of the phosphorescence may arise from the gas phase and, consequently, there might be cross-talk with the velocity of the gas phase (this problem may be overcome by exploiting phosphorescence quenching by oxygen in the gas phase). It was mentioned in the Introduction that the instantaneous position of the "write" laser lines must be measured in the spray if they are affected by beam steering. This can be done by recording laser-induced emissions (phosphorescence or elastic scattering) at t≈0. It is clear that this calibration image must be acquired in each individual measurement if beam steering fluctuates from pulse to pulse. The double-frame camera mentioned above has been used for this purpose. However, it can be assumed that the position of the laser beams in the spray is reproducible from pulse to pulse in most applications (compare chapter 8). Thus, it is also possible to record the calibration image once in advance. Consequently the double-frame option of the camera could be used for instantaneous acceleration field measurements by recording two images at $t_1 > 0$ and $t_2 > t_1$. However, the trajectory and acceleration of individual droplet groups is measured by acquisition of a series of phosphorescence images in a single frame using the gated image intensifier ("droplet group tracking"). Only one of the write laser beams shown in Fig. 9.1 is used in that experiment in order to avoid overlap of the phosphorescence signals from neighbouring beams in the image.

9.3 Results and Discussion

Fig. 9.2 shows a pair of typical phosphorescence single-shot images measured in the spray with a delay of Δt=15μs. Both images have been measured in an individual spray pulse using the double-frame camera described above. There is no residual Mie scattering in these images because both have been recorded after the laser pulse. Fig. 9.2a) has been measured 1-6μs after the laser pulse, and Fig. 9.2b) has been measured at 16-21μs after the laser pulse (gate length: 5μs). The hollow-cone structure of the spray can be nicely seen in these images. The phosphorescence signal-to-noise ratio is very high (>100) in the droplet mainstream, i.e., close to the edge of the spray cone. In contrast, the signal-to-noise ratio is poor in some regions around the spray axis, in particular close to the nozzle, due to low droplet density.

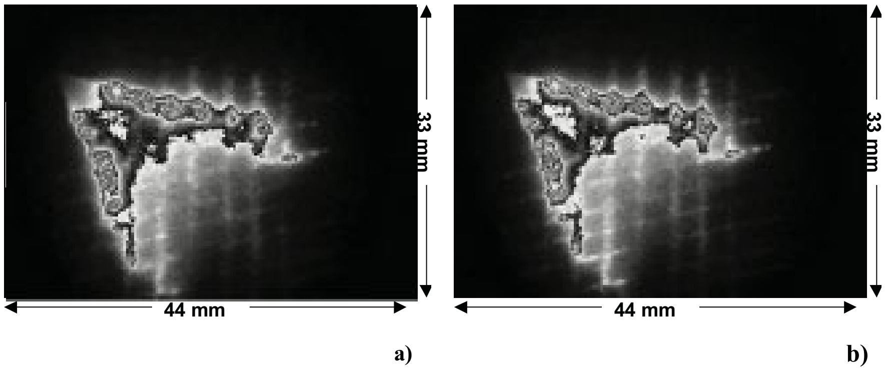

Figure 9.2: Pair of phosphorescence single-shot images recorded in a single spray pulse with a delay of Δt=15μs.

The displacement field of the distorted grid in Fig. 9.2b) with regard to the initial grid in Fig. 9.2a) yields the instantaneous droplet velocity field. The displacement field is found by employing the optical flow algorithm (chapter 2). The resulting instantaneous velocity field is given in Fig. 9.3. One of the "branches" of the droplet mainstream is indicated by a straight line in Fig. 9.3. The velocity magnitude profile along this line is plotted in Fig. 9.4.

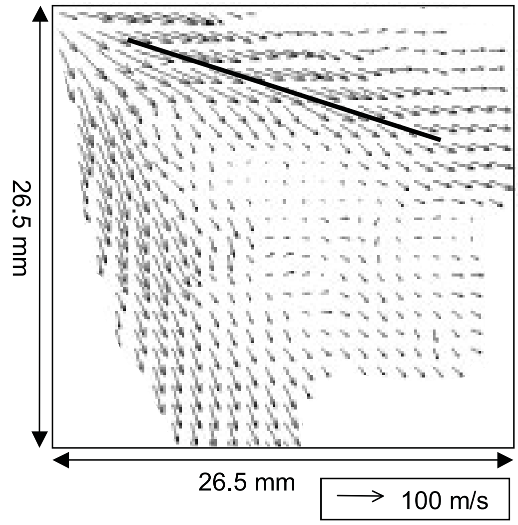

Figure 9.3: Instantaneous droplet velocity field resulting from the image pair in Fig. 9.2.

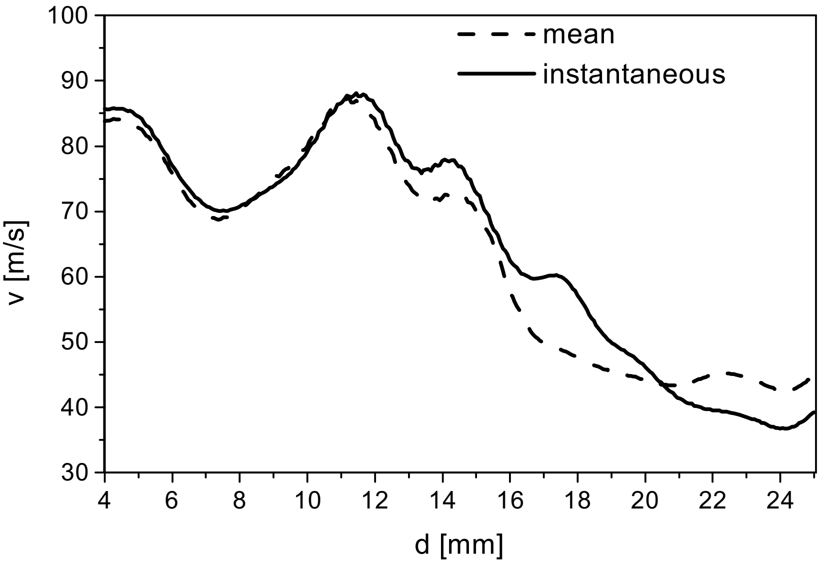

Figure 9.4: Velocity magnitude profile along the straight line in Fig. 9.3 (d is the distance from the nozzle). An instantaneous measurement and the average of 20 instantaneous measurements are given.

The maximum drop velocity found in the mainstream is ≈90m/s. Much smaller drop velocities are found in the inner region of the spray where the droplet density is low. This can be explained by the fact that the droplets in the inner region of the spray are generally smaller than those in the mainstream because they follow the entrainment air flow more easily [4]. It is clear that smaller droplets are decelerated more rapidly than larger droplets. The instantaneous velocity field was found to be quite reproducible from pulse to pulse. In particular, the standard deviation of the instantaneous velocity measurements in the droplet mainstream is in the range 5-10%. It can be seen in Fig. 9.4 that the velocity magnitude profiles in the mainstream of an instantaneous and an averaged measurement are indeed very similar, in particular close to the nozzle. This implies that the relative error of the instantaneous measurements is also smaller than 5-10%, at least in these regions with high signal-to-noise ratio. The mean velocity and standard deviation fields will be discussed in more detail in chapter 10. The spatial resolution of this technique will also be discussed there. Briefly, the resolution is at least half the spacing of the tag lines, i.e., ≈1.6mm in the present application. The velocity distribution in the droplet mainstream is not as uniform or smooth as one might expect. This can be seen in particular in Fig. 9.4.

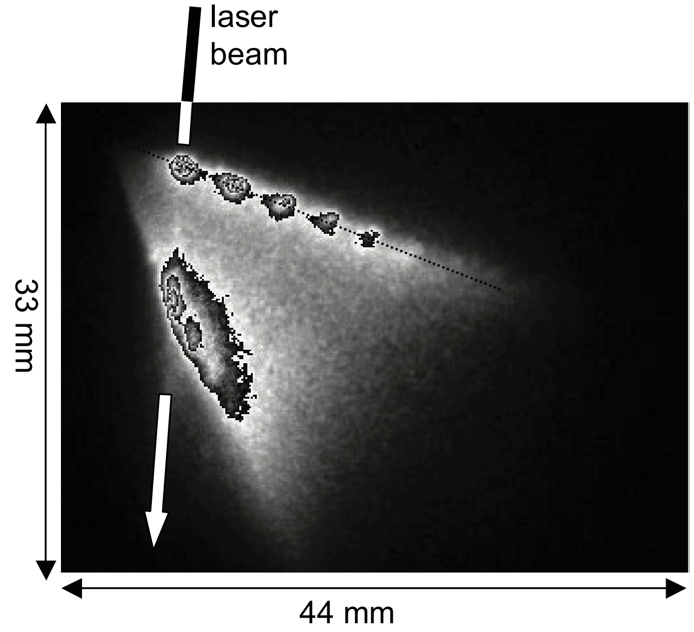

Figure 9.5: "Droplet group tracking" : Unprocessed multi-exposure image measured after a single laser pulse using a single laser beam (Δt=40μs).

There are a number of significant and reproducible velocity peaks and valleys in the droplet mainstream. Most of these structures are clearly resolved, since they larger than the spatial resolution of $\approx$1.6mm. However, the appearance of these structures does not imply that the droplets were accelerated in some regions when they travel in the mainstream. Instead, it will be demonstrated in the following that this velocity distribution is caused by unsteady effects. It was mentioned above that "droplet group tracking" can be performed by a series of instantaneous velocity measurements within the lifetime of the phosphorescent tracer. A typical unprocessed CCD image is given in Fig. 9.5. It results from 10 exposures (Δt=40μs, gate length = 3μs) after a single laser pulse. Only one of the write laser beams is used in this experiment, which is indicated in Fig. 9.5. A well defined group of droplets in the upper branch in the droplet mainstream is illuminated by this laser beam. The vertical extension of the droplet group is limited by the dimension of the droplet distribution in the upper mainstream. This results in a number of well resolved phosphorescence spots in the image in Fig. 9.5. It can be seen in the image that the illuminated droplet group in the lower branch is not as well defined due to an unfavourable angle of the laser beam with regard to the lower mainstream.

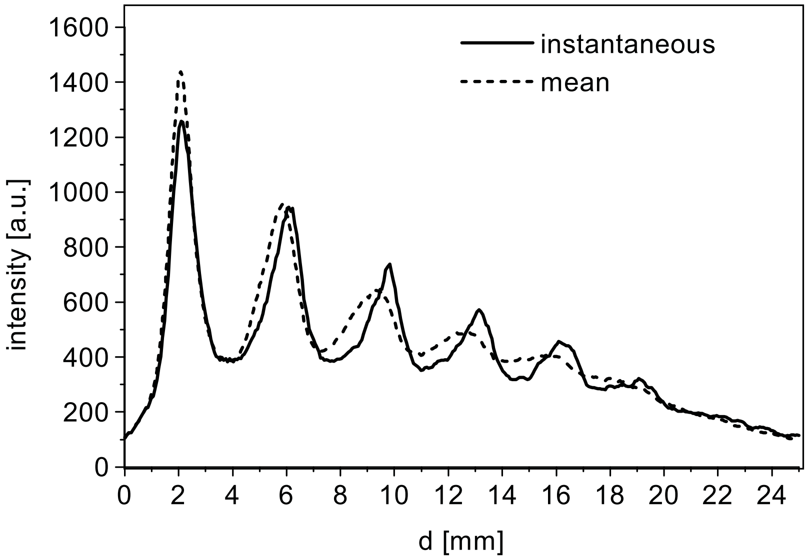

Figure 9.6: Unprocessed image intensity profile along the dotted line in Fig. 9.5 ("instantaneous") and corresponding profile from an image averaged over ten measurements ("mean"); d is the distance from the nozzle.

Thus, only the upper branch is considered in the following. Measured images like Fig. 9.5 turned out to be quite reproducible. A corresponding profile from an image averaged over 10 measurements is also shown. It can be seen that it is quite similar to the "instantaneous" measurement, although the phosphorescence spots are blurred. It is clear that the position of the phosphorescence spots and their spacing represent the trajectory and instantaneous velocities of the illuminated droplet group. It can be observed in Fig. 9.5 that the trajectory can be approximated by a straight line (dotted line). An image intensity profile along this line ("d axis")is plotted in Fig. 9.6. At least 6 phosphorescence spots can be seen in Fig. 9.5 and Fig. 9.6.

The intensity of these spots decreases from left to right, basically because of the dispersion of the droplet group (see below) and due to the phosphorescence decay. It can also be seen in Fig. 9.5 that these spots are sitting on a broad background (≈200 arbitrary units, compare Fig. 9.6) that arises basically from multiple light scattering. The first six phosphorescence spots in Fig. 9.6 yield five consecutive velocity measurements, which are plotted in Fig. 9.7. The accuracy of these measurements can be estimated to be ≈5% in the average, based on the displacements and the uncertainty to determine the center of the phosphorescence spots (Fig. 9.6 shows clearly that the error of the measurements closer to the nozzle is smaller than the error of the measurements further downstream). The data in Fig. 9.7 show that the deceleration, a, is uniform (within the measurement uncertainty) across the field of view ($a = -1.4 \cdot 10^5 \ \frac{m}{s^2}$).

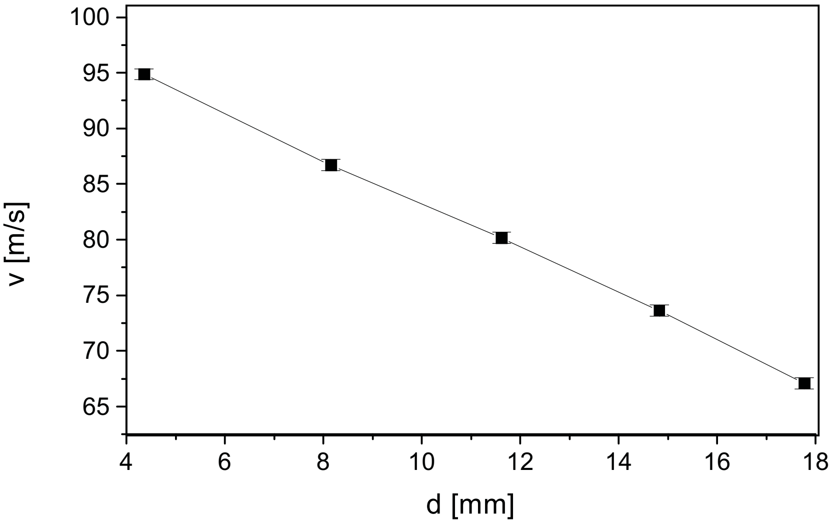

Figure 9.7: Five consecutive velocity measurements resulting from Fig. 9.5 and the "instantaneous" image intensity profile in Fig. 9.6.

It should be noted that this velocity profile is significantly different to the instantaneous profile in Fig. 9.4, which has been determined in the same region. Consequently, the large "oscillations" of the velocity found in the instantaneous (and mean) velocity fields, in particular close to the nozzle, are due to unsteady spray behaviour. This means that the droplet velocity field within each spray pulse is time dependent, for example due to variations in the fuel flow through the nozzle. However, these variations are found to be quite reproducible from pulse to pulse as seen in Fig. 9.4. The "droplet group tracking" measurements also yield information on the dispersion of individual droplet groups. The extension of the droplet group is approximately given by the width (FWHM) of the phosphorescence spots. The measurement shown in Fig. 9.5 has been repeated 20 times and the data have been averaged over this ensemble in order to reduce the noise. The resulting FWHM (in the direction of the d axis) is given in Fig. 9.8. It can be seen that the width of the droplet groups increases continuously by a factor of ≈2 over a distance of 14mm.

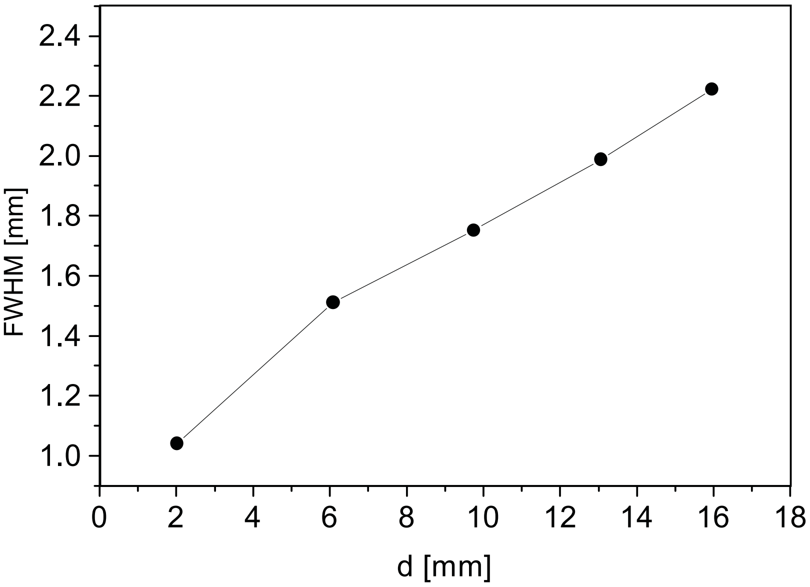

Figure 9.8: Width of consecutive phosphorescence spots as a function of d (distance from the nozzle). The data are averaged over 20 "single-shot" measurements (compare Fig. 9.5).

Such information can be used to study the droplet-gas and droplet-droplet interactions in the spray.

9.4 Summary and Conclusions

It is demonstrated that instantaneous droplet velocity fields can be measured in dense sprays by the present flow tagging method. In comparison to well established techniques, such as PDA and PIV, the present technique is much less affected by multiple light scattering, beam steering and beam attenuation in optically thick two-phase flows. The flow tagging technique based on a phosphorescent tracer can in principle be performed by a single laser source and a single-frame camera. It is noteworthy that the technical effort of typical double-pulsed PIV measurements is higher. Furthermore, it is demonstrated that the trajectory and acceleration of individual droplet groups can be determined by a number of consecutive velocity measurements. This yields additional information on the dynamic motion of the droplets and the interaction with the gas phase. The latter can be studied more thoroughly by combining the present technique with the gas-phase velocimetry method proposed in chapter 8. We did also flow tagging measurements in the dense spray close to a wall in order to investigate spray-wall interaction. Such results will be presented in chapter 10.

Chapter 10

Flow Tagging Measurements in Dense Gasoline Direct Injection Sprays Close To a Wall

10.1 Introduction

High-pressure swirl injectors, generating dense hollow-cone sprays, are currently being developed for automotive direct injection spark ignition engines [3],[4],[5]. It was demonstrated that 2D velocity measurements of the gas and liquid phase can be performed in such sprays by 2D Laser Flow Tagging (LFT) techniques. Further results are given in the present chapter. In particular, measurements in the spray close to a WALL are presented. It is demonstrated that the interaction of the spray with a metal WALL can be studied in this way. The interaction of gasoline direct injection sprays with walls is important, in particular for wall-guided mixture preparation systems [4],[5]. Previous laser-based flow tagging methods have been discussed before (chapters 8 and 9). The present LFT experiment is performed by exciting a phosphorescent tracer, which is dissolved in the fuel, using a write laser grid. The spatial position of the laser-excited phosphorescent molecules is recorded by a gated camera after being convected by the flow. The technical effort of this LFT technique is relatively low, because only one (single-pulsed) laser source and a gated single-frame camera is needed. It is noteworthy that the use of phosphorescent substances also allows performing multiple consecutive velocity measurements within the phosphorescence lifetime, for example, by using a multi-frame camera as the detector or by "droplet group tracking", which has been described previously (chapter 9). It was mentioned above that PDA and PIV encounter severe problems, such as multiple light scattering and laser beam attenuation/steering etc., in dense automotive sprays. It should be emphasized that LFT is hardly affected by multiple light scattering when the distance and width of the tag lines are wide enough so that they can still be resolved. Beam attenuation does not affect the feasibility of LFT, as long as the tag lines are recognized. Laser beam steering is not an important factor because the spatial positions of the write laser beams are recorded by a "double-frame" camera. Therefore, LFT can be performed in dense sprays. It should also be noted that strong out-of-plane motion is not problematic in most LFT experiments, in contrast to most PIV applications. Thus, it is possible to do the measurements, for example, in dense swirling sprays. It is also noteworthy that the three velocity components in a plane can be measured by stereoscopic LFT (see chapter 7).

10.2 Experimental

10.2.1 Spray

Initial measurements have been performed in a hollow-cone gasoline direct injection spray. The prototype swirl injector and electronics were supplied Robert Bosch GmbH, Stuttgart. It has been operated with 50bar rail pressure in room air. Ethanol has been used as the fuel. The measurements have been performed at different times, t, after triggering the injector. The spray pulse length is 1ms. The maximum droplet density is about $5{\cdot}10^6/\mathrm{cm}^3$ in the probe volume. The Sauter mean diameter of the droplets is $\mathrm{D}_{32} \approx 15\mu$m (thus, the average droplet spacing at maximum density is $\approx 4\cdot\ \mathrm{D}_{32}$). This spray is comparable to previously investigated sprays, in which PIV measurements proved to be difficult [3].

10.2.2 Measurement system

The experimental set-up is outlined in Fig. 10.1, but the detector is not shown. The central plane of the spray is illuminated by a write laser grid. A resulting phosphorescence image that has been recorded at t=1.5ms after triggering the injector (averaged over 20 spray pulses) is included in Fig. 10.1. Almost the whole spray is illuminated by the write laser grid because of multiple light scattering. Thus, the image roughly shows the distribution of the droplets, although the signal intensity on the grid is stronger than in the gaps. The field of view (33mm x 44mm) has been imaged onto a CCD camera under right angles by using a spherical focussing mirror. An image-intensified double-frame "progressive scan" CCD camera (PCO Sensicam) is employed as the detector. Phosphorescence images are acquired with a short gate length (3μs) using the image intensifier. The CCD camera is capable of recording two images with a delay down to $\approx 1\mu$s. The initial grid (initial distribution of the excited molecules) and the distorted grid are recorded by this camera in each individual spray pulse. Thus, the technique is not affected by any possible beam steering.

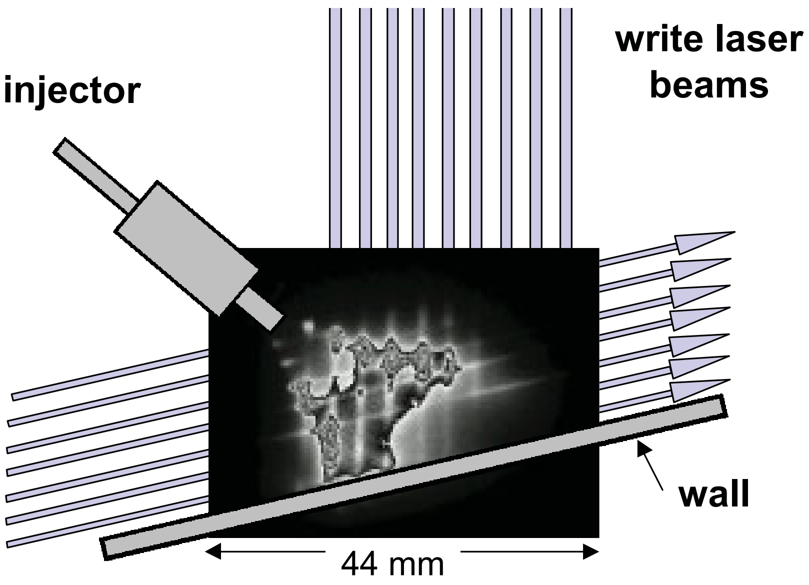

Figure 10.1: Experimental set-up; camera system is not shown

A frequency-quadrupled (266nm) Nd:YAG laser (Spectra Physics) is used as the laser source. Two sets of write laser lines, each ≈ 1mm x 2mm in diameter (70μJ/pulse), are created as described previously. The vertical beams directly impinge on the wall, whereas the "horizontal" beams are parallel to the wall (see Fig. 10.1). Droplet tagging is performed by using phosphorescent molecules. A lanthanide chelate (Tb^{3+}-dipicolinic acid, Molecular Probes) dissolved in ethanol (10^{-3} M) is employed in the present experiment. The phosphorescence lifetime of the terbium chelate is roughly 1ms. It exhibits a broad absorption peak around 280nm. The phosphorescence occurs at two sharp peaks at 491nm and 545nm which are both collected by the camera system.

10.3 Results and Discussion

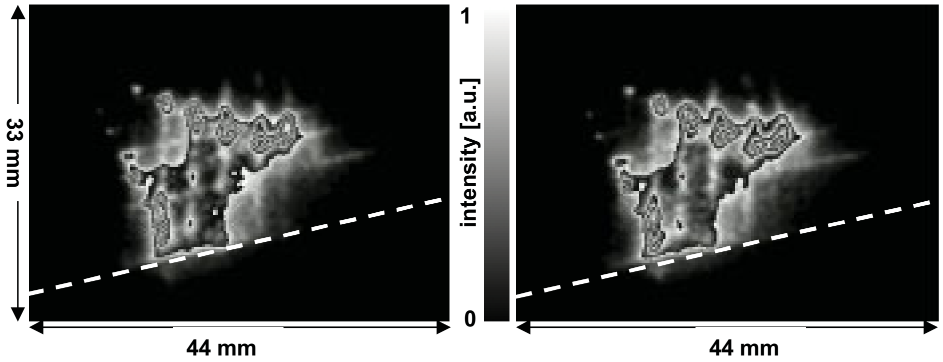

Figure 10.2: Pair of double-pulse single-shot phosphorescence images at t=1.5ms

Fig. 10.2 shows a pair of typical phosphorescence single-shot images measured in the spray impinging on the wall with a delay of $\Delta t = 10\mu$s (at t=1.5ms after triggering the injector). Both images have been measured in the same spray pulse using the double-frame camera. There is no residual Mie scattering or stray light from the wall in these images because both have been recorded after the laser pulse (gate length: 3μs). The image on the left hand side has been measured at 1-4μs after the laser pulse, and the other image has been measured at 11-14μs after the laser pulse. The hollow-cone structure of the spray can be seen in these images. The displacement field of the distorted grid on the right hand side in Fig. 10.2 with regard to the initial grid on the left side in Fig. 10.2 yields the instantaneous droplet velocity field. The displacement is found by employing the optical flow algorithm. The resulting instantaneous velocity field is given in Fig. 10.3.

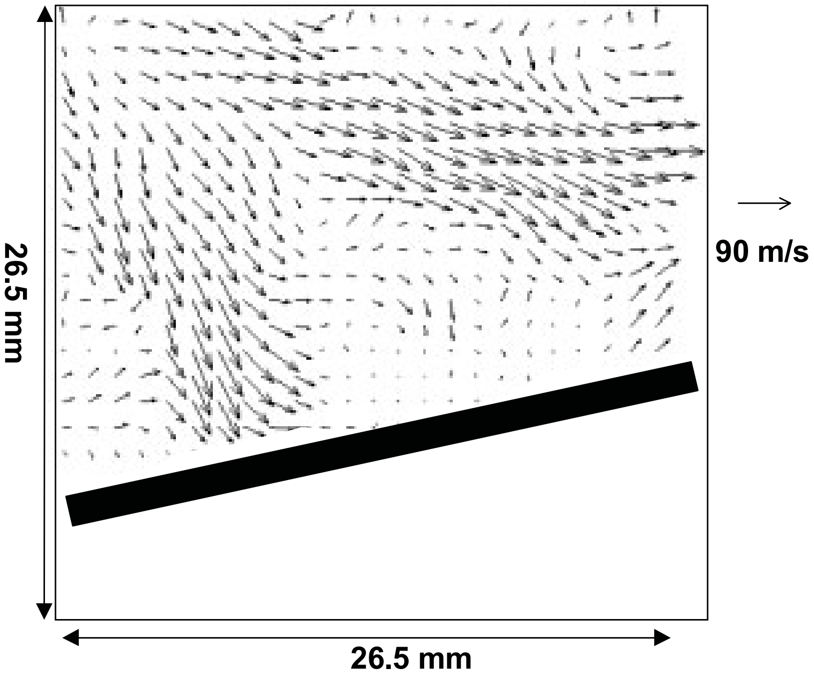

Figure 10.3: Instantaneous velocity field resulting from the two phosphorescence images in Fig. 10.2

Mean velocity fields have been computed from 20 instantaneous measurements. A series of mean velocity fields that have been measured at different times, t, in the spray pulse are shown in Fig. 10.4 (right hand side). Corresponding (averaged) phosphorescence images are given in the left column. Obviously, the instantaneous velocity field in Fig. 10.3 and the corresponding mean velocity field (3rd row in Fig. 10.4) are quite similar, in particular close to the edge of the hollow cone, where the droplet density is high. Shot-to-shot fluctuations will be discussed in more detail below based on standard deviation fields. The phosphorescence image in the first row of Fig. 10.4 (t=0.9ms) basically shows the first part of the spray pulse, which exhibits high droplet density on the spray axis ("pre-spray"). The velocity field on the right hand side shows that the largest velocities of the "pre-spray" also occur on the spray axis. However, in the upper left corner of this field there are even larger velocities, that arise from the tip of the "main spray". The latter exhibits the typical hollow-cone structure. This can be seen more clearly in the images and velocity fields in the 2^{nd} and 3^{rd} rows. The "main spray" is fully developed in the third row (t=1.5ms), and its lower branch just reached the metal wall. The last row in Fig. 10.4 (t=1.8ms) shows the trailing end of the spray pulse. The hollow-cone structure is collapsed, and high droplet density can be seen on the spray axis, in particular close to the wall. Accordingly, the hollow-cone structure is also no longer visible in the velocity field at t=1.8ms. Instead, much smaller velocities occur across the field of view and some vortices show up in the upper right and lower left corners, in contrast to the earlier velocity fields. Similar velocity measurements have been done previously in the "free" spray, i.e., without a wall, at t=1.3ms (chapter 9). The influence of the wall can be investigated by comparing these results with the present measurement at a similar time in the spray pulse (t=1.5ms, 3rd row in Fig. 10.4). First, one observes that the velocity field close to the wall is altered only within the first few millimetres ($<$5mm) above the surface. The lower main branch, that impinges on the wall nearly perpendicularly, is significantly decelerated only within the last $\approx$ 2 millimetres above the wall. Secondly, one finds that the upper branch of the main spray is slightly bent upwards in the present measurement. This may also be caused by wall-induced air flow. However, it is not a significant change. The spatial resolution and accuracy of such LFT measurements have been discussed previously (chapter 9). The measurement error of the instantaneous velocity fields can be estimated to be 5-10% (except in some regions of the velocity fields, where the droplet density is low; such data has been mostly suppressed in the velocity fields given above). It can be assumed that the accuracy of the mean velocity fields is better. The spatial resolution of the measurements can be estimated to be half the spacing of the tag lines in both directions as mentioned before. This is about 1.6mm in the present case. It can be estimated in a first approach that LFT measurements can be performed at a distance of about 1mm from the wall. The phosphorescence signals can be recorded even closer to the wall because there is no interference with stray light as mentioned before.

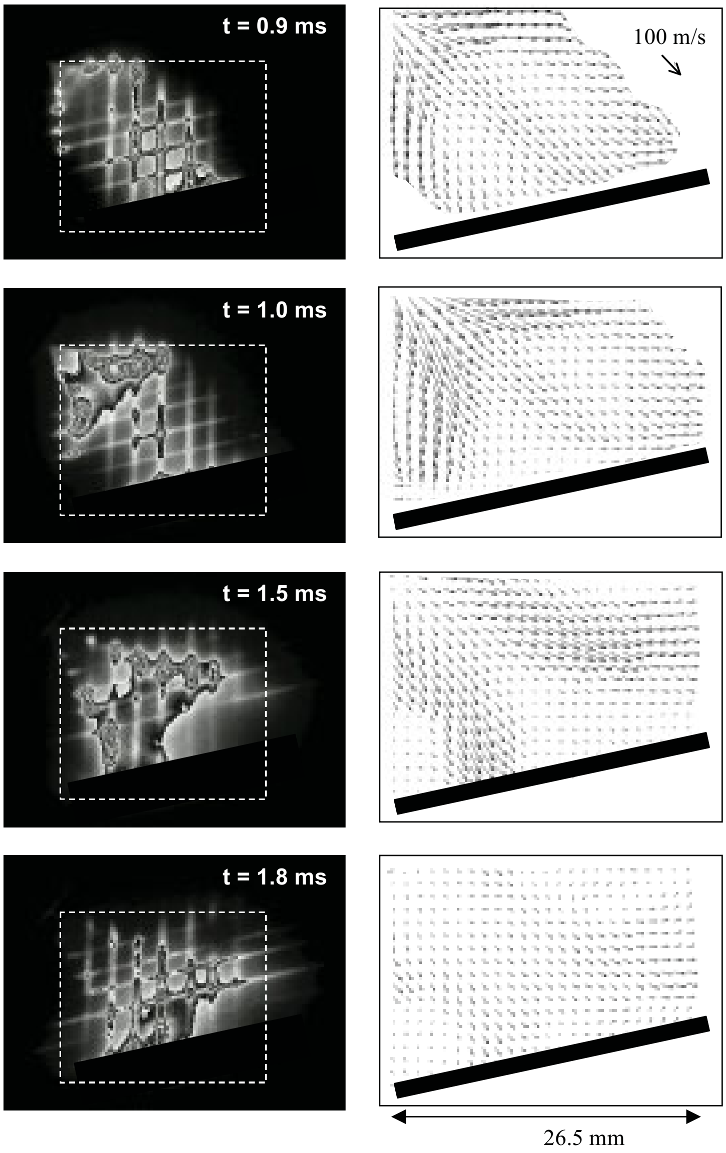

Figure 10.4: Series of phosphorescence images (left) and corresponding mean velocity fields (right) measured at different times, t, in the spray pulse. The inner rectangles in the images on the left hand side indicate where the velocity fields have been determined

However, it should be noted that a certain displacement of the tagged droplets is required, and this sets a lower limit for the measurement distance above the wall, in particular if the flow is directed more or less perpendicular to the wall. The minimum required distance is about $s = v \cdot t = 100\text{m/s} \cdot 10\mu\text{s} = 1$ mm. Some details of the "pre-spray" and the "main-spray" can be observed more clearly in the corresponding velocity magnitude fields which are given in Fig. 10.5 (upper row). It was observed previously that the velocity distribution in the droplet mainstream of the "free" spray is not as uniform as one might expect (chapter 9). These velocity peaks and valleys in the mainstream are also present in the corresponding present velocity fields at t=1.0ms and t=1.5ms.

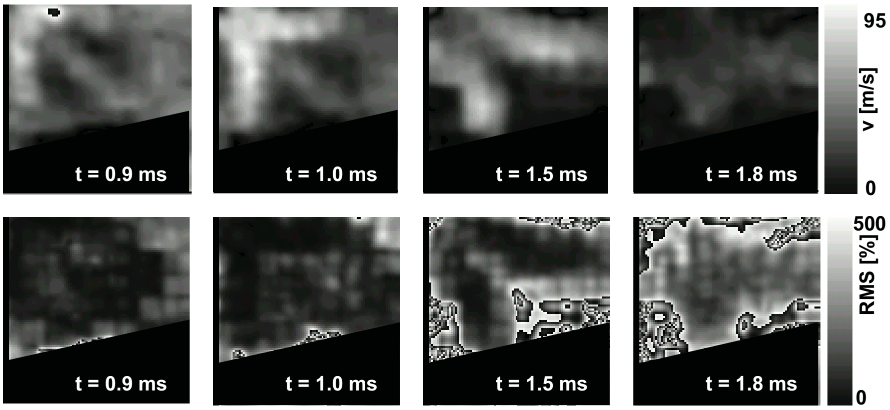

Figure 10.5: Mean velocity magnitude (upper row) and standard deviation (lower row) fields

The standard deviation (RMS) of the instantaneous velocity magnitude is plotted in the lower row of Fig. 10.5. These images essentially show the pulse-to-pulse fluctuations of the spray, since the fluctuations are generally larger than the measurement error (except in regions where the droplet density is very low). The structure of the RMS fields at t=1.0ms and t=1.5ms is comparable to the RMS field measured in the "free" spray at t=1.3ms, except very close to the wall. The RMS is relatively low on the two branches of the hollow cone, i.e., in the mainstream of the droplets. The absolute RMS was determined to be 5-10% in this region of the "free" spray. In contrast, the RMS is ≈ 25% at t=1.0ms and ≈ 45% at t=1.5ms on the main branches in the present measurements (far away from the wall). This is a significant difference.

10.4 Summary and conclusions

It is demonstrated that velocity measurements can be performed in a dense automotive spray impinging on a flat metal wall by a recently developed LFT technique, which is based on phosphorescent molecules. The velocity measurements are not affected by stray light because the phosphorescence signal is acquired after the laser pulse. Thus, the measurements can be performed close to the wall (≈ 1mm in the present state). It is noteworthy that the technical effort of this LFT technique is relatively low, because only one (single-pulsed) laser source and a gated single-frame camera is required (although a double-frame camera is used). Essentially, it is found in the present experiment that the mean velocity field of the fully developed "main spray" is significantly altered by the wall only within the first few millimetres above the surface under the present conditions. On the other hand we found that the pulse-to-pulse fluctuations (RMS) of the instantaneous velocities in the droplet mainstream are significantly increased compared to the "free" spray.

Chapter 11

Microdroplets

11.1 Introduction

The evaporation of one-component mono-disperse microdroplets with a size of approximately 90 microns was investigated. The droplets were embedded in the air flow of a windtunnel. The velocity magnitude of the laminar air flow was adjustable within the range of 0-10 m/s. For the generation of the mono-disperse microdroplets an appropriate aerosol generator was built. Besides its narrow droplet size distribution a small and aerodynamic shape of the generator was requested in order to assure that the air flow is not stronger disturbed. To improve the long time stability of the flow the windtunnel was additionally equipped with a control loop. The source of microdroplets was characterized and evaporation measurements were performed. The evaporation rate of different liquids as well as the dependence of the evaporation rate on the surrounding air flow were investigated with this set-up.

11.2 Set-up

The experimental set-up is shown in Fig. 11.1. A frequency doubled Nd-YAG at 532 nm, providing pulses with an energy of $\approx$ 120 mJ and a pulse duration of 7 ns, was used as the source of light. The laser beams was divided into two identical beams by means of a 50/50 beam-splitter. These 2 partial beams reached the probe volume at different heights. The difference in height was 11 mm. The emitted radiation due to Mie scattering was imaged onto a CCD. Camera and imaging optics could be moved by a z-translator. The position of the droplets inside the windtunnel could be adjusted similarly by an x-y-translator unit. All translator units were controlled by a PC. Thus small fluctuations of the positions of the droplets that are due to changes in the flow conditions could be corrected online.

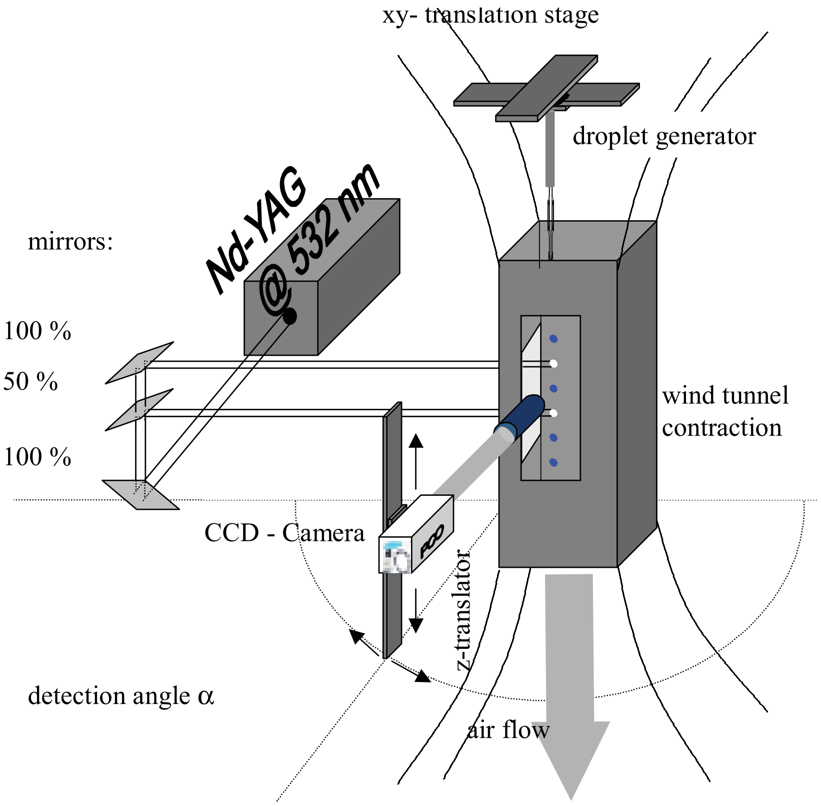

Figure 11.1: Set-up for evaporation measurements.

11.2.1 The Windtunnel

In Fig. 11.2 the windtunnel is depicted. Air flow and droplet motion were parallel for the investigation of small relative velocities. Counter flow and cross flow arrangements can be realised as well. The laminarity of the flow is achieved by leading the incoming air into a thick layer of a porous medium. Thus the flow field is homgenized.

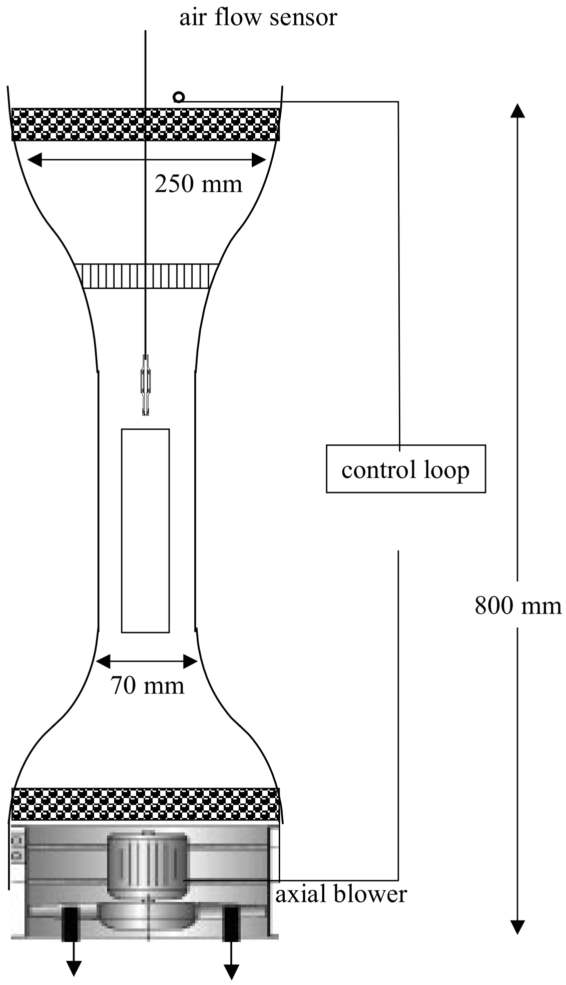

Figure 11.2: Schematic sketch of the windtunnel facility.

The air flow is accelerated when entering the wind tunnel contraction region. Finally a honeycomb mounted at the end of the contraction zone improves the laminarization of the flow. The contraction generates a flat top flow profile as generally known from literature. The windtunnel was studied in detail in previous work ([91]). Its flow properties are known from PIV measurements. The flow sensor of the control loop, that continuously measures the adjusted flow velocity, was mounted at the center of the upper part of the windtunnel. The velocity in the contraction zone can be roughly estimated by applying the contraction ratio (the standard deviation of the control loop is estimated by the manufacturer to be about 1%).

11.2.2 The Aerosol Generator

The principle of this aerosol generator is based on a contraction of the effective tube diameter. Other aerosol generators based on a salt-shaker principle or on the oscillation of the pinhole disc are known from literature ([92]).

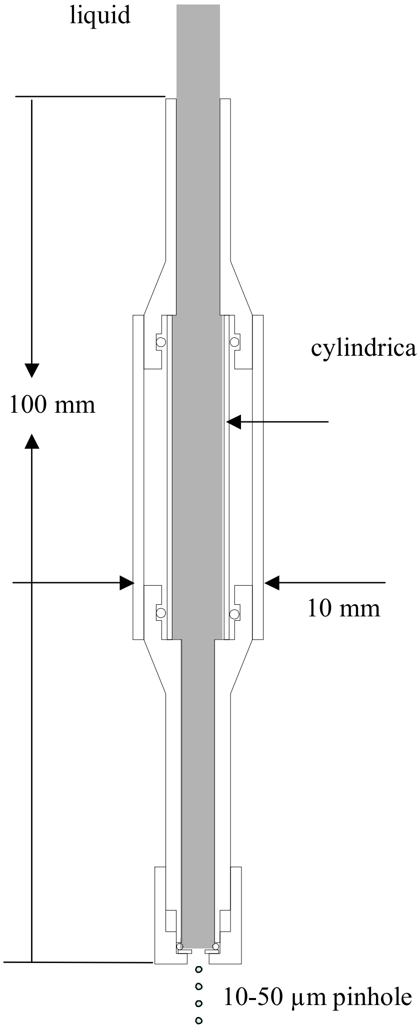

Figure 11.3: The aerosol generator. The narrow shape makes it suitable for use in small windtunnels, especially in co-flow set-ups.

The contraction of the volume is done by the oscillation of a cylindrical shaped piezo ,mounted with seal rings inside the casing, which is flown through by the liquid (Fig. 11.3). An outstanding property of this aerosol generator is its narrow extension (D = 10 mm), which makes the use in co-flow set-ups inside narrow windtunnels possible without strong disturbance of the laminar flow.

The aerosol generator was generally operated at low pressures ($<$ 1bar). The pressure is sufficient to induce a steady liquid running out of the 40 μm - pinhole. The oscillation of the piezo induces the Rayleigh break-up. So called "drop on demand"-operation was found to be possible, too.

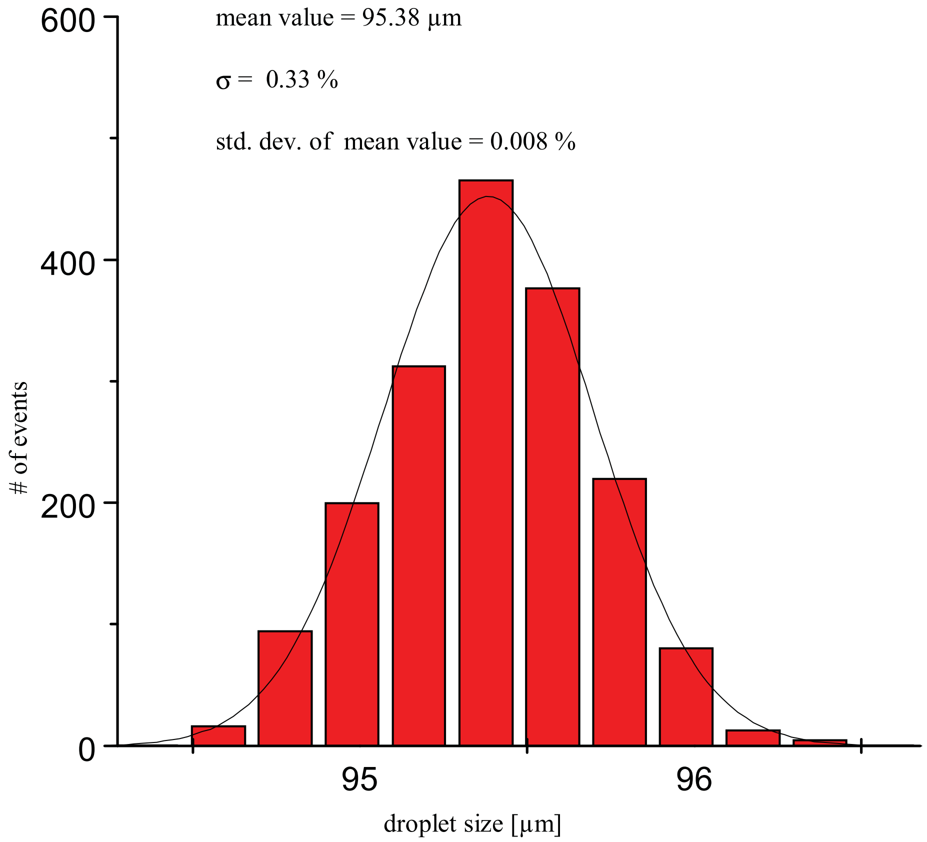

Figure 11.4: Drop size statistics based on 2000 droplets. This statistical accuracy was used for all forthcoming evaporation measurements.

The droplet generator produces droplets with the droplet size distribution shown in Fig. 11.4 ($\sigma \approx 0.3\%$). As the Rayleigh break-up is induced by an effective volume contraction, the properties of the aerosol generator are merely affected by external disruptive factors (wind tunnel vibrations etc.), because the periodic oscillations of the piezo are dominant. The standard deviation of the mean value of n droplets given in Fig. 11.4 was determined according to equation (11.1). Values determined in this way were checked by performing checks of the reproducibility of the evaporation measurement.

$$\sigma_{arith} = \frac{\sigma}{\sqrt{n}} \tag{11.1}$$

These experimentally determined values were always comparable. In the upper case the relative measurement error was 0.01 %.

11.3 The Measurement Technique

11.3.1 Improvement of ILIDS

A Mie scattering technique to determine the size of spherical microdroplets has been improved for the need of high accuracy in three-dimensional systems. In the literature this technique is often referred to as ILIDS (Interferometric Laser Imaging Droplet Sizing). The technique was first demonstrated in [73]. Recently ILIDS was applied to droplets in technical sprays in [81], which is a typical 3D problem. The measurement principle relies on the evaluation of the Mie scattering radiation recorded in the forward scattering direction (40°-80°). In this domain of the scattering angle a regular interference pattern occurs that can be quantitatively understood as the interference of the reflected and refracted light waves emitted by the droplet. The droplet diameter can be deduced from the interference pattern by means of equation 11.2. According to [76] the general relation between droplet diameter D and the number of interference maxima (fringes) N is given by:

$$D = \frac{2\lambda N}{\alpha} \frac{1}{\cos(\frac{\Theta}{2}) + \frac{m \sin(\frac{\Theta}{2})}{\sqrt{m^2+1-2m\cos(\frac{\Theta}{2})}}} \tag{11.2}$$

, where $\frac{N}{\alpha}$ is the number of fringes in the collecting angle α, m the refractive index, λ the laser wavelength, θ the detection angle and D the droplet diameter. The interference structure in the region around 60° is approximately independent of the refractive index of the liquid. Thus it is independent of slight changes of the droplet temperature. According to [75] the spacing $\Delta\theta$ of the interference fringes around $\theta = 60°$ is given by equation 11.3

$$\Delta\theta = 1,129 \cdot \frac{180°}{\chi} \tag{11.3}$$

$$\chi = \frac{\pi D}{\lambda} \tag{11.4}$$

Thus the measurement technique is independent of the droplet temperature.

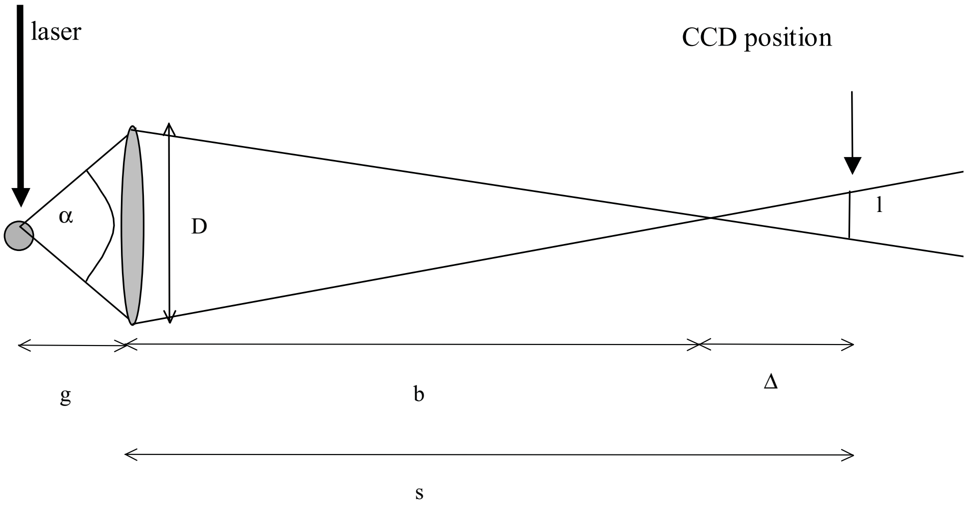

Figure 11.5: Sketch for the deduction of equation 11.5. Only the light rays reaching the optics from the entrance point of the laser beam are shown.

In 3D applications the correction of the effective collecting angle α, that depends on the distance of the droplet from the imaging optics (see Fig. 11.5), is the most critical part of this technique. In [75] the accuracy is specified to be about 4 %, in [73] about 2% . Especially the correction of the collecting angle of each single droplet signal provided a possibility for improvement. A collecting angle of 20° is used to detect the scattering signal but only a small part of the signal (about 20 fringes around $\theta = 60°$) is used to determine the fringe spacing, ensuring its independence of the refractive index. The large collecting angle however is needed to achieve a high precision in determining the effective collecting angle, that varies from droplet to droplet due to fluctuations in the y-position of the droplet in 3D systems as will be discussed in detail later in this chapter.

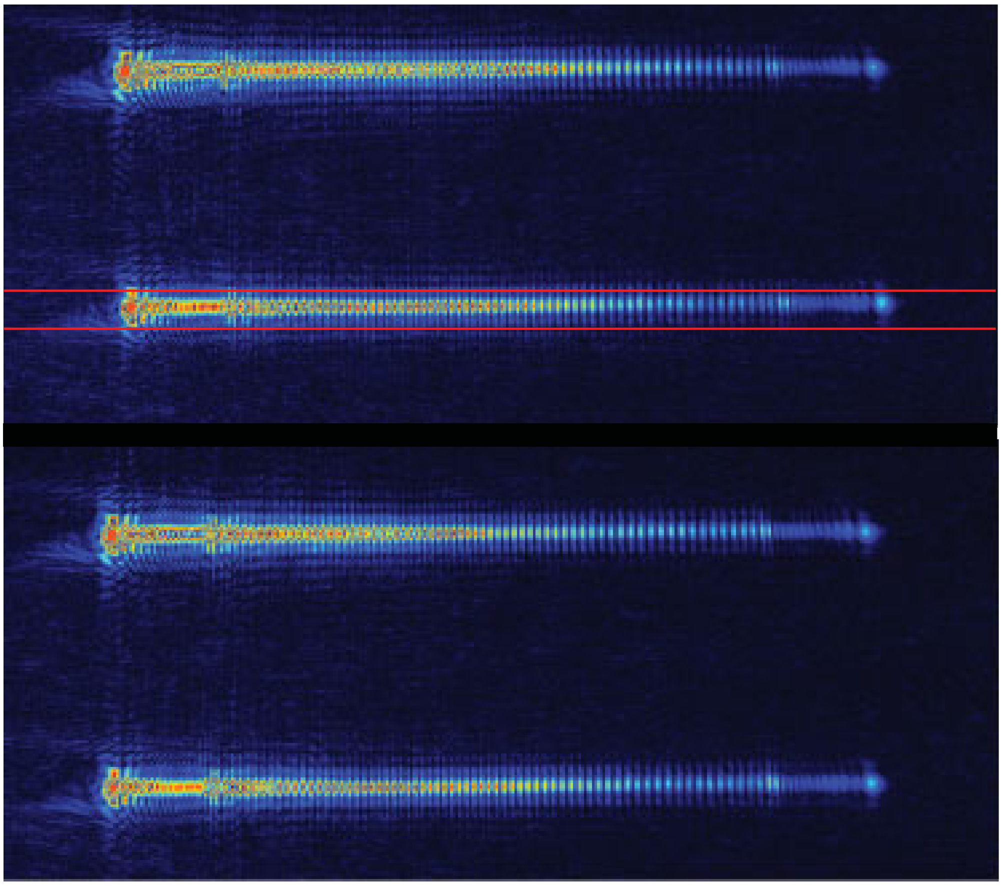

Figure 11.6: Typical raw data. The signals of 4 droplets can be seen. Each horizontal signal pattern gives the intensity I as a function of the scattering angle θ within a certain range. From $I(\theta)$ the droplet size can be deduced.

Fig. 11.6 shows a typical raw image. The Mie scattering signal of 4 droplets in the out-of-focus plane can be seen as 4 separated horizontally orientated signals $I(\theta)$. The horizontal extension of the signals is given by the edge of the imaging optics while the vertical one is determined by a horizontal slit mounted in front of the imaging optics. In this way overlapping signals from neighbouring droplets are avoided and thus the smallest possible distance between droplets is reduced. This is very important for evaporation studies in droplet clusters. The collecting angle α is determined from the total horizontal extension of the signal as illustrated in Fig. 11.7.

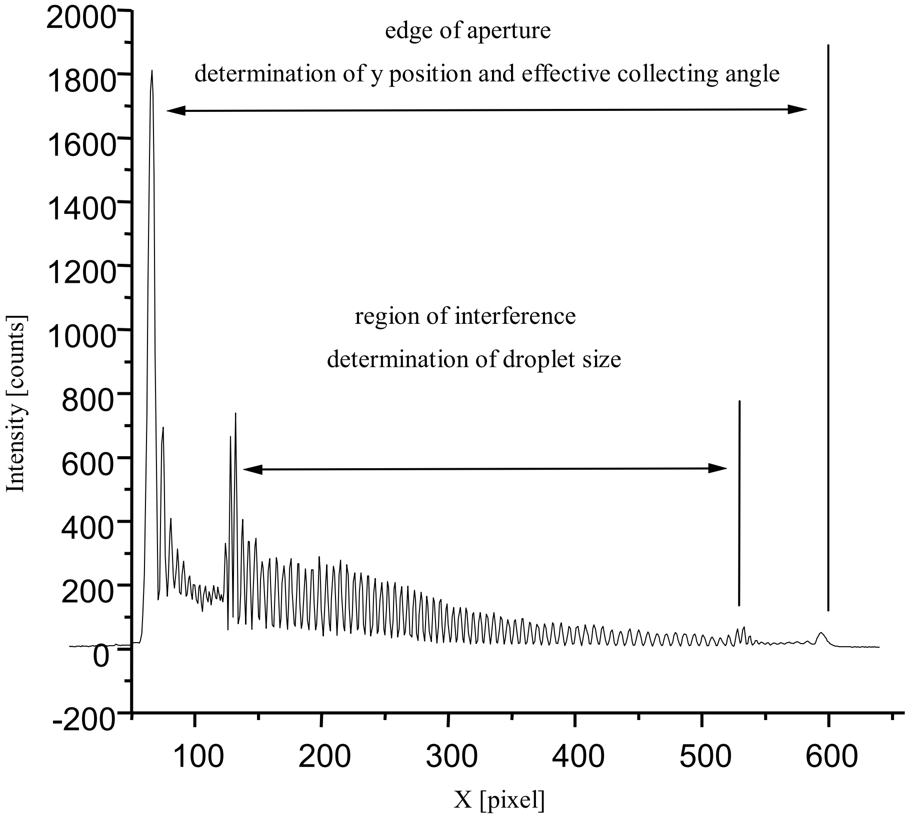

Figure 11.7: Typical profile taken from the 2nd droplet in Fig. 11.6

The relation of the horizontal extension of one glare point (for example from the reflected part of the light) l and the collecting angle α can be determined by geometrical analysis to be:

$$\alpha(l) = 2 \cdot \arctan \frac{D}{2 \cdot \frac{f \cdot \frac{D \cdot s}{D+l}}{\frac{D \cdot s}{D+l} - f}} \tag{11.5}$$

See Fig. 11.5 for the corresponding geometry.

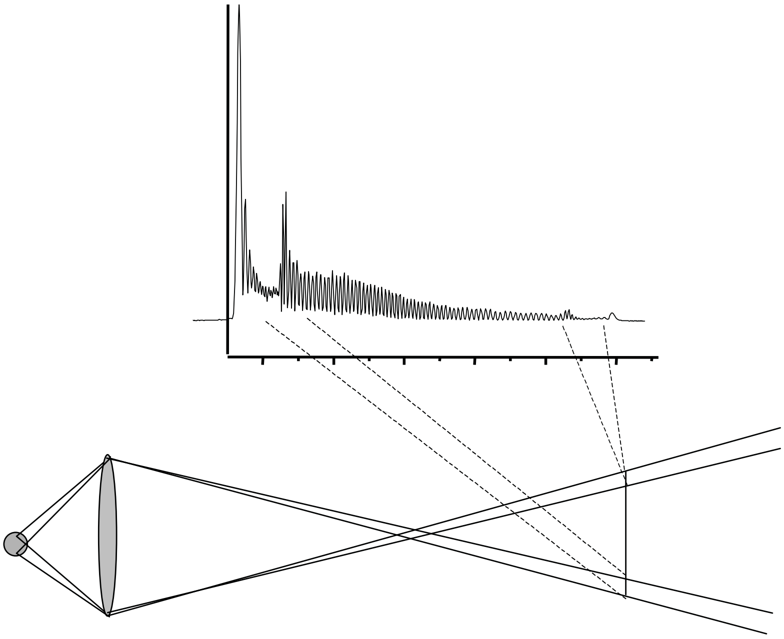

Figure 11.8: Consideration of reflected and refracted light waves with regard to the origin of the signal in Fig. 11.7

The maxima located at the edge of the signal arise from Fresnel diffraction at the edge of the aperture of the imaging optics and are clearly separated from the region, where interference occurs. The horizontal extension of the signal is derived from the distance between the outer right and outer left maximum. From this extension l can be derived, which is the important quantity in the determination of the collecting angle. The separation of said regions, where interference or pure signal from one glare point respectively occurs, which is achieved by the combination of a high magnification of 7.6 with a large average collecting angle of about 20°, is the needed for a high precision in the determination of the real collecting angle. Figs. 11.9 and 11.10 show the effect of this angle calibration. Fig. 11.9 feigns a broad droplet size spectrum. The width of the distribution is dominated by the fluctuations of the y-positions of the droplets due to the surrounding air flow. After the application of the calibration procedure the distribution width of the droplet sizes including the measurement error remains.

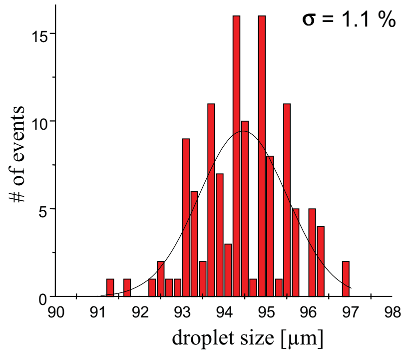

Figure 11.9: Without aperture correction

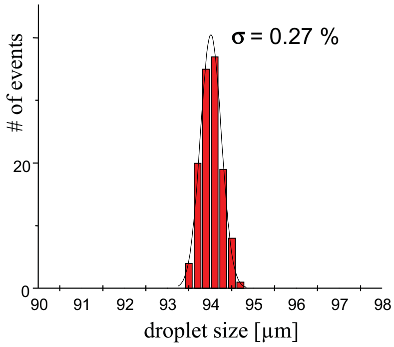

Figure 11.10: With aperture correction

The FWHM is determined to be $\sigma \approx 0.3\%$. The width of the droplet distribution of the aerosol generator can therefore be assumed to be of the same order or even less. This value is comparable to other aerosol generators reported in the literature.

11.4 Experimental Results

11.4.1 Investigations of the droplet source

First of all the long term stability of the droplet size spectrum produced by the aerosol generator (see 11.3) had to be checked. Corresponding measurements were carried out inside the windtunnel at well defined air flows to avoid an accumulation of vapour which would have reduced the evaporation rate of the droplets. Thus a well defined gas environment could be provided, which should facilitate highly reproducible evaporation measurements. The stability of the system is expressed by Fig. 11.4. Within about 10 minutes 1000 images of the Mie scattering emitted by the droplets were taken. The corresponding Mie signals were evaluated and the resulting droplet size spectrum was determined. Each image contained the signals of 2 droplets so that the statistic refers to 2000 droplets. The histogram in Fig. 11.4 shows that the standard deviation of the droplet size is, as mentioned above, about $\sigma = 0.3$ %. The standard deviation of the arithmetic mean value determined according to equation 11.1 is 0.008 %. This is the accuracy for averaged relative droplet size measurements and represents the measurement error for evaporation measurements.

11.4.2 Evaporation Measurements

Example: Evaporation of single component droplets inside the windtunnel.

The measurements of the evaporation rate in the continuous droplet stream were carried out as follows. At 2 distinct points of the droplet chain measurements of the relative droplet size were carried out over a period of time of 15 min by the means of ILIDS. These two probe volumes were located 50 and 61 mm below the generator nozzle, so that the evaporation over a distance of 11 mm was determined. To avoid systematic errors due to a long term drift of the generator the two volumes were probed alternately.

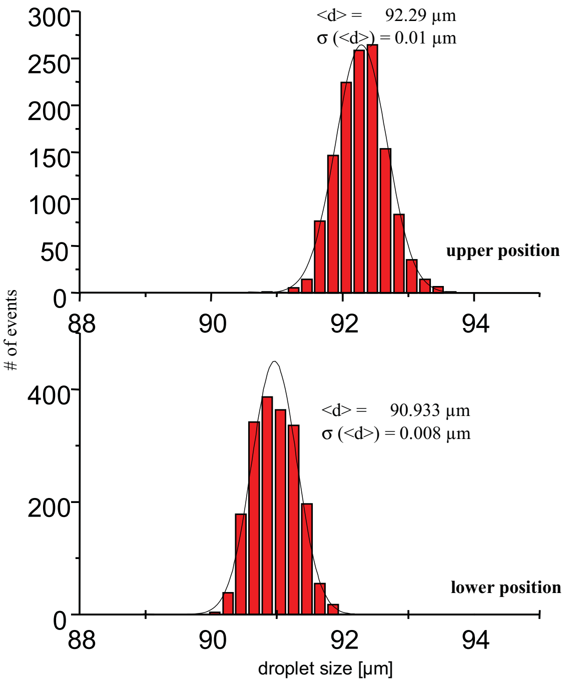

Figure 11.11: Evaporation rate of pentane over distance of 11 mm at height h = 50 mm below the pinhole

A single droplet size measurement at one position took approximately one minute. Typical results obtained from measurements of pentane droplets are depicted in Fig. 11.11. The airflow inside the windtunnel was set to approximately 1 m/s to avoid an accumulation of vapour. The velocity of the droplets can be deduced from the distance of the droplets as $\frac{dN}{dt} = const$, which is based on the assumption that no droplet collisions and break-ups occur. The droplet velocity can be determined simultaneously within each ILIDS measurement. It was about 9 m/s.

Comparison of the evaporation rate of different substances inside the windtunnel

Several liquids with different vapour pressures (boiling points) were investigated under identical flow conditions. The result is depicted in Fig. 11.12. The measurements were carried out completely analogous to the previous evaporation measurements with pentane. The velocity of the air flow was set to 1 m/s. Air temperature was approximately 20° at atmospheric pressure. The corresponding evaporation rates of the tested liquids according to [80] are plotted in Fig. 11.13. It can be seen, that the evaporation rates determined experimentally show good agreement with the evaporation rates according to [80].

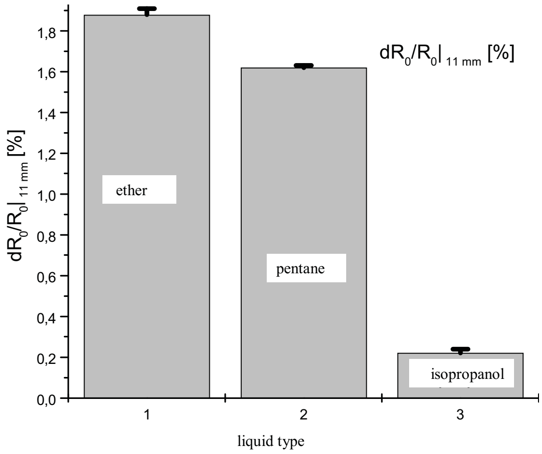

Figure 11.12: Evaporation rate of different liquid substances over a distance of 11 mm at height h = 50 mm

So the expected effect is properly corroborated by the measurement system, which is shown more clearly in Fig. 11.13. These results prove the functionality of the new set-up. The error bars given in Fig. 11.13 arise from the measurement error of single droplet size measurements according to equation 11.1. Slight deviations from the linear correlation in fig. 11.13 can be explained by slightly different droplet sizes of the different liquids.

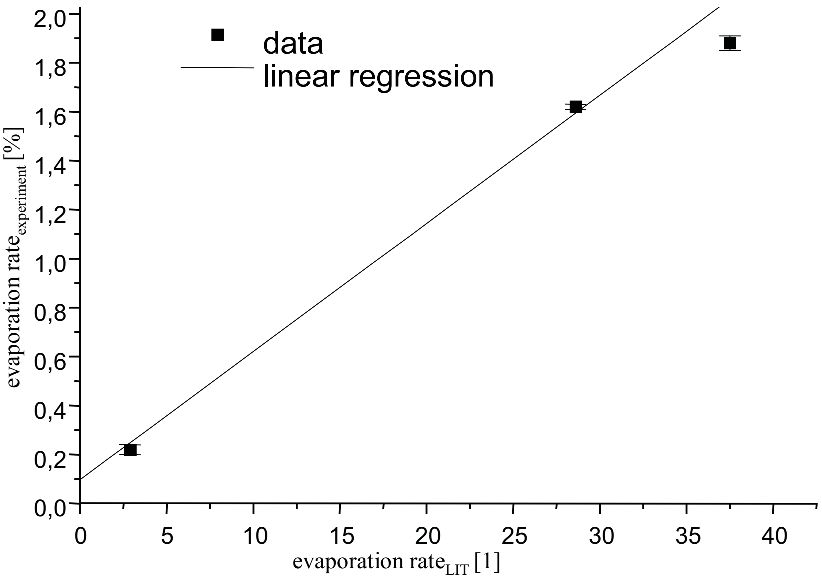

Figure 11.13: Comparison of the measurement results with the expected evaporation rate according to [80]. The values taken from the literature are normalized to the evaporation rate of butyl acetate.

Dependence of the evaporation of pentane on the windtunnel air flow

Finally the dependence of the evaporation rate on the windtunnel air flow velocity was studied. Pentane was used as the liquid. For this purpose measurements were performed at one fixed height beneath the nozzle (h= 50 mm). The initial droplet size was kept constant and the windtunnel air flow was varied. The corresponding measured droplet size distributions are shown in fig. 11.14. The dependence on the air flow is clearly visible. Mean values and their standard deviations are shown in fig. 11.15. A global increase of the evaporation with increasing *absolute* windtunnel air flow velocity is visible.

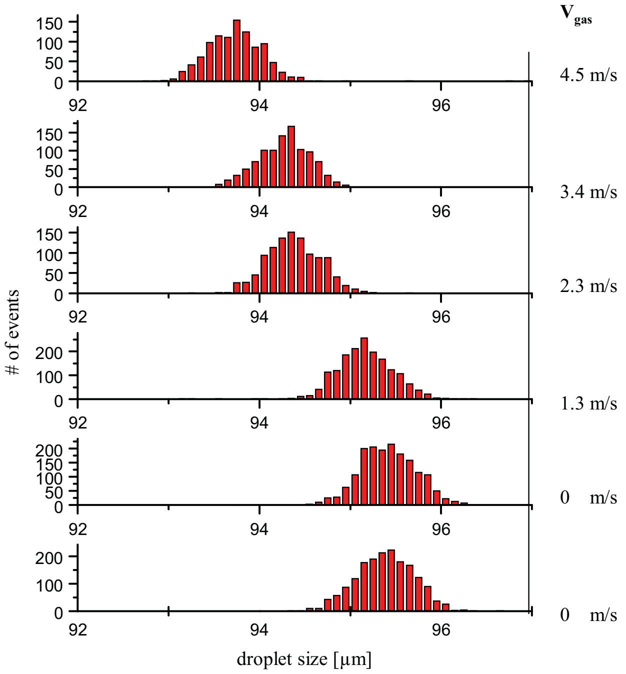

Figure 11.14: Variation of the gas flow velocity inside the windtunnel

Note that the *relative* velocity between the droplets and the air decreases within the given interval of variation of the air flow (v_{air} = 0 - 4,5 m/s, $v_{Tropfen} \approx 9$ m/s). The observed effect therefore is somewhat surprising. It might be expected, that the evaporation would increase with increasing *relative* velocity.

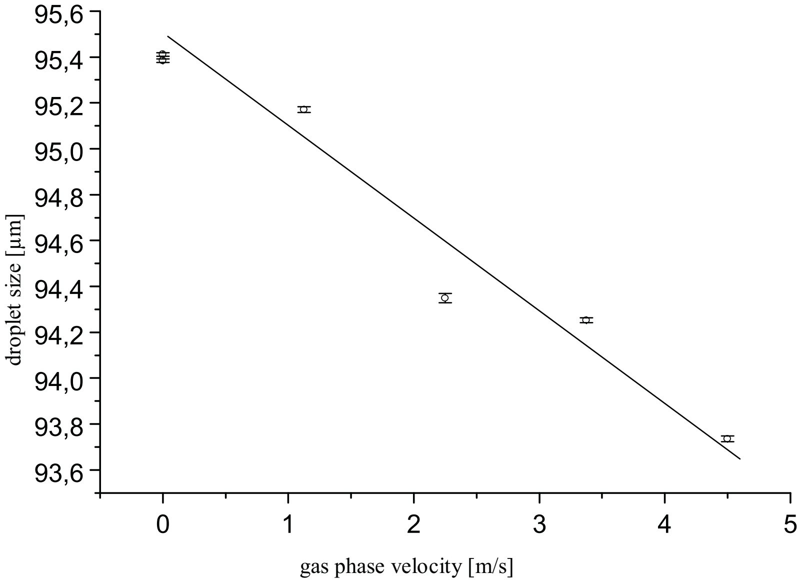

Figure 11.15: Results: Variation of the flow velocity inside the windtunnel

A possible explanation of the observed effect is based on the assumption, that in the proximity of the droplet chain a vapour cloud is formed, that depends on the air flow. Furthermore it is assumed that the *relative* velocity between vapour and the droplets in close proximity to the droplet chain is merely changed by variations of the air flow velocity. This could occur if the gas motion in between the droplets and in close proximity to them is dominated by the motion of the droplets. The vapour density distribution in this vapour cloud would decrease with increasing *absolute* air flow velocity which causes an enhanced removal of vapour from this cloud. In this model the *absolute* velocity of the global air flow would be the decisive quantity. A detailed clarification of this effect could be achieved by laser flow tagging measurements of the gaseous phase in between the droplets and comparative evaporation measurements in counter-flow arrangements. The effect is highly reproducible even in the domain of very low *absolute* air flow velocities. Regarding the droplet velocities it can be stated that there is no obvious dependence of the droplet velocity on the global air flow velocity as fig. 11.16 shows. The accuracy of the control loop for the determination of the air flow velocity given by the manufacturer is approximately 1 %. Nevertheless the given values for the air flow velocity must be regarded as preliminary because the measurement of the air flow by the flow sensor only allows an approximate estimation of the air flow in the probe volume.

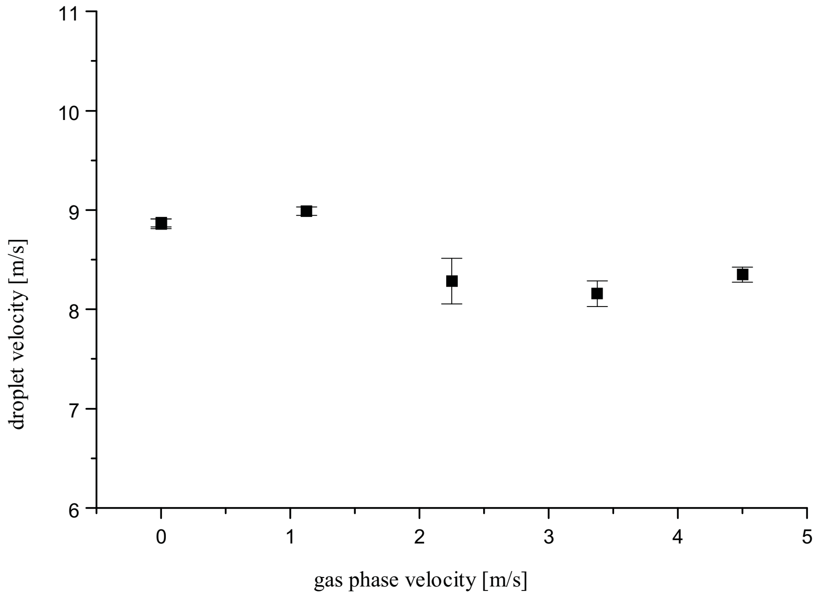

Figure 11.16: Influence of the global air flow velocity on the droplet velocity.

11.5 Summary and conclusions

An improved droplet sizing technique has been developed and adapted for 3D flow systems. A data reduction procedure has been implemented to extract droplet size spectra from a set of Mie scattering images. The measurement technique has been tested in a windtunnel air flow. A windtunnel flow facility as well as an appropriate aerosol generator with a monodisperse droplet size distribution have been developed. The set-up allows precise measurements of the evaporation rate of droplets in a continuous droplet stream and therefore provides a tool for fundamental evaporation studies. First results from a continuous droplet stream were found. In the future investigations on single droplets, short droplet sequences and regular droplet clusters will be performed. Evaporation measurements will be combined with measurements of the vapour concentration and the gas phase velocity in close proximity to the droplets.

Chapter 12

Summary, conclusions and outlook

The existence of a huge lack of experimental data from both technical and fundamental two phase flows was mentioned. The development of laser based non-intrusive measurement techniques to overcome this problem were the task of this work.

An optical flow algorithm was adapted for the determination of the velocity fields of continuous and dispersed phase in flow systems. It was used as data reduction method for the newly developed Gaseous Imaging Velocimetry (GIV) technique. The measurement technique including the data reduction has been validated by comparing it to the well-established Particle Image Velocimetry (PIV). Its applicability on scalar data from 2D two-phase flows and reacting gaseous flows was demonstrated.

Laser based measurement techniques concerning 3D two-phase flows have also been developed. Solutions for the measurement of the velocity field of the gaseous phase in between the droplets as well as of the liquid phase in an automotive DI spray have been given. The suggested laser flow tagging (LFT) techniques are capable to determine reliable 2D velocity projections of both phases. It was mentioned that these techniques can be performed simultaneously. Thus investigations on a single-shot basis are possible. The obtained results serve as input data for numerical models to predict the fundamental properties of the sprays (break-up, evaporation, droplet size spectra etc.).

Pointwise acceleration measurements were performed, which allow to observe directly the interaction of gas and liquid phase. The obviously possible extension of the planar velocity measurement techniques to planar acceleration measurement techniques is noteworthy. For this purpose two consecutive planar velocity measurements have to be performed. It was shown that the LFT techniques can be applied in a spray/wall system. The capability of resolving effects due to the presence of the wall was demonstrated. Thus LFT might serve as a tool for the analysis of wall-guided mixing processes, which is an important problem as far as the development of DI engines is concerned. LFT was extended to stereoscopic LFT, which allows to measure 3D velocity vectors in a plane with high precision even in turbulent flows. The data reduction was always performed by means of the OFA, which was adapted to the new binary-like type of images to yield velocity fields with the highest possible resolution.

An advanced droplet sizing technique has been developed for the investigation of the evaporation rate of microdroplets in 3D flow systems. The accuracy for relative droplet sizing measurements was improved by more than 2 orders of magnitude. A monodisperse, small and aerodynamic aerosol generator for the use in windtunnels has been developed. In combination with a windtunnel facility a precise system for fundamental studies on the evaporation of microdroplets was built and data from a continuous droplet stream were obtained. The results demonstrate the accuracy of the measurement technique. Investigations on single droplets (produced by the aerosol generator in "drop-on-demand"-mode), short droplet sequences (electrostatic deflection) and regular droplet clusters can be performed. Evaporation measurements can be combined with measurements of the vapour concentration and the gas phase velocity in close proximity to the droplets. The vapour density could be determined via LIF and the gas phase velocity by "micro - LFT". Thus extensive data sets describing elementary two phase systems can be obtained, with which numerical models are meant to be optimized.

Bibliography

[1] W.D. Bachalo, Int. J. Multiphase Flow **20** (Suppl.), 261-295 (1994); A. Brandt, W. Merzkirch, Part. Part. Syst. Charact. **11**, 156-158 (1994).

[2] J.-F. Le Coz, in: Ninth International Symposium on Applications of Laser Techniques to Fluid Mechanics, Paper 7.3, Lisbon, Portugal (1998); L. Araneo, C. Tropea, in: Spray ‘99, (5. Workshop über Techniken der Fluidzerstäubung und Untersuchungen von Sprühvorgängen) Universität Bremen, in English (1999).

[3] W. Hentschel, A. Homburg, G. Ohmstede, T. Müller, G. Grünefeld, SAE Tech. Paper No. 1999-01-3660 (1999).

[4] F. Zhao, M.-C. Lai, D.L. Harrington, Progr. Energy Combust. Sci. **25**, 437-562(1999).

[5] G.K. Fraidl, W.F. Piock, M. Wirth, SAE Tech. Paper No. 960465 (1996).

[6] J.A. Wehrmeyer, L.A. Ribarov, D.A. Oguss, F. Batliwala, R.W. Pitz, AIAA Paper 99-0646, **37**, "Aerospace Sciences Meeting & Exhibit", Jan. 11-14 Reno/NV (1999); L.A. Ribarov, J.A. Wehrmeyer, F. Batliwala, R.W. Pitz, P.A. DeBarber, AIAA J. **37**(6), 708 (1999).

[7] R.B. Miles, D. Zhou, B. Zhang, W.R. Lempert, AIAA J. **31** (3), 447-452 (1993); R.B. Miles, C. Cohen, J. Connors, P. Howard, S. Huang, E. Markowitz, G. Russell, Opt. Lett. **12** (11), 861-863 (1987).

[8] L.R. Boedecker, Opt. Lett. **14** (10), 473-475 (1989); C. Orlemann, C. Schulz, J. Wolfrum, Chem. Phys. Lett. 307, 15-20 (1999).

[9] H. Finke G. Grünefeld, "An Experimental Investigation of Extinction of Curved Laminar Hydrogen Diffusion Flames", Proc. Combust. Inst. 28, Symposium (International) on Combustion, Edinburgh (2000).

[10] S. Krüger, G. Grünefeld, Appl. Phys. B **69**, 509 (1999).

[11] S. Krüger, G. Grünefeld, Appl. Phys. B **70**, 463-466 (2000).

[12] R.E. Falco, C.C. Chu, Proc. SPIE Vol. **814**, 706-710 (1987).

[13] B. Hiller, R.A. Booman, C. Hassa, R.K. Hanson, Rev. Sci. Instrum. **55** (12), 1964-1967 (1984).

[14] S. Arndt, Private Communication, Robert Bosch GmbH Stuttgart, Germany (1999).

[15] I. Hemmilä, J. Alloys Comp. **225**, 480-485 (1995)

[16] E. F. Gudgin Dickson, A. Pollak, E.P. Diamandis, J. Photochem. Photobio. B **27**, 3-19 (1995)

[17] P.T. Tokumaru, P.E. Dimotakis, Exp. in Fluids **19**, 1-15 (1995);

[18] G. Grünefeld, H. Finke, J. Bartelheimer, S. Krüger, "Probing the Velocity Fields of Gas and Liquid Phase Simultaneously in a Two-Phase Flow", Exp. in Fluids, **29** (2000), 322-330.

[19] G.M. Faeth, Prog. Energy Combust. Sci. 9, 1-76 (1983).

[20] W.A. Sirignano, J. Fluids Engineering 115, 345-378 (1993).

[21] K. Annamalai, W. Ryan, S. Danapalan, Prog. Energy Combust. Sci. 20, 487-618, 1994;

[22] T. Elperin, B. Krasovitov, B., Atomization and Sprays 4, 79-97, 1994.

[23] R.A. Gore, C.T. Crowe, Int. J. Multiphase Flow 15 (2), 279-285, 1989; G. Hetsroni, Int. J. Multiphase Flow 15 (5), 735-746, 1989.

[24] V.G. McDonell, G.S. Samuelsen in Combusting Flow Diagnostics, Chapter 10 (Eds. D.F.G. Durao et al.), Kluwer Academic Publ., Dordrecht, Boston, London, 1992; I. Gillandt, T. Schulze, U. Fritsching, K. Bauckhage, Flow Meas. Instr. 9, 1-9 (1998).

[25] Y.A. Hassan, O.G. Philip, W.D. Schmidl, "Bubble Collapse Velocity Measurements using a PIV Technique with Fluorescent Tracers", ASME FED-Vol. 172, 85-92 (1993); G. Sridhar, J. Katz, Phys. Fluids 7, 389-399 (1995).

[26] L.A. Ribarov, J.A. Wehrmeyer, F. Batliwala, R.W. Pitz, P.A. DeBarber, AIAA J. 37(6), 708 (1999).

[27] G. Grünefeld, J. Bartelheimer, H. Finke, S. Krüger, "Gas-phase Velocity Field Measurements in Sprays Without Particle Seeding", Exp. in Fluids, **29** (2000), 238-246.

[28] S. Krüger, G. Grünefeld: "Stereoscopic Flow Tagging Velocimetry", Appl. Phys. B, **29** (1999) 509-512.

[29] S. Arndt, Private Communication, Robert Bosch GmbH Stuttgart, Germany (1999).

[30] J.G. Calvert, J.N. Pitts, Photochemistry, Wiley, New York, (1966).

[31] M.P. Arroyo, C.A. Greated, Meas. Sci. Technol. **2** , 1181-1186 (1991).

[32] P.A. DeBarber, M.S. Brown, J. Segall, R.W. Pitz, T.M. Brown, R.A. Yetter, AIAA Paper 96-0300, 34^{th} Aerospace Sciences Meeting & Exhibit, Jan. 15-18 Reno/NV (1996).

[33] R.E. Falco, C.C. Chu, Proc. SPIE **814** , 706-710 (1987).

[34] C. Orlemann, C. Schulz, J. Wolfrum, Chem. Phys. Lett. **307** , 15-20 (1999).

[35] H.-G. Maas, Determination of velocity fields in flow tomography sequences by 3-D least squares matching, Proc. 2nd Conf. on Optical 3-D Measurement Techniques, Zurich, Oct. 4-7 (1993).

[36] W.J.A. Dahm, L.K. Su, B. Southerland, Phys. Fluids A **4** (10), 2191-2206 (1992).

[37] H. Finke, H. Spiecker, P. Andresen, J. Chem Phys. **110** (10), 4777-4782 (1999).

[38] R. Engleman, P.E. Rouse, H.M. Peek, V.D. Baiamonte, V.D., Beta and Gamma Systems of Nitric Oxide, Los Alamos Sc. Lab. Report No. LA-4364 (1970).

[39] Gornowicz, G.G. (1997), Continuous-Field Image-Correlation Velocimetry and its Application to Unsteady Flow Over an Airfoil, Thesis, Graduate Aeronautics Laboratory, California Institute of Technology, Pasadena CA.

[40] Grünefeld, G., Gräber, A., Diekmann, A., Krüger, S., Andresen, P. (1998a) Measurement System for Simultaneous Species Densities, Temperature and Velocity Double-Pulse Measurements in Turbulent Hydrogen Flames, Combust. Sci. and Tech. 135 (16^{th} Special Issue on Dynamics of Reactive Systems), 135-152.

[41] Keane, R.D., Adrian R.J. (1990) Optimization of particle image velocimeters. Part 1: Double pulsed systems, Meas. Sci. Technol. **1** , 1202-1215.

[42] Keane, R.D., Adrian R.J., Zhang, Y. (1995) Super-resolution particle imaging velocimetry, Meas. Sci. Technol. **6** , 754-768.

[43] Komiyami, M., Miyafuji, A., Takagi, T. (1996) Flamelet behaviour in a turbulent diffusion flame measured by Rayleigh scattering image velocimetry, 26th Symp. (Intl.) on Comb., 339-346.

[44] Su, L.K., Dahm, J.A. (1996) Scalar imaging velocimetry measurements of the velocity gradient tensor field in turbulent flows. 1. Assessment of errors, Phys. Fluids **8** (7), 1869-1882.

[45] Krüger S, Grünefeld G, Arndt S, Hentschel W, Planar velocity measurements of the gas and liquid phase in dense sprays by flow tagging, 10th Int. Symp. On Appl. Of Laser Techniques To Fluid Mechanics, Lisbon, Portugal, 2000.

[46] Dahm, W.J.A., Su, L.K., Southerland, B. (1992) A scalar imaging velocimetry technique for fully resolved four-dimensional vector velocity field measurements in turbulent flows, Phys. Fluids A **4** (10), 2191-2206.

[47] Durst, F., Melling, A., Whitelaw, J.H., 1987, Theorie und Praxis der Laser-Doppler-Anemometrie, G. Braun Karlsruhe, p. 385.

[48] Georjon, T., Chale, H.G., Champoussin, J.-C., Marie, J.-L., Lance, M., 1997, A droplet tagging method to investigate Diesel spray, SAE Technical Paper No. 970351.

[49] Glezer, A., 1988, The formation of vortex rings, Phys. Fluids **31** (12), pp. 3532-3542.

[50] Hassan, Y.A., Canaan, R.E., 1991, Simultaneous velocity field measurements of bubbles and sorrounding fluid by pulsed laser velocimetry, Proc. of the Fourth Int. Conference on Laser Anemometry, Advances and Applications, ASME, **1** , pp. 387-400.

[51] Lierke, E.G., 1997, Techniken und Anwendungen der Ultraschall-Zerstäubung, ein Rückblick auf 35 Jahre Forschung und Entwicklung, Proc. SPRAY '97 (W.W. Koschel, O.J. Haidn eds.) Lampoldshausen, in German.

[52] Lindken, R., Gui, L., Merzkirch, W., 1998, Geschwindigkeitsmessungen in Mehrphasenströmungen mit Hilfe der Particle Image Velocimetry, Chemie Ingenieur Technik, **70** , pp. 856-860, in German.

[53] Maxworthy, T., 1972, The structure and stability of vortex rings, J. Fluid Mech. **51** (1), pp. 15-32.

[54] Merzkirch, W., Gui, L., Hilgers, S., Lindken, R., Wagner, T., 1997, PIV in Multiphase Flow; Proc. of the Int. Workshop on PIV, Fukui, Japan, pp. 165-171.

[55] Rottenkolber, G., Richter, B., Dullenkopf, K., Wittig, S., 1998, PIV-Untersuchungen der Zweiphasenströmung im Saugrohr eines Ottomotors, Lasermethoden in der Strömungsmeßtechnik, 6. Fachtagung GALA, W. Merzkirch et al. (eds.), in German.

[56] Sridhar, G., Ran, B., Katz, J., 1991, Implementation of particle image velocimetry to multi-phase flows, Cavitation Multiphase Flow Forum **109** , p. 205.

[57] Sridhar, G., Katz, J., 1995, Drag and Lift Forces on Microscopic Bubbles Entrained by a Vortex, Phys. Fluids **7** , pp. 389-399.

[58] Stamm, K., 1964, Ph. D. Thesis, RWTH Aachen, in German.

[59] Tokumaru, P.T., Dimotakis, P.E. (1995) Image Correlation Velocimetry, Exp. In Fluids, **19** , 1-15.

[60] Buch, K.A., Dahm, J.A. (1998) Experimental study of the fine-scale structure of conserved scalar mixing in turbulent shear flows Part 2. Sc»1, J. Fluid Mech., **364** , 1-29.

[61] Eckbreth, A.C. (1988) Laser Diagnostics for Combustion Temperature and Species Abacus Press, Cambridge Mass., 123-124.

[62] Heywood, J.B. (1988) Internal Combustion Engine Fundamentals, McGraw-Hill Publ., New York, p. 195.

[63] Lenz, H.P. (1990) Gemischbildung bei Ottomotoren, Springer, Wien, New York, p. 138, in German.

[64] Long, M.B. (1993) Multidimensional Imaging in Combusting Flows by Lorenz-Mie, Rayleigh, and Raman scattering, in Instrumentation for Flows with Combustion, (Ed. by A.M.K.P. Taylor) Academic Press, London, 467-508.

[65] Meinhardt, C.D., Wereley, S.T., Santiago, J.G., Adrian, R.J., (1998) Diagnostic techniques for microfluidics research. Proceedings of the Ninth International Symposium on Applications of Laser Techniques to Fluid Mechanics, Lisbon, Portugal, July 13-16.

[66] Rothe, E.W., Andresen, P. (1997) Application of tunable excimer lasers to combustion diagnostics: a review, Appl. Opt. **36** (18), 3971-4031.

[67] Saffman, P.G. (1992) Vortex dynamics, Cambridge Monographs on Mechanics and Applied Mathematics, Cambridge University Press.

[68] P. Ferrao and M.V. Heitor, "Probe and Optical Techniques for Simultaneous Scalar-Velocity Measurements" Combustion Flow Diagnostics (D.F.G. Durao et al. Eds.), Kluwer Academic Publ., Dordrecht (Netherlands) 1992.

[69] C.J. Sung, C.K. Law, R.L. Axelbaum, "Thermophoretic Effects on Seeding Particles in LDV Measurements of Flames", Comb. Sci. Tech. **99** , 119-132, 1994.

[70] T.S. Cheng, J.A. Wehrmeyer, R.W. Pitz, "Simultaneous Temperature and Multi-species Measurements in a Lifted Hydrogen Diffusion Flame", Combust. Flame **91** , 323-345, 1992.

[71] G.S. Lewis, B.J. Cantwell, U. Vandsburger, C.T. Bowman, "An Investigation of the structure of a laminar non-premixed flame in an unsteady vortical flow", 22nd Symposium (Intl.) on Combustion, The Combustion Institute, pp. 515-522, 1988.

[72] B. Atakan, V., Jörres, K., Kohse-Höinghaus, "Double Pulse 2D LIF as a Means for Following Flow and Chemistry Development in Turbulent Combustion" Ber. Bunsenges. Phys. Chem. **97** (12), 1706-1710, 1993.

[73] König G., Anders K., Frohn A. (1986): " A new light scattering technique to measure the diameter of periodically generated moving droplets " J. Aerosol Sci., **17**, pp. 157-167

[74] R. Ragucci, A. Cavaliere und P. Massoli (1990): " Drop sizing by laser light scattering exploiting intensity angular oscillation in the Mie regime", Part. Charact. **7**, pp. 221-225.

[75] R. Calabria und P. Massoli (2000): " Experimental study of droplets in evaporating regime by 2D scattering analysis ", 10th. Int. Symp. Applications of Laser Techniques to Fluid Mechanics, Lisbon 10.-13. 7. 2000.

[76] T. Kobayashi, T. Kawaguchi, M. Maeda (2000): " Measurement of spray flow by an improved interferometric laser imaging droplet sizing (ILIDS) system ", 10th. Int. Symp. Applications of Laser Techniques to Fluid Mechanics, Lisbon 10.-13. 7. 2000.

[77] Y. Nivwa, Y. Kamiya, T. Kawagucchi und M. Maeda (2000): " Bubble sizing by interferometric laser imaging ", 10th. Int. Symp. Applications of Laser Techniques to Fluid Mechanics, Lisbon 10.-13. 7. 2000.

[78] P. Massoli (1984): " Scattering of electromagnetic-plane waves by radially inhomogeneous spheres: a finely stratified sphere model ", Appl. Opt. Vol. **33**, No.3 pp. 501.

[79] P. Massoli, F. Beretta und A. D‘ Alessio (1989): " Single droplet size, velocity, and optical characteristics by the polarisation properties of scattered light ", Appl. Opt. Vol. **28**, No.6, pp. 1200-1205.

[80] http://www.chemfinder.com

[81] O. Pajot. und C. Mounaim-Rousselle (1999): " Droplet sizing by Mie scattering interferometry in a spark ignition engine", Part. Part. Syst. Charact. **16**, 160-168.

[82] J.I. Nogueira, A. Lecuona, P.A. Rodriguez (1997): " Data validation, false vectors correction and derived magnitudes calculation on PIV data", Meas. Sci. Technol. **8**, 1493-1501.

[83] Douglas P. Hart (2000): " Super-resolution PIV by recursive local-correlation.", Journal of Visualization **3**(2), 187-94.

[84] Keane R. D., Adrian R.J., (1992): " Theory of cross-correlation analysis of PIV images", Appl. Sci. Res. **49**, 191-215.

[85] Raffel M., Kompenhans J., (1996): " Post processing: data validation", Von Karman Institute for Fluid Dynamics Lecture Series 1996-03

[86] Brock, A. Deimling, L. , (1999): " Direct cross correlation for high resolution PIV of vortex structures ", INTERNATIONAL ANNUAL CONFERENCE- FRAUNHOFER INSTITUT FÜR CHEMISCHE TECHNOLOGIE, 1999, 103 ff.

[87] Pust O. : " PIV: Direct Cross-Correlation compared with FFT-based Cross-Correlation", Department of Fluid Mechanics, Faculty of Mechanical Engineering, University of the Federal Armed Forces Hamburg, D-22039 Hamburg, Germany

[88] Barron J.L., Fleet D.J., Beauchemin S.S. (1994) : "Performance of Optical Flow Techniques", International Journal of Computer Vision, **12**:1, 43-77

[89] Arroyo M.P., Greated C.A. (1991): "Stereoscopic particle image velocimetry", Meas. Sci. Technol. **2**, 1181-1186

[90] Press W.H., Teukolsky S.A., Vetterling W.T., Flannery B.P. : "Numerical Recipes in C, The Art of Scientific Computing", 2nd edition

[91] Dierksheide U. : Dissertation: "Aufbau und Test eines Verfahrens zur zweidimensionalen Strömungsfeldmessung durch Mie-Streuung mit UV-Excimerlaser"

[92] Berglund R.N., Liu B.Y.H. (1973): "Generation of monodisperse aerosol standards", Environ. Sci. Technol. **7**, 147-153

List of Figures

Acknowledgements

This work was supported by "Bundesministerium für Bildung und Forschung" (BMBF) and "Deutsche Forschungsgemeinschaft" (DFG).
I woukd like to thank Prof. Dr. Gerd Grünefeld and Prof. Dr. Peter Andresen for the good teamwork and the rest of our group for their contribution to a unique working atmosphere.